Xenon NMR with spectroscopic, spatial, and temporal resolution

Von der Fakultät für Mathematik, Informatik und Naturwissenschaften der
Rheinisch-Westfälischen Technischen Hochschule Aachen
zur Erlangung des akademischen Grades einer Doktorin der Naturwissenschaften
genehmigte Dissertation

vorgelegt von

Dipl.-Chem.

Kerstin Münnemann geb. Kletzke

aus Krefeld

Berichter: Universitätsprofessor Dr. Dr. h. c. Bernhard Blümich

Universitätsprofessor Dr. Marcel Liauw

Tag der mündlichen Prüfung: 29. September 2005

Diese Dissertation ist auf den Internetseiten der Hochschulbibliothek online verfügbar.

Content

1 Introduction

Nuclear magnetic resonance (NMR) spectroscopy is one of the most powerful tools for the detailed analysis of molecular structure and dynamics of molecules in solution. For this reason it was used for countless applications in chemistry and biology since its discovery in 1945 by Bloch [Blo] and Purcell [Pur]. The development of different NMR techniques like imaging, diffusion or velocity measurements, and relaxometry has lead to widespread applications in nearly every field of natural science like physics, chemistry, biology, material science, and medicine. However, this work is devoted to a new and growing field of NMR: ^{129}Xe NMR, and will give no general introduction to the theory of NMR. For the fundamental theory and practical applications the reader is referred to the literature [Abr, Sli, Cal, Blü, Blü2, Ern, Fuk, Can, Kim].

During the last two decades ^{129}Xe NMR has found many applications in material sciences and medicine as can be seen in the following reviews [Bru, Pie, Goo, Che] because of two useful properties of Xenon atoms for NMR: the sensitivity to their environment due to their highly polarizable electron cloud, which results in a wide range of chemical shifts, and the ability of being hyperpolarized, which overcomes the problem of the low signal-to-noise ratio of thermally polarized Xenon. Some examples that exploit the unique ability of ^{129}Xe to report on its local physicochemical environment by means of its extremely sensitive chemical shift, even in the absence of covalent bonding, are cited here. It can be used as a sensitive probe for nano- and mesoporous materials [Ito, Raf2, Chm, Raf3, Rat, Ter, Nos, Jam, Sea, Stu, Mou], as an interesting imaging agent [Alb, Tse, Mou2, Mai, Wan, Han], is useful for probing surfaces [Pie2, Jae, Smi, Kna, Roo], and has potential for lung and tissue visualization [Mug, Swa, Swa2, Maz, Wol]. Furthermore, it has proven to be a useful biosensor for probing proteins upon non-specific binding [Rub, Loc], proteins with hydrophobic pockets upon specific binding [Til, Rub2], ligand-protein binding events [Spe, Han2], and the membrane and cell morphology [Bif, Alb2, Wol2]. Several models exist in the literature to interpret the ^{129}Xe chemical shift in specific applications such as pore size determination in porous media [Rip, Der, Dem, Che2] or for the investigation of polymers [Fre, Mil].

The hurdle to overcome making ^{129}Xe NMR a useful tool for the characterization of inorganic and biological materials within a reasonable experimental time and under moderate

physical conditions is the low density and magnetization of ^{129}Xe compared to ^{1}H nuclei. Hyperpolarization is the tool to negotiate this main draw-back of NMR not only for thermally polarized Xe nuclei. Hyperpolarized noble gases can transfer their polarization to other nuclei by the Spin Polarization Induced Nuclear Overhauser Effect (SPINOE) leading to a higher polarization than that given by the Boltzmann distribution and results in better signal-to-noise ratios. The most established technique to achieve hyperpolarization of ^{129}Xe is the spin-exchange optical pumping using polarized electrons of Rb [Hap, Hap2, Wal, App3, Jau, Cat, Tyc, Dri, Kna2, Su, Haa2, Bru2, Zoo].

This work is meant to reveal the potential of ^{129}Xe NMR with respect to its unique sensitivity to its local environment and to its capability for time-resolved measurements. Therefore experiments were performed combining spectroscopic, spatial, and temporal resolution in various applications. The work is structured as follows: in chapter 2 a brief overview of Xe NMR is presented. Chapter 1 gives an introduction to the technique of hyperpolarization and explains its basic principles. The apparatus to produce hyperpolarized Xe is explained as well. In chapter 1 the general setup of the Xe NMR experiments is described. From chapter 1 onwards the presentation of the results starts. It contains a detailed study of the chemical shift of gaseous and liquid Xe and for Xe dissolved in organic solvents. This chapter reveals also the possibility to use cold solvents as a storage medium for hyperpolarized Xe. A new model is introduced to calculate fundamental constants of the Xe-Xe and the Xe-solvent interactions based on the measured chemical shift. These results serve as the basis for the interpretation of the results of chapters 1 and 1. Chapter 1 reports on the on-line monitoring of polymerization reactions by hyperpolarized ^{129}Xe NMR. It is a good example for the sensitivity of Xe to its chemical environment and reveals also the power of Xe NMR spectroscopy with temporal resolution. Chapter 1 deals with time-resolved chemical shift imaging using accumulated hyperpolarized Xe in different systems. The incorporation process of liquid Xenon in a cold ethanol and ethanol-water matrix is observed with spectroscopic, spatial, and temporal resolution. Chapter 8 gives some examples of multi-dimensional imaging with temporal resolution using a continuous flow of hyperpolarized Xe gas. The exchange mechanism of hyperpolarized Xe gas with organic solvents and a porous material is explored. A summary of the whole work is given in chapter 1 where also future applications are discussed.

2 NMR with ^{129}Xe

The Xenon atom has an atomic weight of 131.29 u and a diameter of 0.44 nm. It possesses the electron configuration [Kr] $4d^{10}5s^25p^6$ and has 54 electrons [Hol]. Because of its small size and chemical inertness it is an ideal probe for material characterization on the nanometer-scale. From the 11 known isotopes of Xenon (9 stabile ones and 2 radioactive ones) two are interesting for NMR, because they have a nonzero nuclear spin I: ^{129}Xe with $I = 1/2$ and ^{131}Xe with $I = 3/2$. The NMR properties of these Xe isotopes are listed in Tab. 2.1 in comparison with the standard nuclei of NMR ^{1}H.

Table 2.1 [Har]: Comparison of the NMR properties of ^{1}H, ^{129}Xe and ^{131}Xe.

Property	^{1}H	^{129}Xe	^{131}Xe
Spin I	1/2	1/2	3/2
$\gamma [10^8 \text{s}^{-1}\text{T}^{-1}]$	2.675	-0.74	0.22
nat. abundance [%]	99.99	26.44	21.18
rel. sensitivity	1.00	$5.60 \cdot 10^{-3}$	$5.84 \cdot 10^{-4}$

It becomes obvious that the low gyromagnetic ratios γ combined with the low natural abundances of the Xe isotopes yields to much lower NMR sensitivities in comparison with the ^{1}H nuclei. Therefore, it is necessary to increase the number of scans and also the experimental time significantly to achieve comparable signal-to-noise (S/N) ratios in NMR measurements with thermally polarized Xe. This problem can be overcome by hyperpolarization which makes also on-line (single scan) measurements viable.

The ^{131}Xe nucleus possesses an electric quadrupole moment which leads to quadrupole relaxation and shortens the T_1 relaxation time to the order of seconds to minutes [Jok] making the storage of hyperpolarized ^{131}Xe difficult. On the other hand the quadrupole moment of ^{131}Xe offers different information that cannot be obtained with spin 1/2 nuclei and therefore experiments with ^{131}Xe have made significant contributions to the field of fundamental physics (test of the local Lorentz invariance and nonlinear quantum mechanics) [Chu, Chu2], to the field of navigation and geometric quantum phases [App, App2] and to

surface NMR investigations [Vol, Wu, Wu2]. However, ^{131}Xe is not the topic of this thesis and for a general overview of the NMR measurements made with ^{131}Xe the reader is referred to the literature [Raf3, Mou3].

In contrast to ^{131}Xe, ^{129}Xe has a very long T_1 relaxation time depending on its physical phase (solid: several hours [Yen], liquid: 25 min [Hun]) which is a drawback for measurements with thermally polarized Xe because long recycle delays are required, but it is an advantage for measurements with hyperpolarized Xe. In the gas phase the spin rotation interaction of the coupling of a nuclear Xe spin to the diatomic Xe-Xe pair which exists during collisions defines the principle limit of the T_1 relaxation time (in the absence of wall relaxation) to $T_1 \approx 56/[\text{Xe}_{\text{gas}}]$, where $[\text{Xe}_{\text{gas}}]$ is the density of Xenon gas in amagat and T_1 the longitudinal relaxation time in hours [Tor]. One amagat is defined as the density of an ideal gas at 293 K and 1 bar pressure and corresponds to $2.69 \cdot 10^{19}$ atoms/cm^3. In the presence of oxygen the T_1 relaxation time of gaseous Xe is remarkably shortened by the intermolecular dipole-dipole interaction of the nuclear and electron spins [Jam2]. Therefore a small amount of oxygen can be used as relaxation agent in measurements with thermally polarized Xe, because it has a negligible effect on the Xe chemical shift [Jam3, Jam4, Jam5].

The most important advantage that provides Xenon for NMR is its sensitivity to its chemical and physical environment which makes it an interesting probe for material science, biology or medicine. The reason for this extraordinary sensitivity leading to a chemical shift range of several thousand ppm is its large (54 electrons) and therefore easily polarizable electron cloud. An overview over the accessible chemical shift range of ^{129}Xe NMR is given in Fig. 2.1.
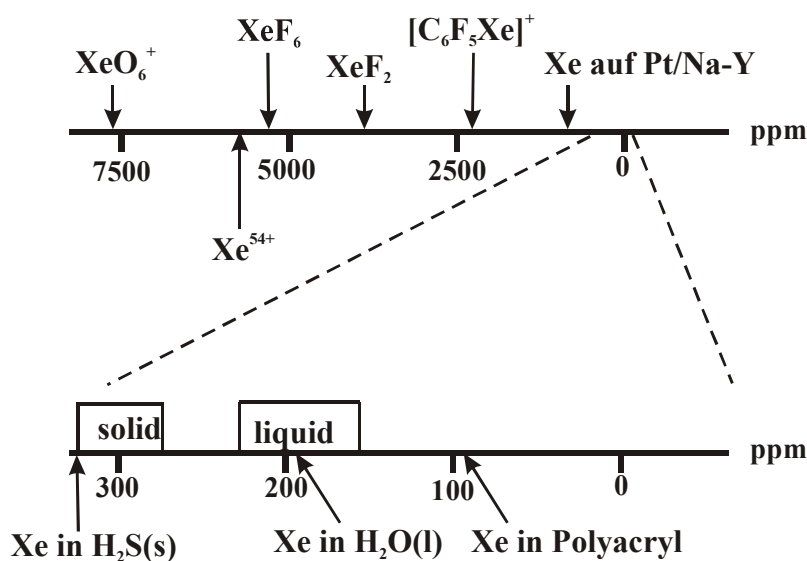

Fig. 2.1: Chemical shift range of ^{129}Xe NMR with examples of specified materials [Raf]. The chemical shift is referenced to Xe gas at zero Xe density.

The substances which lead to the largest chemical shifts have very strong electronegative covalent bonding partners to the Xe atom (like O or F) that are attracting the electrons from the Xe nucleus yielding to a very strong deshielding effect. Under normal conditions Xe is chemically inert, which makes it an excellent probe for material science and biology but shrinks also its chemical shift range. The chemical shift range of Xe NMR which corresponds to physical, chemical, and non-covalent local changes in the sample is magnified in the bottom part of Fig. 2.1, it still consists of 300 ppm which is much larger than the chemical shift range of ^{1}H (15 ppm) and therefore also minimal changes in materials or tissues can be detected. A detailed consideration of the fundamental theory of the chemical shift of ^{129}Xe in the gas, liquid, and dissolved phase is given in chapter 1. The thermodynamic properties of Xenon allow measurements in all physical states because they exist at moderate physical conditions as is depicted in Fig. 2.2.
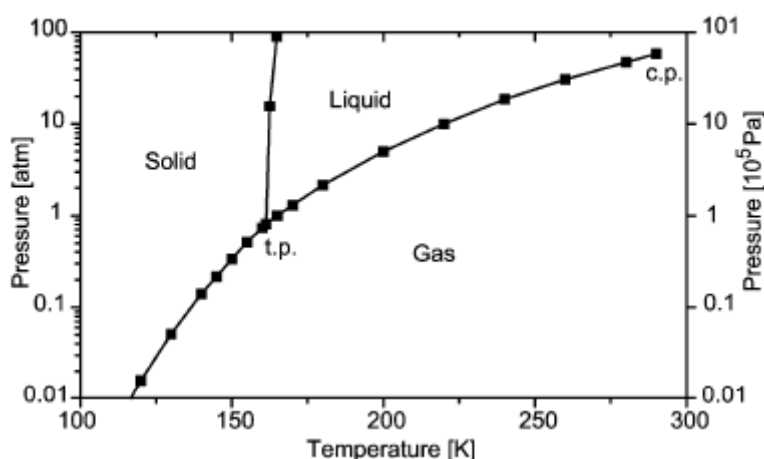
Fig. 2.2: Phase diagram of Xenon. Triple point (t.p.), 161.3 K, 81.6 kPa. Critical point (c.p.), 289.7 K, 5.88 MPa. 1 atm = 101,325 Pa. Data taken from [Coo].

Under normal conditions Xenon exists as an lipophilic gas with only weak van-der-Waals interactions between the single atoms. Its boiling and melting points at 1 bar are 165.02 K and 161.38 K, respectively. This makes storage of hyperpolarized Xe at temperatures of liquid nitrogen possible. Xe becomes supercritical at 289.7 K and 58 bar making measurements of hyperpolarized Xe in supercritical state viable [Haa, Lea].

3 Basic principle of hyperpolarization by spin-exchange optical pumping

Spin-exchange optical pumping is the notation of a mechanism for the transfer of angular momentum from circular polarized laser light to electronic and afterwards to nuclear spins [Hap, Wal, App3]. It is capable of producing moderate to high levels of nuclear spin polarization in Xenon and Helium under a wide range of conditions (e. g. temperature, gas pressure, and field strength). The first step of this mechanism, the optical pumping, was discovered by Kastler in 1950 [Kas], for which he was awarded the Nobel prize in physics in 1966. The second step, the ability to transfer polarization from electron to nuclear spins, was found by Bouchiat et al. in 1961 [Bou]. Under optimized conditions laser-polarized Xenon can give sensitivity enhancement of as much as 10^5 compared to thermally polarized Xenon [Gae]. A very important fact is that the polarization of the spins is no longer dependent on the magnetic field strength they experience, because the magnetization of the sample is no longer given by the Boltzmann distribution. Therefore the technique of hyperpolarization allows also measurements of small samples in very small magnetic fields [App5], which is a breakthrough for NMR. Important steps towards the successful application of hyperpolarized Xenon were the separation of Xenon from the optical pumping cell containing Rb metal and the realization of flow-mode hyperpolarization of Xenon gas [Goo, Son, Dri, Sta]. A key to make hyperpolarized Xenon widely applicable to a variety of applications beyond proof of principle work, was the achievement of extremely high polarizations of up to 60% with the help of theoretical framework [Tyc, Dri, Kna2], the use of high power lasers [Hir] and technical advancements [Zoo]. Figure 3.1 represents a schematic overview of the hyperpolarization process.
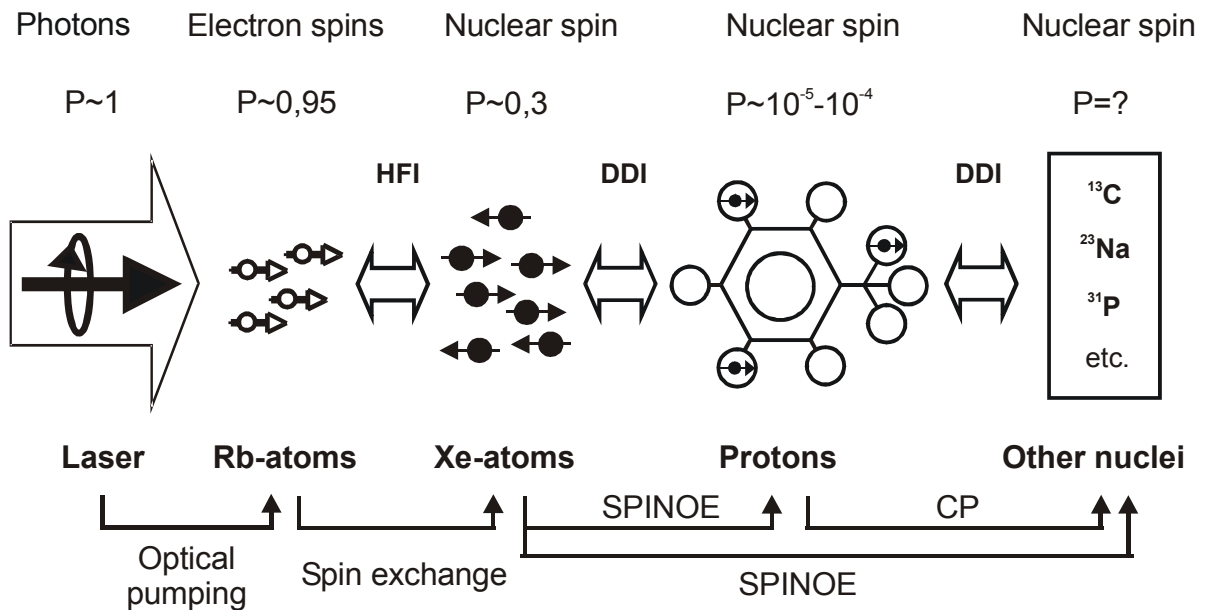
Photons   Electron spins   Nuclear spin   Nuclear spin   Nuclear spin

P~1   P~0,95   P~0,3 $P \sim 10^{-5}\text{-}10^{-4}$ P=?

Fig. 3.1: Principle of polarization transfer: polarization is transferred from photons to Rb-atoms by optical pumping, from the electron spin to the nuclear spin of Xe by hyperfine interaction (HFI) and from the Xe spins to other nuclear spins by dipole-dipole interaction (DDI). The magnitudes of the spin polarization P for each step are indicated at the top of the figure [App4].

The absorption of the circular polarized laser light by the Rb-atoms leads to a nearly perfect polarization of the Rb electron spins. The ordered Rb electron spins experience many interactions with each other and the gases (Helium, Nitrogen and Xenon) which are present in the optical pumping cell. During a collision with other Rb atoms they undergo a flip-flop process, which does not lead to a loss of polarization. Collisions with Xe-atoms cause the exchange of polarization by hyperfine coupling of the Rb electron spin to the nuclear spin of Xe. If the Xe atoms get in contact with different nuclei (for example the protons of toluene like in Fig. 3.1) they can transfer their polarization via SPINOE (Spin Polarization Induced Nuclear Overhauser Effect) [Nav, Son2, Son3, App8, Cav]. The SPINOE is driven by dipole-dipole interactions and therefore works best if the distance between the Xe and the interacting atom is small and the correlation time is long. For that reason, the most efficient polarization transfer takes place between Xe and protons, which results in a high net magnetization of protons which can exchange their polarization by cross polarization (CP) with other nuclei.

3.1   Optical Pumping

All alkali-metal elements can be used for optical pumping because they very efficiently absorb the laser light due to their large optical dipole moment. They have a relatively simple quantum mechanical structure (only one valence electron in the S state) and therefore well-defined optical selection rules with the optical transitions of the ground state in the near infrared.   The contents of an optical pumping cell are Rb atoms in vapor state and a gas mixture of approximately 97% He, 2% N_2 and 1% Xe at high gas pressure (7-10 bar). The high pressure in the optical pumping cell broadens the D_1 transition line of the Rb electrons making efficient use of broadband lasers (1-2 nm width) possible [Rom]. Figure 3.2 indicates the interaction of a Rb-atom with circular polarized light and an external magnetic field, which leads to a Zeeman splitting of the energy levels of the ground and excited states.
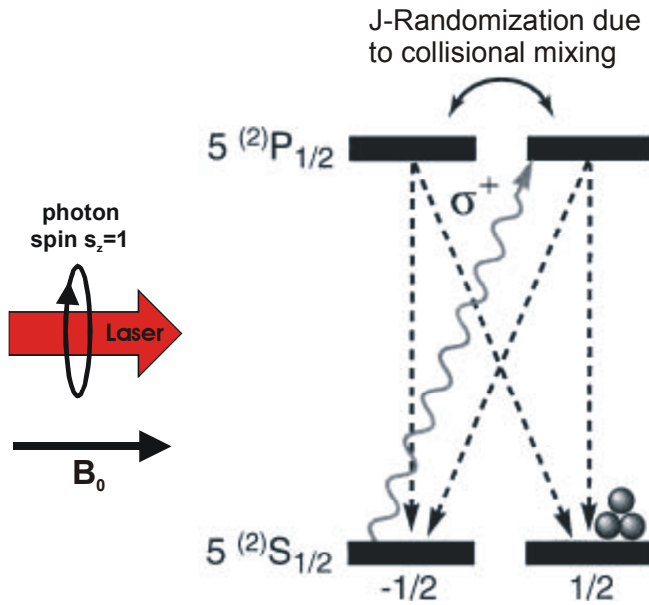

Fig. 3.2: Schematic sketch of the alkali-metal optical pumping process, the hyperfine couplings ($F = I + S$) between the electronic (S) and nuclear (I) spins are neglected [Goo].

The absorption of circular polarized laser light of the wavelength 794.8 nm (D_1 transition) leads to the excitation of the Rb atoms from the ground state $5^2S_{1/2}$ to the excited state $5^2P_{1/2}$. For right circular polarized light only the transition from the $m_s = +1/2$ ground state is allowed leading to a selective depopulation of this state. The J-randomization due to collisions with ^{4}He atoms causes an equal distribution of the two excited states with $m_j = -1/2$ and $m_j = +1/2$ resulting in a complete loss of polarization. Quenching collisions with N_2 gas yield an equal repopulation of the ground states preventing the relaxation to the ground state by emission of fluorescence photons, which destroy polarization. Here the depopulation cycle

of only <u>one</u> of the ground states starts again resulting therefore in a ground state polarization of the electron spin. A very import aspect of the optical pumping cycle is that all conversions of the electron states are sudden with respect to the nuclear spin polarization. The electron polarization is destroyed by spin relaxation processes such as e. g. collisions with the wall of the pumping cell and collisions with Xe atoms. The rapidly reached steady-state population of the Rb electrons can be well described by a spin temperature parameter β and the electron spin polarization P [App3]. Therefore the polarization of all Zeeman energy levels of the Rb ground state can be determined by measuring only one parameter $P = \tanh \beta / 2$. P can be measured by the method of optically detected magnetic resonance (ODMR), which can give very useful information of the spatial distribution of the Rb polarisation inside the optical pumping cell and is therefore an important tool to improve the optical pumping process [Bag, App7]. Under high pressure conditions the polarization of the Rb electrons which depends on space r can be described by [App6]:

$$P_{Rb}(r) = s_z \cdot \frac{R(r)}{\gamma_{SD} + R(r)},$$ (3.1-1)

where s_z is the photon spin, R the optical pumping rate of the laser and γ_{SD} (SD: spin destruction) the rate of depolarization by collisions with e. g. Xe-atoms. Near the walls of the pumping cell P_{Rb} drops to zero, as the residence time of the Rb atoms is long enough to permit significant depolarization.

3.2   Polarization transfer from Rb electrons to Xe nuclei

The spin exchange between Rb electrons and Xe nuclei is based on a collisional polarization transfer [Hap2, Wal, App3]. The number and kind of collisions (binary collisions or triple-partner collisions as indicated in Fig. 3.3) is determined by the gas pressure in the optical pumping cell. Under high pressure conditions mainly binary collisions between Rb and Xe atoms takes place leading to short living (1 ps) Rb-Xe complexes. At low gas pressures a Rb-Xe van der Waals molecule is formed in a triple partner collision with N_2. The life time of the Rb-Xe van der Waals molecule depends strongly on the gas pressure (e. g. 0.1 μs at 1 Torr [Hap2]), because it exists until the next collision with a N_2 molecule.
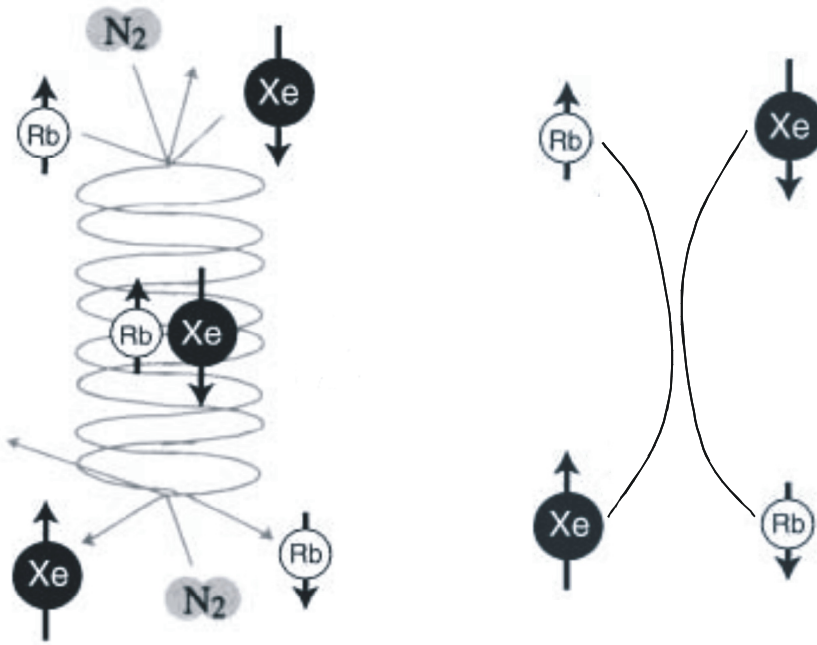
Fig. 3.3: Polarization of the Xe nuclei via collision and spin-exchange. Left: triple partner collision of Rb, Xe and N₂ at low gas pressures. Right: binary collision, that takes place at high gas pressures [Hap2].

During the life time of both kind of complexes the polarization transfer happens via hyperfine coupling (also called Fermi contact interaction) between the Rb electron and the Xe nucleus, because the Rb electron has a nonzero probability of being at the position of the Xe nuclear spin. The Fermi contact interaction between the electron spin S and the nuclear spin I can be described by the following equation:

$$\alpha S \cdot I = \frac{\alpha}{2}\left[S_{+}I_{-} + S_{-}I_{+}\right] + \alpha S_{z}I_{z} \ , \tag{3.2-1}$$

where the "flip-flop" term in brackets gives the spin-exchange between Rb and Xe and the coupling constant α defines the probability of finding the Rb electron at the nucleus of Xe, and is given by:

$$\alpha = \frac{8\pi}{3}\gamma_{S}\gamma_{I}\hbar^{2}\delta(r) \tag{3.2-2}.$$

Here $\delta(r)$ is the Dirac delta function which depends upon the relative distance between the electron and the nucleus. With a certain duration t_{p} of the optical pumping process the theoretically achievable Xe polarization P_{Xe} is given by [Dri2, Hap2]:

$$P_{Xe}(t_p) = \frac{\gamma_{SE}}{\gamma_{SE} + \gamma_w} \cdot \langle P_{Rb} \rangle \cdot \left\{ 1 - \exp^{-(\gamma_{SE} + \gamma_w)t_p} \right\},$$ (3.2-3)

where γ_{SE} is the rate of spin exchange, γ_w defines the relaxation due to collisions with the wall of the pumping cell and $\langle P_{Rb} \rangle$ is the averaged polarization of the Rb electrons. Far from the walls the spin exchange rate γ_{SE} origins mostly from collisions between Rb and the gases contained in the pumping cell and is proportional to the Rb atom density [Rb]:

$$\gamma_{SE} = \kappa_{SE}[Rb],$$ (3.2-4)

where the proportionality constant κ_{SE} is the spin-exchange cross section. Over time (seconds to hours depending on the experimental conditions) the nuclear polarization of Xe will accumulate, yielding values as high as several tens of percent. The Xe polarization can simply be measured by the comparison of the NMR signal amplitude of thermally and hyperpolarized Xe under the same experimental conditions. An indirect method to determine P_{Xe} is the measurement of the homogeneous dipole field arising from hyper-polarized Xe in a cylindrical sample tube [Ver]. The strength of the dipole field is proportional to the product of Xe density and polarization. In an NMR experiment this dipole field adds up with the external field and therefore changes the Larmor frequencies of all other nuclei contained in the sample tube. The advantage of this method is that no rf pulse is needed which consumes a part of the hyperpolarization.

3.3   Apparatus for hyperpolarization

The first setup of a Rb-Xe gas flow hyperpolarizer was invented by Driehuys et al. at Princeton University [Dri]. It was able to work in a continuous flow mode to deliver a gas stream of hyperpolarized Xe continuously to the sample or in a batch mode to accumulate hyperpolarized Xe ice. The hyperpolarizer used in this work is also constructed to work in both modes and was built at the research center Jülich by the group of S. Appelt. It is shown schematically in Fig. 3.6.
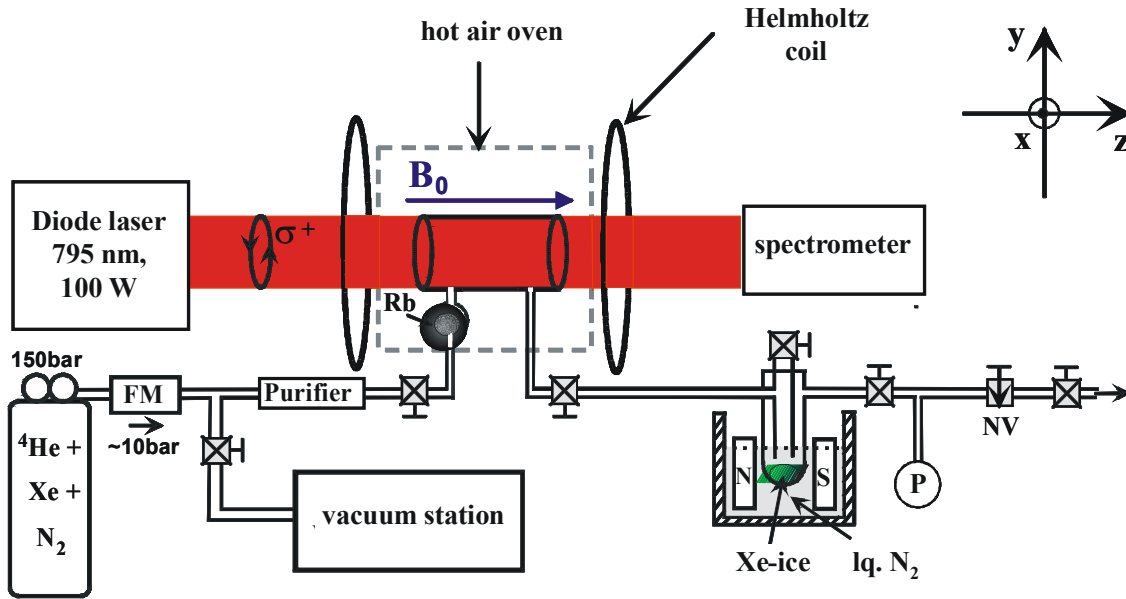
Fig. 3.4: Schematic drawing of the Rb-Xe gas flow hyperpolarizer with accumulation unit for Xe ice.

The gas mixture used for hyperpolarization consists of 98% Helium, 1% Nitrogen and 1% Xenon (natural abundance of ^{129}Xe) at a pressure of 7 bar. The gas flow through the pumping cell and the whole apparatus can be regulated by a needle valve and controlled by a flowmeter (FM). The typical flow rate used was about 300 cm^3/min. The pumping cell which consists of a borosilicate glass cylinder (inner diameter: 2.4 cm, length: 7 cm) and the Rb reservoir (1 g Rb applied on a copper mesh) are surrounded by a hot air oven in order to evaporate the Rb to the gas phase. The temperature for optical pumping used in this work varied in the range of 160-180°C. The Rb vapor is transported by the ^{4}He, N$_2$, Xe gas stream inside the optical pumping cell which is exposed to a laser beam of circular polarized light with a wave length of 795 nm. The laser beam is shielded by an aluminum box in order to ensure maximum security. The optical pumping cell is centered in a pair of Helmholtz coils that produce a homogeneous magnetic field of 70.7 G, which is necessary for the optical pumping process. During the time the Xe atoms need to pass the optical pumping cell (depending on the gas flow rate between a few seconds and half a minute) they get hyperpolarized by spin-exchange optical pumping. In the batch mode the gas stream containing the hyperpolarized gas is flowing through a plastic tube inside the freezing unit where the Xe is separated at the temperature of liquid nitrogen (77 K) from the quenching gases and accumulated as Xe ice. The polarization of the Xe ice inside the freezing unit was maintained by a Halbach magnet with an approximate field strength of 1000 G. The

longitudinal relaxation time of ^{129}Xe which determines the life time of the hyperpolarization is more than 2 hours at a temperature of 77 K and a magnetic field strength of more than 500 G [Dri, Gat, Kuz, Bae]. When the hyperpolarized Xe was used in a continuous flow mode, it was flowing through a 7 meter plastic tube directly into the sample cell which was positioned in a 200 MHz spectrometer. During the transit time to the fringe field of the spectrometer the hyperpolarized Xe experienced no magnetic field, but due to the short transit time of 50 s the depolarization was assumed to be negligible. The total degree of polarization which was achieved by this hyperpolarizer varied in the range of 20% to 35 % depending on the experimental conditions [App4].

4 Experimental

All NMR experiments were performed using a Bruker DSX 200 spectrometer with a field strength of 4.7 T. The spectrometer has a vertical bore of 89 mm diameter and is equipped with an x,y,z-imaging system with a maximum gradient strength of about 1 T/m. The spectrometer has a standard Bruker temperature controll system which can be used in a temperature range from 150 K to 360 K. For rf irradiation a 20 mm standard birdcage coil was used operating at a ^{129}Xe resonance frequency of 55.3 MHz.

For measurements with thermally polarized Xe at different pressures a sapphire tube (4.89 cm^3 volume) sealed by a titanium valve was used which was approved for pressures up to 50 bar. The sapphire tube was constructed by K. Kupferschläger at the RWTH Aachen University and is shown in Fig. 4.1.
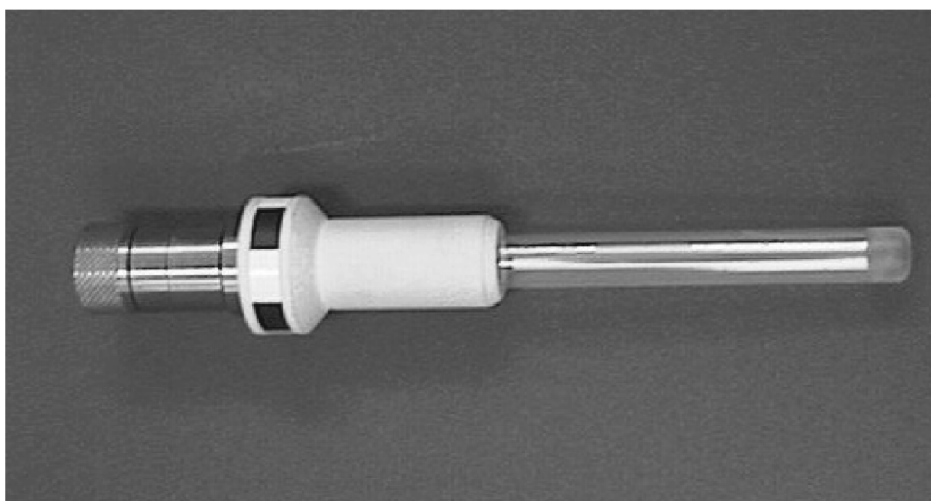
Fig. 4.1: NMR sapphire sample tube for high pressure measurements with a titanium valve. The length of the tube (without valve) is 12.7 cm and the inner diameter 7 mm.

The pressure tube was loaded with Xe gas at natural abundance and defined pressures at a filling station equipped with a pressure gauge in order to carefully control the applied Xe pressure. The Xe gas pressure has significant influence on the chemical shift as is shown in detail in chapter 1.

The measurements with hyperpolarized Xe were performed using the hyperpolarizer which was introduced in chapter 3.3. It is shown in Fig. 4.2. It consists of the following parts: 1. 100 W laser, 2. optics with laser beam shielding, 3. optical pumping cell centered in a magnetic field produced by Helmholtz coils housed in a heating chamber, all surrounded by an aluminum box in order to shield the laser beam, 4. manometer, 5. flowmeter, 6. high vacuum station, 7. infrared camera used for controlling of hyperpolarization process.
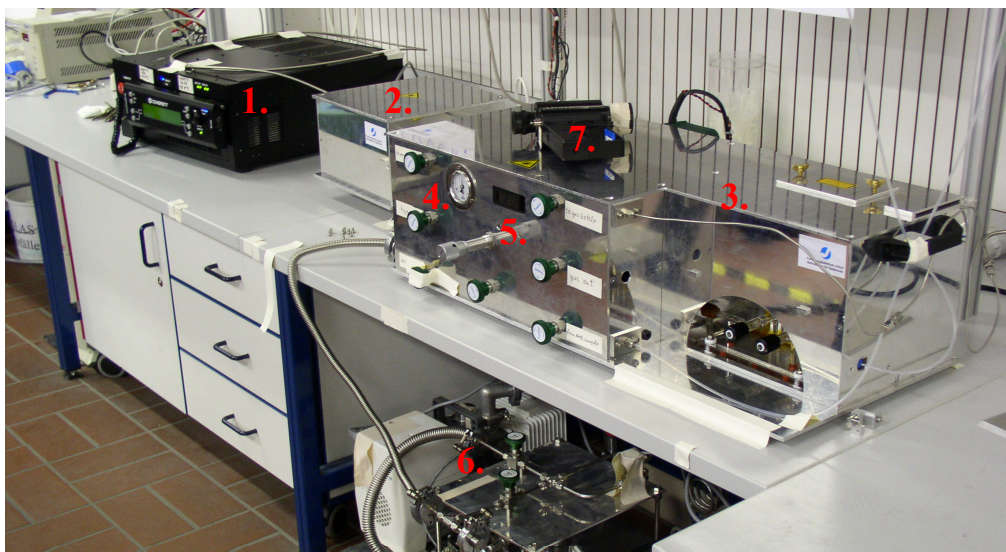

Fig. 4.2: Portable Rb-Xe hyperpolarizer located in the Magnetic Resonance Center of the RWTH Aachen University. It was developed and constructed by S. Appelt and coworkers in the research center Jülich.

The sample cell that was used for the experiments with hyperpolarized Xe was also constructed at the research center Jülich and is shown in Fig. 4.3. Two different sample tubes can be attached to it, one with a diameter of 7 mm and a bigger one with a diameter of 16 mm. The probe can be used to work in continuous flow mode or for accumulation of hyperpolarized Xe ice. A detailed description of the used experimental setup and conditions as well as the most important NMR parameters will be given for the individual measurements in each chapter.
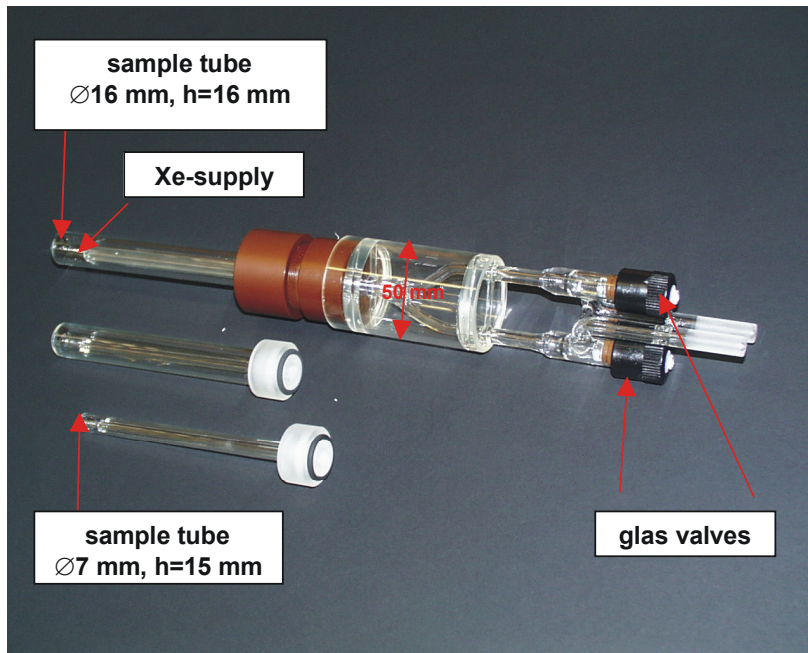
Fig. 4.3: Probe for measurements with hyperpolarized Xe. It consists of an inflow and an outflow part and can be used in the continuous flow mode or for accumulation of hyperpolarized Xe ice. Two sample tubes with different diameters can be attached.

5 A quantitative study of the chemical shift of ^{129}Xe in organic solvents

This chapter is devoted to ^{129}Xe NMR with only spectroscopic resolution, because it is inevitable to earn a basic knowledge about the chemical shift behavior of Xe in the dissolved phase at the beginning of this work. In this chapter a new analytical model will be introduced which allows the quantitative evaluation of the Xenon chemical shift in the gas and liquid phases and also of Xe dissolved in organic solvents. Extensive measurements of the chemical shift of thermally polarized Xenon were performed as a function of temperature (150-295 K) and Xe density (1- 400 amagat). Based on these measurements and the theory of the chemical shift, a simplified phenomenological model of the chemical shift of Xe is developed, which allows the calculation of the chemical shift as a function of temperature and Xe density by an analytical function with only a few fitting parameters. This chapter will therefore give the basis for the interpretation of the results of the following chapters.

5.1   Introduction

As described in chapter 2, Xe atoms have the useful property for materials science, biology or medicine to report very sensitively on their physical and chemical environment by their wide range of chemical shift. In order to use Xe as a probe for different environments in the liquid phase, which is the subject of many investigations in biology, it is inevitable to understand the chemical shift of dissolved Xenon in detail. However, no quantitative model for the chemical shift of Xe dissolved in liquids exists so far. A good example for the benefit that a quantitative model provides for the practical application of Xe NMR in material science is the model for the determination of pore sizes in porous media [Rip, Der, Dem, Che2] which led to many applications of Xe NMR [Ito, Raf2, Chm, Raf3, Rat, Ter, Nos, Jam, Sea, Stu, Mou].

Pure Xe systems like Xe gas, liquid or ice have already been investigated a long time ago. In the 1970s, Jameson et al. published the first model for the chemical shift of different noble gases as a function of temperature and density based on ab initio calculations and NMR measurements [Jam3, Jam5, Jam6]. They were able to specify the first and second coefficient of the virial expansion which describes the chemical shift of Xe in the gas phase up to pressures of 50 bar. Jameson et al. also investigated Xenon gas mixed with other rare gases,

like Krypton and Argon [Jam4] and found that the second virial coefficient of the chemical shielding depends on the atomic pair (Xe-Xe, Xe-Ar, Xe-Kr). For the case of pure liquid Xenon the first chemical shift data were already determined in 1966 by Brinkmann et al. [Bri], who found a linear dependence of the chemical shift on temperature. Yen and Norberg measured the chemical shift of solid Xe and established a correlation between the line width and the temperature [Yen].

More recently, several groups worked on techniques to accumulate and store hyper-polarized Xe. For that purpose the chemical shift data of Xe in the storage medium and its longitudinal relaxation time T_1 were also determined. In most cases, Xenon is accumulated as a solid in a magnetic field (> 0.1 T) and then applied as Xe gas after evaporation. The polarization loss of solid Xe at 77 K and 1000 G is negligible due to the small T_1 relaxation rate of 10^{-4} s^{-1} [Kuz]. A different approach to store hyperpolarized Xe is to dissolve it in another compound. In 2001, Patton et al. published the chemical shift data of hyperpolarized Xe dissolved in liquid nitrogen as a function of temperature and observed a linear dependence of the ^{129}Xe chemical shift on the N_2 density [Pat]. They estimated the Xe T_1 relaxation time in liquid nitrogen to be of the order of 2 hours. Ishikawa et al. proposed deuterated ethanol as a storage medium for hyperpolarized Xe based on T_1 values of 1000 s at 5.4 mT measured in this system at atmospheric pressure and above the boiling point of Xe [Ish].

The motivation for this study was not only to gather basic knowledge of the chemical shift behavior of Xe dissolved in liquids but also to find a suitable solvent storage medium for hyperpolarized Xe. Therefore measurements with hyperpolarized Xe dissolved in ethanol and toluene were performed and an interesting difference in the chemical shift of Xe dissolved in high quantities in these two solvents was found which is depicted in Fig. 5.1. It shows spectra of hyperpolarized Xe dissolved in different quantities in ethanol and toluene. The experiments with low Xe densities were performed in the continuous flow mode of the Rb/Xe hyperpolarizer. The partial pressure of Xe in the gas mixture used for hyperpolarization was 0.07 bar, which results in different Xe densities dissolved in the same amount of ethanol (0.175 amagat) or toluene (0.35 amagat) due to the different Ostwald coefficients (2.5 for Xe in ethanol [Joh] and 5 for Xe in toluene) of Xe in these liquids. For the measurements with hyperpolarized Xe in higher concentrations solid Xe was accumulated at the temperature of liquid nitrogen on top of the frozen liquids. After heating the sample to room temperature, the NMR spectra for high Xe densities were acquired.
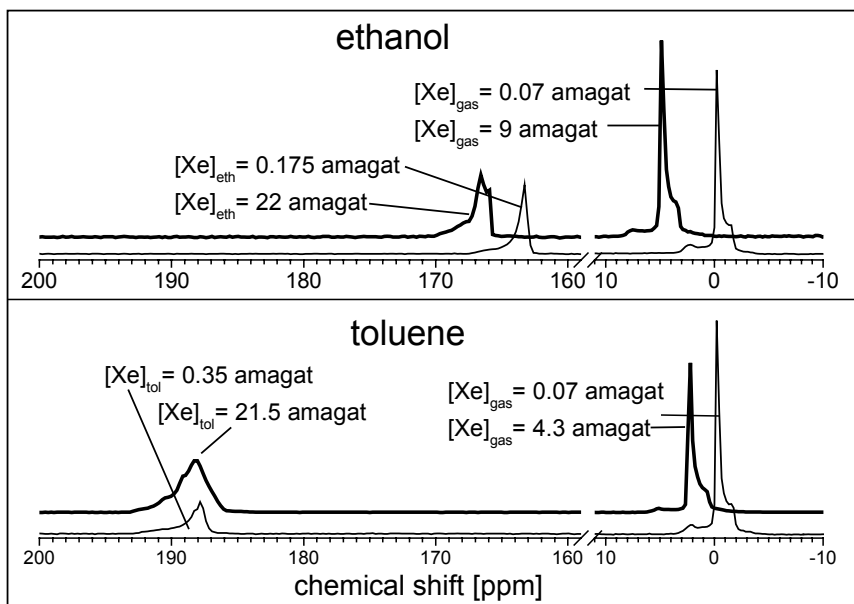
Fig. 5.1: Spectra of hyperpolarized Xe dissolved in different quantities in ethanol (top) and toluene (bottom) at room temperature. Note, that with a high amount of Xe in ethanol, the chemical shift of Xe dissolved in ethanol increases significantly whereas the chemical shift for Xe dissolved in toluene remains constant also for higher Xe densities.

The Xe density in the gas phase can be determined from the chemical shift of the Xe gas line following a procedure which will be described in detail later; afterwards the Xe density dissolved in the different liquids can be calculated from this knowledge and from the Ostwald coefficients. In Fig. 5.1, the difference in the chemical shift of Xe in ethanol and toluene is obvious. Whereas the chemical shift of Xe at high concentrations in ethanol is significantly increased compared to the low density spectrum, the chemical shift of Xe dissolved in toluene remains the same for different densities of Xe. No quantitative study of the chemical shift of Xe dissolved in liquids could be found in the literature which explains this result and therefore this study investigates the chemical shift of Xe in ethanol and toluene in dependence of temperature and density in detail.

5.2 Experimental

The experiments were performed with thermally polarized Xe in order to study a higher density range than can be achieved by accumulating hyperpolarized Xe. Furthermore the use of thermally polarized Xe allows measurements in thermal equilibrium of the gas phase and the Xe atoms dissolved in the liquids. For all experiments the same sapphire sample tube (4.89 cm^3 volume) sealed by a titanium valve was used (see chapter 1). For the experiments with pure Xe, the tube was filled at room temperature with different amounts of Xe gas (4, 16, 31 bar) in natural abundance. A small amount of oxygen (0.2 bar) was added in order to

shorten the T_1 relaxation time which has no effect on the Xe chemical shift [Jam3, Jam4, Jam5]. For the Xe/solvent experiments, 0.3 cm^3 solvent was filled into the sapphire tube at room temperature and different amounts of Xe gas were added (also 0.2 bar oxygen). The initial amount of Xe dissolved in a liquid is given by the Ostwald coefficient, which is defined as the ratio of the Xe density in solution divided by the Xe density in the gas phase. The NMR experiments were performed with a 4.7 Tesla DSX Bruker spectrometer equipped with a standard cooling system and a 20 mm birdcage coil operating at a Xe resonance frequency of 55.3 MHz. The samples were cooled down slowly in several steps from 295 K to 150 K in such a way that the Xe gas and liquid phase were in thermal equilibrium, and at each temperature an NMR spectrum was acquired.

The flip angle (50°), repetition time (15 s) and receiver gain were the same for all experiments but the number of averages was increased at low Xe concentrations in order to obtain a similar signal-to-noise ratio in all experiments. The temperature was measured with a Pt100 sensor, which was placed in the cooling gas stream 1 cm below the sample tube. For the whole temperature range, the temperature sensor was calibrated in separate runs against a second calibrated temperature sensor which was placed within the liquid inside the sapphire tube. This procedure was repeated for each liquid.

5.3   The model

The very basic equation which describes the chemical shift in NMR can be written as:

$$\delta = \frac{B_{loc} - B_{loc}^{ref}}{B_0} = \sigma^{ref} - \sigma \,, \tag{5.3-1}$$

with δ being the chemical shift (a dimensionless quantity), B_{loc} the local magnetic field which is experienced by the observed nucleus, B_{loc}^{ref} the local magnetic field of a reference nucleus, and σ and σ^{ref} the shielding of the observed and the reference nucleus [Abr, Blü2]. The shielding defines the interaction of the observed nucleus with its surrounding nuclei which causes a deviation from the external magnetic field B_0 at the place of the nucleus of interest $B_{loc} = (1-\sigma)B_0$. The shielding is a tensor which is reduced to its isotropic value in

the gas and liquid phases due to fast rotational motion which averages out the anisotropic parts of the tensor.

Following Buckingham, Streever, and Jameson [Buc, Str, Jam3, Jam6, Jam7] the nuclear shielding of Xe gas $\sigma(T,[Xe])$ can be described by a virial expansion

$$\sigma\left(T,[Xe_{gas}]\right)=\sigma_0(T)+\sigma_1(T)\left[Xe_{gas}\right]+\sigma_2(T)\left[Xe_{gas}\right]^2+\dots.., \qquad (5.3\text{-}2)$$

where $\sigma_1(T)$ and $\sigma_2(T)$ are defined as the second and third virial shielding coefficients, which depend on the temperature T and the Xe gas density $[Xe_{gas}]$. For Xe gas with a density below 50 amagat the shielding is sufficiently described by the first and second virial coefficient of equation 5.3-2, which will be proven by experimental results. For Xe gas the first virial coefficient $\sigma_0(T)$ describes the shielding in the limit of zero Xe density and therefore isolated Xe atoms and is by definition set to zero. Equation 5.3-2 reduces with this definition to $\sigma(T,[Xe_{gas}])=\sigma_1(T)\left[Xe_{gas}\right]$. Buckingham showed that the second virial coefficient can be expressed as

$$\sigma_1(T)=\int_0^\infty 4\pi r_a^2\cdot\left[\sigma(r_a)-\sigma(\infty)\right]\cdot\exp\left(-\frac{V_{pot}(r_a)}{kT}\right)d\,r_a, \qquad (5.3\text{-}3)$$

where $\sigma(r_a)$ is the intermolecular shielding function for Xe atoms at a distance r_a, and $\sigma(\infty)$ corresponds to the isolated Xe atoms. $V_{pot}(r_a)$ is defined as the intermolecular potential function, which qualitatively looks similar to the anharmonic (black curve) potential function shown in Fig. 5.2.

Jameson et al. showed that the shielding function $\sigma(r_a)-\sigma(\infty)$ consists of a sum of paramagnetic $\sigma^{par}\approx-\sigma_0^{par}/r_a^6$ and diamagnetic $\sigma^{dia}\approx\sigma_0^{dia}/r_a$ contributions $\sigma(r_a)-\sigma(\infty)=\sigma^{par}+\sigma^{dia}$ [Jam7]. They found that for the approaching noble gas pair the negative paramagnetic contribution is larger than the positive diamagnetic part and therefore the total shielding for an interacting noble gas pair is weaker than that of the isolated atom and the resulting chemical shift is positive.
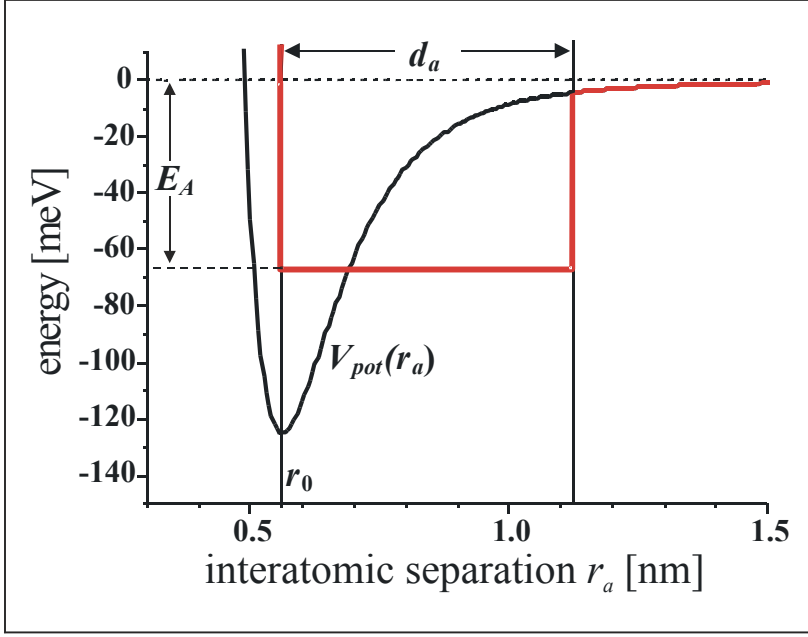
Fig. 5.2: Schematic drawing of the interatomic potential $V_{pot}(r_a)$ of two Xe atoms as a function of the interatomic separation r_a. In the model presented here the anharmonic potential function $V_{pot}(r_a)$ is substituted by a constant potential wall for short range interactions (red line), which is characterized by the activation energy E_A and the width d_a, and a long range potential $(r_a > r_0 + d_a)$, which is identical with $V_{pot}(r_a)$ and satisfies the condition $V_{pot}(r_a) << kT$.

The model of Buckingham can only be solved by ab initio calculations and requires the knowledge of the intermolecular potential function $V_{pot}(r_a)$ [Jam7, Mai2]. Here an analytical "binary" model is presented which is a good approximation of equation 5.3-3 and is depicted in Fig. 5.2 by the red line. For this model, the interatomic potential is divided into a short range and a long range interaction. For the short range interaction the potential function at $r_0 < r_a < r_0 + d_a$ can be replaced by a potential wall with width d_a and height E_A. For the long range interaction $(r_a > r_0 + d_a)$ the potential is the same as $V_{pot}(r_a)$ and the absolute value of the potential fulfils the condition $V_{pot}(r_a) << kT$. Therefore the exponential part in equation 5.3-3 can well be approximated by $\exp(-V_{pot}(r_a)/kT) \approx 1 - V_{pot}(r_a)/kT$. For the short range interaction the chemical shielding is assumed to be a sum of paramagnetic and diamagnetic contributions $\sigma(r_a) - \sigma(\infty) = -\sigma_0^{par}/r_a^6 + \sigma_0^{dia}/r_a$, whereas for the long range interaction the shielding is dominated by the paramagnetic part $\sigma(r_a) - \sigma(\infty) = -\sigma_0^{par}/r_a^6$ [Jam7]. The integral in equation 5.3-3 can be evaluated for the two regions $r_0 \leq r_a \leq r_0 + d_a$ and $r_0 + d_a < r_a < \infty$ which leads to:

$$\sigma_1(T) = \alpha_1 + \alpha_2 \cdot \exp\left(-\frac{E_A}{kT}\right) + O\left(\frac{1}{kT}\right), \qquad (5.3\text{-}4)$$

with the coefficients α_1 and α_2 given by

$$\alpha_1 = -\frac{4}{3}\pi\sigma_0^{par}(r_0 + d_a)^{-3} \qquad (5.3\text{-}5)$$

$$\alpha_2 = -\frac{4}{3}\pi\sigma_0^{par}\left[r_0^{-3} - (r_0 + d_a)^{-3}\right] + 2\pi\sigma_0^{dia}\left[(r_0 + d_a)^2 - r_0^2\right]. \qquad (5.3\text{-}6)$$

The function $O(1/kT)$ is linear in $V_{pot}(r_a)/kT$ and much smaller than α_1 and α_2, therefore it will be neglected for further considerations. The coefficient α_1 of equation 5.3-4 represents the temperature independent part of the chemical shift which arises from long range Xe-Xe or Xe-solvent interactions. The term $\alpha_2 \cdot \exp(-E_A/kT)$ determines the temperature dependent chemical shift contribution due to short range Xe-Xe or Xe-solvent interactions.

5.4   Results I: pure Xenon system

The validity of the model will first be proven by experiments on a simple system, which is pure Xe, before it is applied to a more complicated system like Xe dissolved in a second compound. Figure 5.3 shows a stack plot of Xe NMR spectra measured with an initial gas pressure of 16 bar. The spectra are referenced to Xe gas at zero Xe density, determined by measuring Xe gas at different pressures and linear interpolation to zero Xe density.

Three different Xe phases can be distinguished by their chemical shift: Xe gas, liquid Xe and Xe ice as is depicted in Fig. 5.3. The cooling process was slow enough so that the three phases coexist in thermodynamic equilibrium according to the p,T phase diagram shown in Fig. 2.2. In the temperature range between 295 K and 222 K an isochore cooling process takes place because the Xe density $\lfloor Xe_{gas} \rfloor$ did not change with decreasing temperature as long as no Xe gas condensed in the liquid phase. An increasing chemical shift for the Xe gas line with decreasing temperature can be observed. At 215 K the boiling point of Xe is reached and the Xe gas begins to condense into the liquid phase. Therefore, the Xe density in the gas phase decreases resulting in decreasing chemical shift of the Xe gas peak. At 168 K only a small quantity of Xe gas with low pressure is left as is indicated by its chemical shift being close to zero. The Xe chemical shift of liquid Xe is increasing with decreasing temperature,

and at 160 K the liquid Xe crystallizes to solid Xe ice (melting point: 161.3 K at 0.8 bar) resulting in a Xe line at 294 ppm.
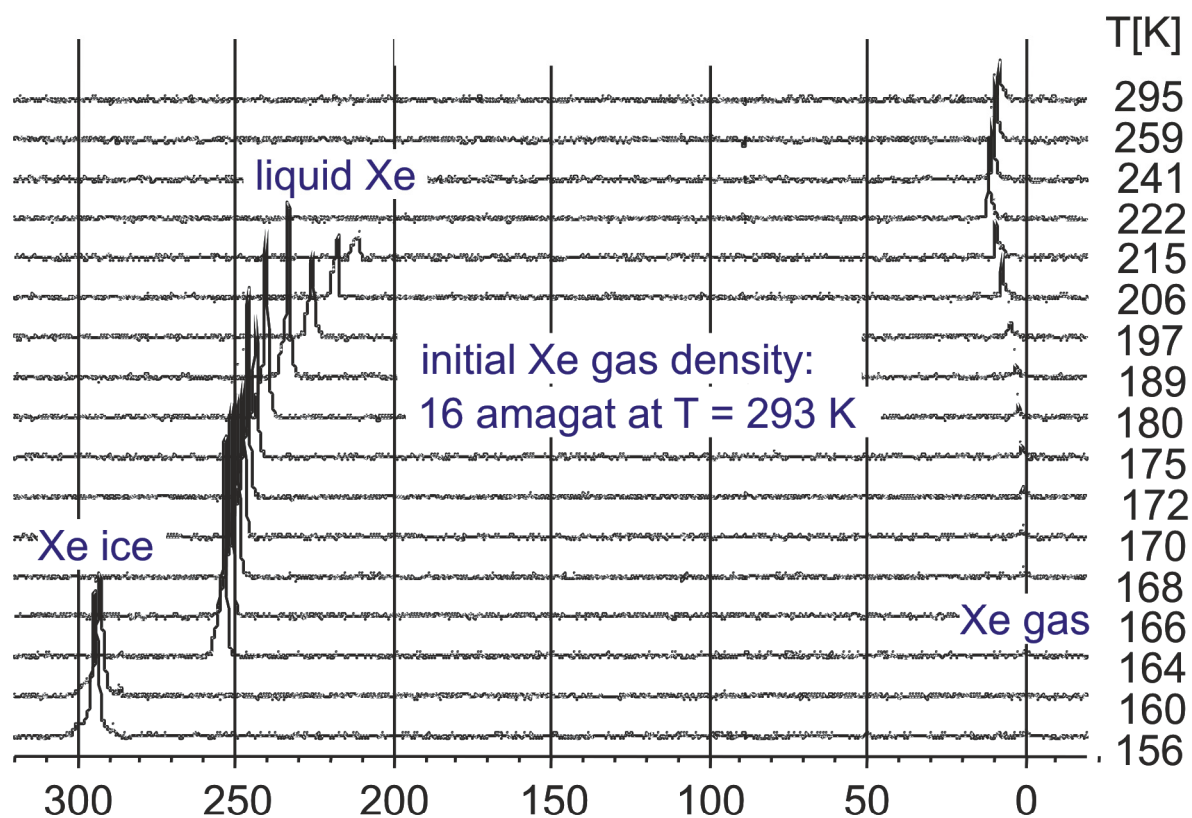

Fig. 5.3: Stack plot of Xe NMR spectra at different temperatures. The initial gas pressure at room temperature was 16 bar. The plot shows three signals originating from the three phases of Xe gas, liquid and ice.

The positive chemical shift values for Xe atoms in contact with each other (like in the gas phase at high pressure or in the liquid and solid phases) correspond to a deshielding effect as can be seen from equation 5.3-1. The interactions of Xe atoms (like collisions) lead to deformations of the Xe electron cloud and therefore change the local magnetic field that the Xe nuclei experiences. This is not the case for the isolated Xe atom, that is referenced to zero ppm. In the following the chemical shift of gaseous and liquid Xe will be discussed individually.

Pure Xe gas:

The measurement shown in Fig. 5.3 was also done for initial Xe gas pressures of 4 and 31 bar. From these measurements the chemical shifts of the Xe gas peak during the cooling process

were extracted and plotted in Fig. 5.4(a). The triangles, circles and squares are associated with the initial Xe gas pressures at room temperature of 31, 16 and 4 bar, respectively.
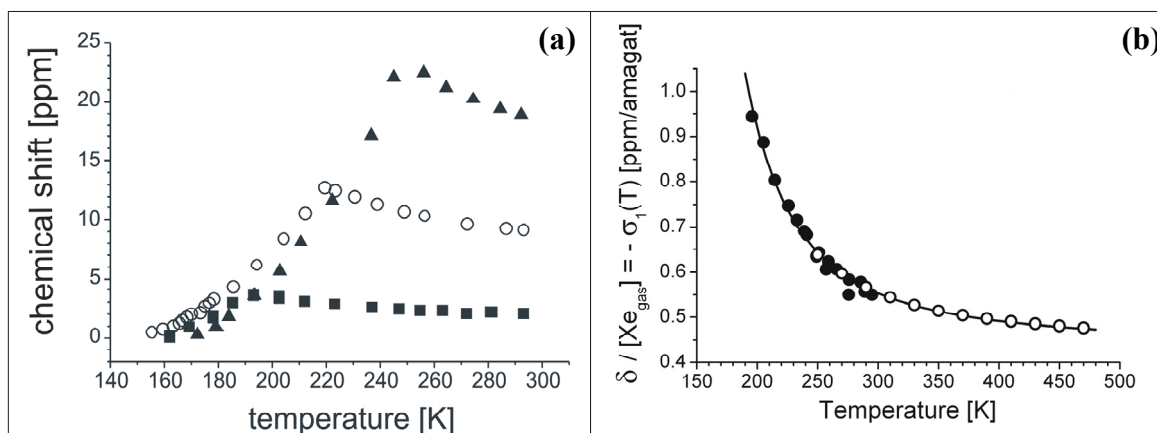

Fig. 5.4: (a) Plot of the chemical shift in ppm of Xe gas versus temperature in K for the three initial gas pressures (295 K) of 4 bar (squares), 16 bar (circles), and 31 bar (triangles.) (b) Normalized Xe chemical shift $\delta/[Xe_{gas}] = -\sigma_1(T)$ in units of ppm/amagat of the Xe gas versus temperature, obtained from each data set in (a) by division by the corresponding initial Xe gas density. The filled circles correspond to own measurements and the open circles to data from Jameson [Jam7]. The solid line corresponds to the fit of the presented model function (Eq. 5.3.4), which fits well to all measured data.

The same chemical shift behavior can be observed for all three initial Xe gas densities; the chemical shift increases with decreasing temperature during the isochore cooling process, until the boiling point of Xe is reached which is different for different Xe pressures (see p,T phase diagram in Fig. 2.2). With the beginning of the condensation process, the chemical shift of Xe gas starts to decrease, because the Xe gas density is decreasing.

In Fig. 5.4(b) the normalized chemical shift data of Xe gas $\delta/[Xe_{gas}] = -\sigma_1^{Xe-gas}(T)$ are plotted versus temperature. For normalization, the data points of the three measurements were taken which correspond to the isochore cooling process (from 295 K until δ reaches its maximum) and divided by their corresponding initial Xe gas density. The filled circles correspond to the data points of the measurements of the initial Xe density of 4 bar at 295 K. For the sake of clarity the plot of the chemical shift data of the measurements at 16 bar and 31 bar Xe gas density were omitted, although the data points fit very well to the curve defined by the filled circles. This proves the validity of the approximation that in the virial expansion in equation 5.3-2 the first two virial coefficients are sufficient to describe the chemical shift of Xe gas for temperatures down to 193 K and for Xe gas densities up to 31 amagat and that the first coefficient which is independent of the Xe density can be set to zero. The open circles in Fig. 5.4(b) correspond to measurements of Jameson et al. [Jam7] in the temperature range

between 250 K and 450 K which agree well with measurements presented here in the common temperature range. Both data sets can be well fitted by equation 5.3-4 (solid line in Fig. 5.4(b)) which yields the fitting parameters $\alpha_1^{Xe-gas} = 0.42 \pm 0.01$ ppm/amagat, $\alpha_2^{Xe-gas} = 0.0097 \pm 0.0025$ ppm/amagat and an average activation energy for each Xe-Xe pair of $E_{Xe}^{gas} = -66 \pm 4$ meV.

The important result of the measurements of Xe gas is that the model described in equation 5.3-4 is valid and the analytical form of the model has a very useful consequence. Now it is possible to determine precisely the Xe density $\left[Xe_{gas}\right]$ in the gas phase at each temperature from the measured chemical shift of a Xe gas line. Considering a closed sample tube containing a known amount of Xe gas together with a solvent, it is possible to quantify the amount of Xe dissolved in the liquid at a certain temperature. $\left[Xe_{dis}\right](T)$ can be calculated by taking the initial Xe concentration in the liquid at room temperature (given by the Ostwald coefficient which can be found in the literature for most systems), adding the amount of Xe which is given by the initial Xe density in the gas phase, and subtracting the Xe gas density at a certain temperature which is determined by the chemical shift of the Xe gas line. This procedure will be used in the following sections.

Pure liquid Xe:

The chemical shifts δ_{Xe}^{lq} of pure liquid Xe are presented in Fig. 5.5(a) as a function of temperature. The data were extracted from the measurements initial Xe gas pressures of 16 and 31 bar (filled circles). As can be seen from this figure, the chemical shift of liquid Xe covers a broad range and increases linearly with decreasing temperature. The open triangles correspond to measurements of Brinkmann et al. [Bri] and show exactly the same slope as the data presented here. In contrast to the gas phase the density of liquid Xe varies strongly with temperature (see open circles in Fig. 5.5(b) [Str2]). The increasing density of liquid Xe with decreasing temperature can be well described by a polynomial of order three: $\left[Xe_{lq}\right](T) = c_0 + c_1 \cdot T + c_2 \cdot T^2 + c_3 \cdot T^3$ with the fit parameters $c_0 = 973$ amagat, $c_1 = -5.82$ amagat/K, $c_2 = 0.026$ amagat/K^2 and $c_3 = -4.91 \cdot 10^{-5}$ amagat/K^3 [Str2].
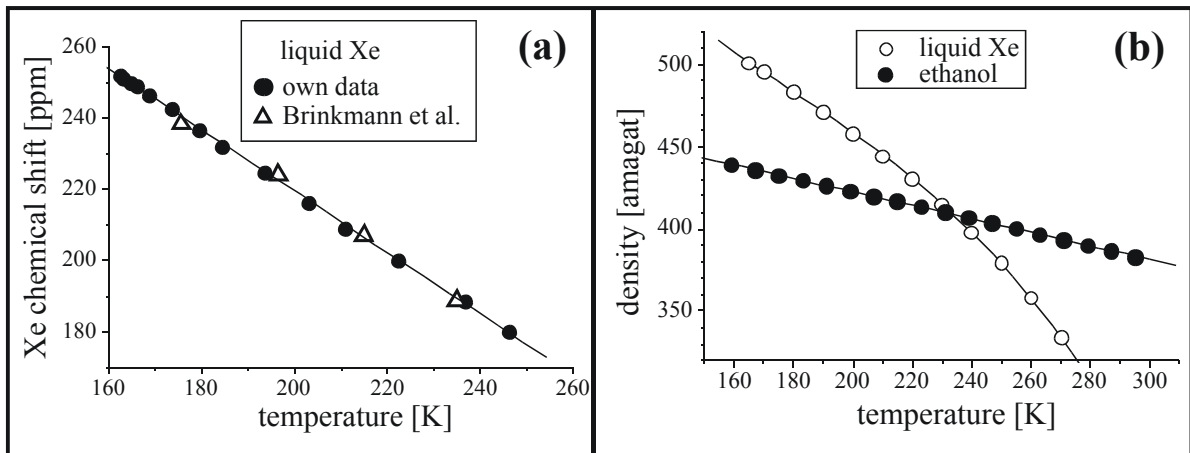
Fig. 5.5: (a) Chemical shift data of liquid Xe versus temperature (filled circles correspond to data measured in this work, open triangles to data measured by Brinkmann et al. [Bri]. (b) Density of liquid Xe (open circles, [Str2]) and ethanol (closed circles, [Smi2]) as a function of temperature.

With this knowledge and according to equation 5.3-1 it can be assumed that the chemical shift of liquid Xe can be expressed by $\delta_{Xe}^{lq}(T) = -\sigma_1^{Xe-lq}(T) \cdot [Xe_{lq}](T)$. The second virial coefficient $\sigma_1^{Xe-lq}(T)$ can be extracted from the known functional form of $[Xe_{lq}](T)$ and from the measured values for the chemical shift of liquid Xe, $\delta_{Xe}^{lq}(T)$. The model function in equation 5.3-4 for the case of liquid Xe reads as follows: $-\sigma_1^{Xe-lq}(T) = \alpha_1^{Xe-lq} + \alpha_2^{Xe-lq} \cdot \exp(-E_{Xe}^{lq}/kT)$, and can be fitted to the experimentally obtained values of $\sigma_1^{Xe-lq}(T)$ yielding the fitting coefficients of $\alpha_1^{Xe-lq} = 0.412 \pm 0.04$ ppm/amagat, $\alpha_2^{Xe-lq} = 0.026 \pm 0.02$ ppm/amagat, and the average activation energy for each Xe-Xe pair of $E_{Xe}^{lq} = -17.2 \pm 8$ meV. The values of α_1 and α_2 are nearly the same for Xe in the gas and liquid phases, but the activation energy of Xe gas is four times higher compared to the activation energy in the liquid phase. This experimental result can be explained by the fact that in the dense liquid phase the Xe atom is surrounded by more than one other Xe atom. The electrons of the Xe atoms in the liquid phase can be shared between all interacting Xe atoms and consequently the average activation energy per atomic pair is smaller than in the gas phase.

5.5   Results II: Xenon dissolved in organic solvents

In the last section it was shown that the analytical model that was introduced in Eq. 5.2-4 is valid for pure Xe systems like Xe gas or liquid Xe. Now it will be applied to the more complicated case of Xe dissolved in an organic solvent. As an example for the experimental results, Fig. 5.6 shows a stack plot of NMR spectra for a system that consists of 0.3 cm^3 ethanol and 16 bar Xe pressure at room temperature acquired at different temperatures between 295 K and 151 K.
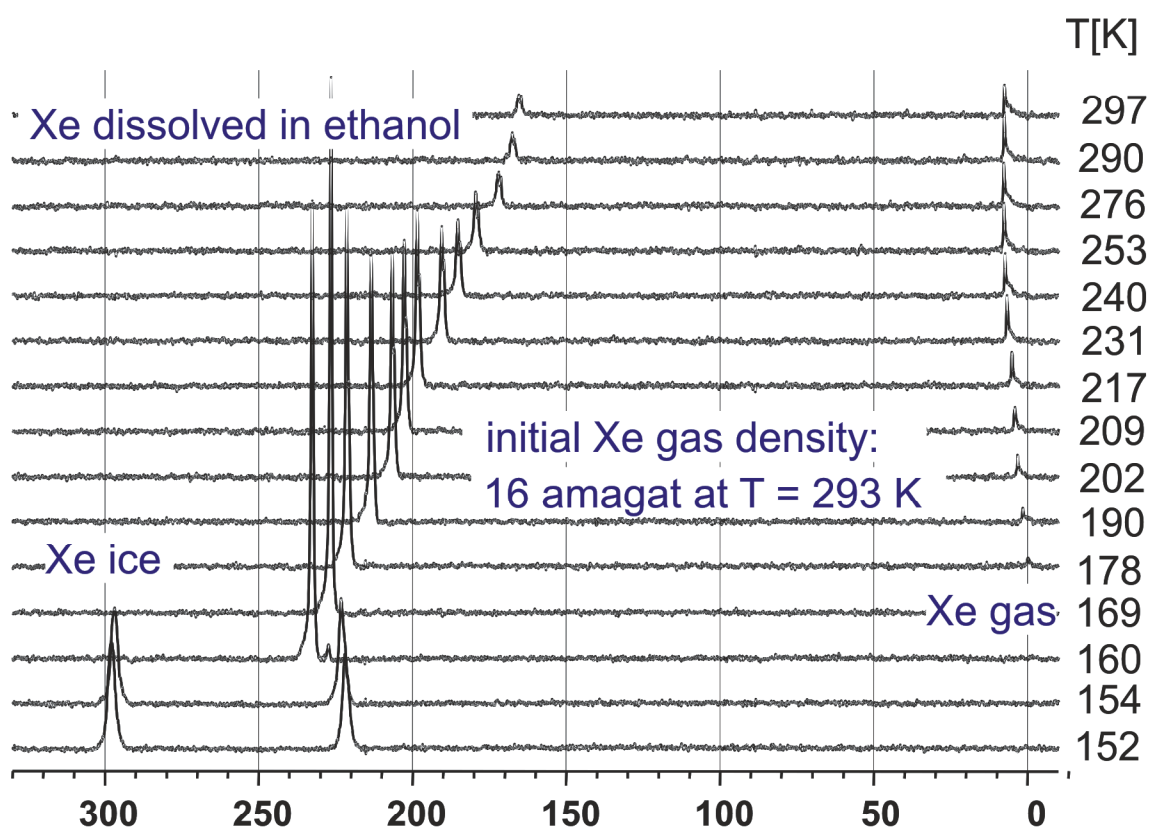

Fig. 5.6: Stack plot of NMR spectra for the two-component system 0.3 cm^3 ethanol and 16 bar initial Xe gas pressure at different temperatures. The chemical shift of Xe dissolved in ethanol increases strongly with decreasing temperature.

Like in the pure Xe system three Xe phases can be distinguished in the NMR spectra: the gas phase (δ_{Xe}^{gas} : 8 ppm at 297 K to 0.5 ppm at 178 K), Xe dissolved in ethanol (δ_{Xe}^{Eth} : 167 ppm at 297 K to 235 ppm at 160 K) and Xe ice (δ_{Xe}^{ice} : 295 ppm at 154 K to 298 ppm at 152 K). An important fact is that in the temperature range from 295 K to 161 K the chemical shift of Xe dissolved in ethanol increases strongly and starts to decrease at 154 K. This behavior can be explained by a decreasing Xe density inside the ethanol due to the Xe ice formation

which results in a decrease of Xe-Xe interactions at temperatures below the melting point of Xe.

To quantitatively evaluate the chemical shift of Xe dissolved in an organic liquid, that consists of the two basic contribution of Xe-Xe interactions and Xe-solvent interactions, δ_{Xe}^{sol} was measured as a function of temperature for four initial Xe concentrations. For two organic solvents (ethanol and toluene) Fig. 5.7 shows the dependence of chemical shift on Xe density and temperature.
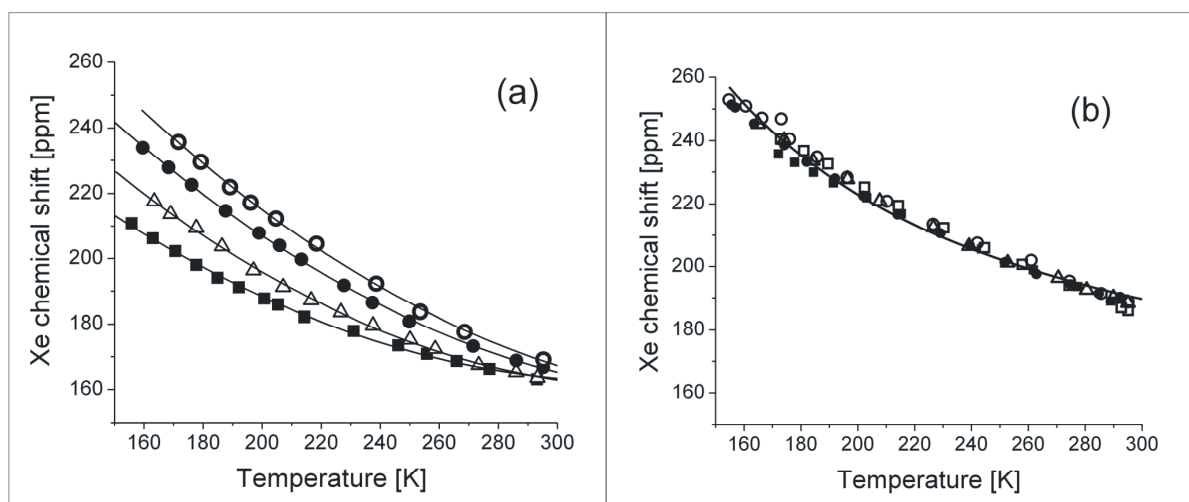

Fig. 5.7: (a) Chemical shift δ_{Xe}^{Eth} of Xe dissolved in 0.3 cm^3 of liquid ethanol versus temperature. (b) Chemical shift δ_{Xe}^{Tol} of Xe dissolved in 0.3 cm^3 of liquid toluene versus temperature. The open (filled) circles correspond to an initial Xe gas density (at 293 K) of 33 (16) amagat and the triangles (squares) to an initial Xe gas density of 7 (2) amagat. The open squares in (b) correspond to 4 amagat. The solid lines are guides for the eyes.

Figure 5.7(a) depicts the results for Xe dissolved in ethanol as a function of temperature with Xe density as parameter. Figure 5.7(b) shows the results for Xe dissolved in toluene. In both graphs the symbols represent the measurements with 2 amagat (filled squares), 7 amagat (open triangles), 16 amagat (filled circles), and 33 amagat (open circles) initial Xe density, respectively. In Fig. 5.7(b) the open squares correspond to an initial density of Xe gas of 4 amagat. For all measurements the chemical shift of Xe dissolved in ethanol increases monotonically with decreasing temperature. A strong dependence on Xe density of the chemical shift of Xe in ethanol is observed for a given temperature, which indicates that the chemical shift of Xe in ethanol strongly depends on the Xe-Xe interaction. For Xe in toluene the chemical shift is independent of the Xe density and no Xe-Xe interactions can be observed.

Figure 5.8 shows in the top part two-dimensional x-z ^{1}H-FLASH images of 0.3 ml pure ethanol (a) and 0.3 ml ethanol with 33 bar Xe at room temperature (b) and at 211 K (c). The images were acquired using the described NMR system but with a 20 mm proton birdcage coil operating at a proton resonance frequency of 200.5 MHz. A huge increase of the volume of the Xe-ethanol mixture is observed with decreasing temperature. The bottom part shows the corresponding two-dimensional x-z ^{1}H-FLASH images of 0.3 ml pure toluene (d) and 0.3 ml toluene with 16 bar Xe at 293 K (e) and 210 K (f). For toluene the increase of the volume of the mixture is much smaller than for ethanol although the Xe density is the same in both solvents due to an Ostwald coefficient of 5 for toluene and 2.5 for ethanol.

T = 293 K	T =293	T = 211 K
0.3 ml ethanol	0.3 ml ethanol	0.3 ml ethanol
Reference	+ 33 bar Xe	+ 33 bar Xe
T = 293 K	T = 293 K	T = 210 K
0.3 ml toluene	0.3 ml toluene	0.3 ml toluene
Reference	+ 16 bar Xe	+ 16 bar Xe

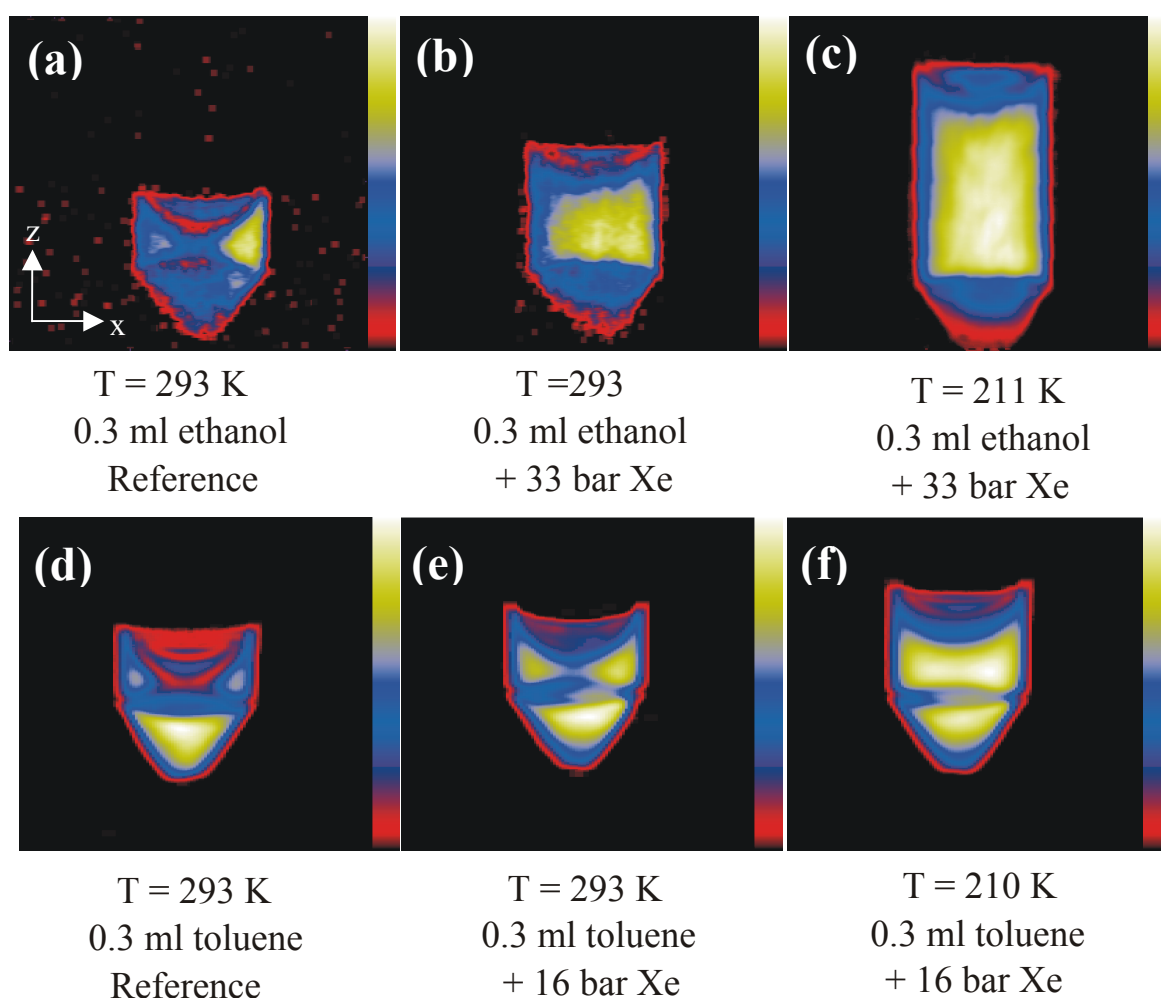**Fig. 5.8**: Top: (a) 2D x-z ^{1}H-FLASH images of 0.3 ml pure ethanol. (b) 0.3 ml ethanol with 33 bar Xe at room temperature and at 211 K (c). Bottom: 2D x-z ^{1}H-FLASH images of 0.3 ml pure toluene (a) and 0.3 ml toluene with 16 bar Xe at 293 K and 210 K. All images depict a field of view of 25 mm in both directions. The resolution in z-direction was 49 μm (read-encoding) whereas in x direction it was 195 μm (phase-encoding).

Combining the results of the chemical shift measurements and the volume of the mixtures, it can be concluded that the Xe atoms move freely between the ethanol molecules so that they can collide with each other. On the other hand, in toluene the Xe atoms seem to be captured preferably in the aromatic ring of a toluene molecule. This leads to a much smaller volume increase of the Xe-toluene mixture compared that of the Xe-ethanol mixture, and no Xe-Xe collisions are possible in the former. Apart from this qualitative considerations the chemical shift behavior of Xe dissolved in ethanol and in toluene will be analyzed in more detail.

Xe dissolved in ethanol

As a first approximation, the chemical shift of Xe dissolved in ethanol can be expressed as a sum of two basic contributions: the Xe-solvent interaction, which depends linearly on the ethanol density $[Eth]$ and is equivalent to the first virial coefficient $\sigma_0(T)$ in equation 5.3-4, and the Xe-Xe interaction, which is proportional to the Xe density $[Xe_{sol}]$ in solution

$$\delta_{Xe}^{Eth}(T) = -\sigma_0^{Xe-Eth}(T)\cdot[Eth](T) - \sigma_1^{Xe-Xe}(T)\cdot[Xe_{sol}](T). \qquad (5.5\text{-}1)$$

In order to quantify both contributions to the chemical shift, the ethanol density $[Eth]$ and the Xe density dissolved in ethanol $[Xe_{sol}]$ must be known for each temperature. $[Xe_{sol}]$ is given by the number of Xe atoms dissolved in ethanol N_{Xe}^{sol} divided by the volume of the Xe-ethanol mixture V_{total}^{Xe-Eth}. The number of Xe atoms which is dissolved in ethanol at room temperature is expressed by the Ostwald coefficient [Joh] and, N_{Xe}^{sol} can be calculated at different temperatures from the chemical shift of the Xe gas measured at a certain temperature and the initial Xe gas density as described in the results section for the Xe gas. The evaluation of N_{Xe}^{sol} is done in two steps: first the Xe density is calculated at a certain temperature in the gas phase above the ethanol from equation 5.3-4 using the measured chemical shift of the Xe gas and the fitting parameters determined for Xe gas. Afterwards, the total amount of dissolved Xe atoms can be calculated by:

$$N_{Xe}^{sol}(T) = N_{Xe}^{sol}(293K) + \left([Xe_{gas}](293K) - [Xe_{gas}](T)\right)\cdot V_{Xe}^{gas}(T). \qquad (5.5\text{-}2)$$

The value of N_{Xe}^{sol} (293K) is calculated from the initial Xe gas density and from the Ostwald coefficient of 2.5 of Xe in ethanol [Joh]. The total volume of the Xe-ethanol mixture V_{total}^{Xe-Eth} can be determined at each temperature by two-dimensional proton MRI, if a homogenous Xe-ethanol distribution is assumed. Hence, a series of x-z FLASH images for the cooling process for each initial Xe density was measured. Figure 5.8 can serve as an example showing three x-z FLASH images of the pure ethanol and of an ethanol-Xe mixture in the sample tube. The volume of the Xe-solvent mixtures increases significantly compared to the references of the pure solvents due to the high amount of Xe atoms that are dissolved in the liquid. With decreasing temperature this effect becomes even more pronounced as can be seen from the increased volume of the Xe-solvent mixtures in Fig. 5.8(c) and (f) because even more Xe atoms dissolve into the liquids at low temperatures. The total volume of the Xe-ethanol mixture at each temperature was determined by the height of the mixture in these images.

Now the density $[Xe_{sol}](T)$ of Xe dissolved in ethanol and the ethanol density $[Eth](T)$ can be evaluated from $N_{Xe}^{sol}(T)$ and $V_{total}^{Xe-Eth}(T)$ at each temperature, and the results are plotted in Fig. 5.9. Figure 5.9(a) shows that the density of Xe dissolved in ethanol increases with decreasing temperature until most of the Xe gas is dissolved into the liquid. For an initial Xe gas density of 33 amagat (see open circles in Fig. 5.9(a) the Xe density in ethanol is 270 amagat for temperatures below 180 K, which is very close to the Xe density in liquid Xe at 170 K of 335 amagat. This large amount of Xe, which can be accumulated in cold ethanol, proves the ability of cold solvents to serve as a storage medium for hyperpolarized Xe.
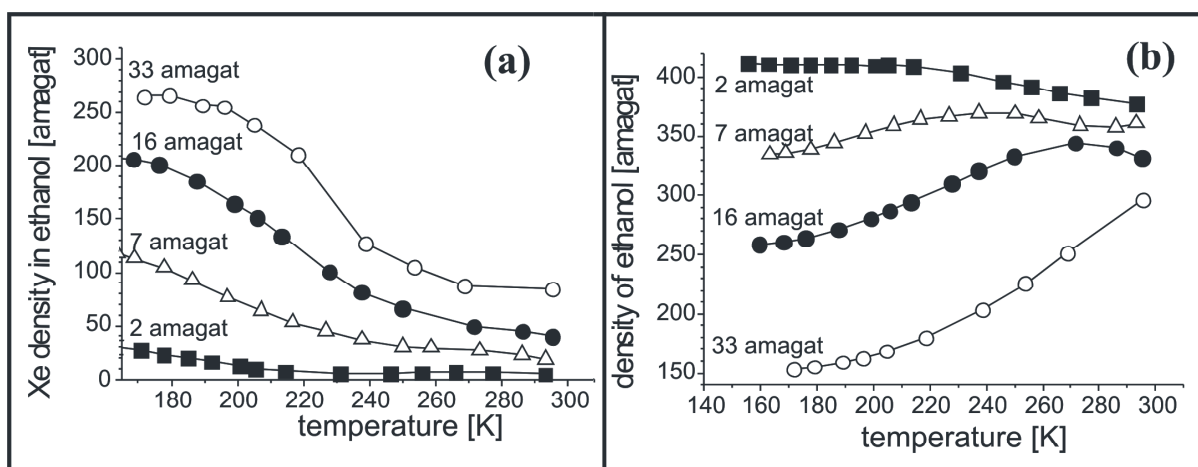

Fig. 5.9: (a) Xe density for Xe dissolved in ethanol versus temperature. (b) Ethanol density of the Xe-ethanol mixture as a function of temperature. The open (filled) circles correspond to 33 (16) amagat initial Xe gas density, the triangles (squares) to 7 (2) amagat initial Xe gas density.

The density of ethanol in the Xe-ethanol mixture shows the opposite behavior. At 2 amagat initial Xe gas density $[Eth](T)$ increases slightly with decreasing temperature because the volume of the Xe-ethanol mixture is dominated by the known thermal expansion of pure ethanol (see open circles in Fig. 5.5(b) [Smi2]). For the case of 33 amagat initial Xe gas pressure the ethanol density decreases significantly at lower temperatures, because a large amount of Xe is dissolved in the solvent therefore diluting the mixture from the viewpoint of ethanol.

Now that the Xe density in the gas phase and of the dissolved Xe is known, therefore the Ostwald coefficient, which is a measure of the solubility of a gas in a liquid, can be determined as a function of temperature. The Ostwald coefficient is given by the ratio of the densities of dissolved Xe and Xe gas and is plotted versus temperature in Fig. 5.10 for the measurements of 33 bar (open circles) and 16 bar (filled circles) initial Xe gas pressure, respectively
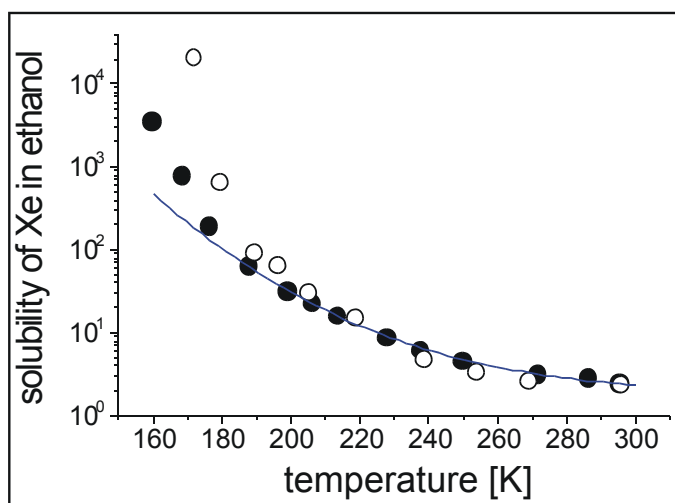

Fig. 5.10: Ostwald coefficient of Xe in ethanol as a function of temperature for the measurements with 33 bar (open circles) and 16 bar (filled circles) initial Xe gas pressure. The solid line corresponds to an exponential fit to the data points for 16 bar initial Xe pressure for temperatures above 190 K.

For temperatures in the range between 295 K and 200 K the solubility of Xe in ethanol increases exponentially with decreasing temperature for both data sets as can be seen from the solid line in Fig. 5.10 which depicts an exponential fit to the data points of 16 bar initial Xe pressure in this temperature range. From this fit the activation energy for the Xe dissolution in ethanol was found to be –192 meV. In this temperature range above the boiling point of ethanol the solubility of Xe in ethanol is independent of the initial Xe gas density, because at this temperatures the solubility depends predominantly on Xe-ethanol interaction due to the high ethanol concentration in the mixture. For temperatures below 200 K the data points of

both measurements deviate significantly from an exponential behavior and a dependence on the Xe gas density becomes obvious. The condensation of liquid Xe takes place below 200 K and the number of Xe atoms in the mixture increases significantly and therefore Xe-Xe interactions are no longer negligible and change the activation energy of solvation.

Considering the initial approximation that the chemical shift of Xe dissolved in ethanol is given by the sum of Xe-ethanol and Xe-Xe interaction contributions (Eq. 5.4-1), the chemical shift due to both must be determined separately. From Fig. 5.7(a) the dependence of the chemical shift of Xe dissolved in ethanol on Xe density can be determined for a given temperature. Then the Xe chemical shift at zero Xe density can be extrapolated (dotted line in Fig 5.11(a)) and fitted by the model function in equation 5.3-4. Now the chemical shift contribution due to Xe-ethanol interaction which defines the first virial coefficient of equation 5.5-1 can be determined resulting in the coefficients of $\alpha_1^{Xe-Eth} = 0.399 \pm 0.006$ ppm/amagat, $\alpha_2^{Xe-Eth} = 0.0058 \pm 0.0025$ ppm/amagat, and the average activation energy per Xe-ethanol pair is $E_A^{Xe-Eth} = 32 \pm 5$ meV. With these results it has been demonstrated that the analytical model is also able to describe the chemical shift contribution due to Xe-ethanol interactions.
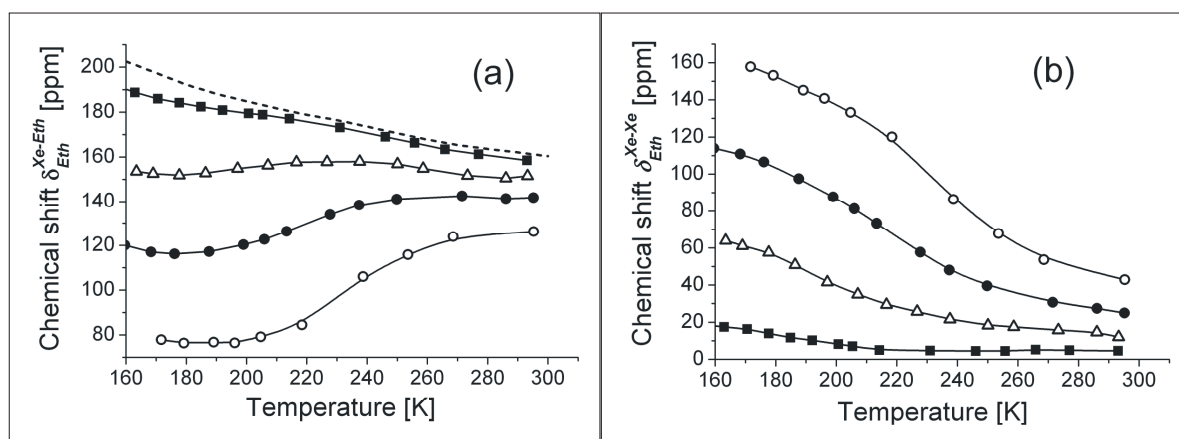
Fig. 5.11: (a) Chemical shift of Xe due to Xe-ethanol interactions versus temperature. The open (filled) circles correspond to 33 (16) amagat initial Xe gas density, the triangles (squares) to 7 (2) amagat initial Xe gas. The dashed line depicts the Xe chemical shift at zero Xe density. (b) Chemical shift of Xe caused by Xe-Xe interaction versus temperature. The symbols have the same meaning as in (a).

With these data, the chemical shift caused by the Xe–ethanol interaction can be calculated for all Xe-ethanol mixtures using equation 5.5-3 and the known temperature dependence of pure ethanol (see filled circles in Fig. 5.5(b) [Smi2]):

$$\delta_{Xe}^{Xe-Eth} = [Eth](T) \cdot \left(\alpha_1^{Xe-Eth} + \alpha_2^{Xe-Eth} \cdot \exp\left(-E_{Xe}^{Eth} / kT \right) \right). \qquad (5.5\text{-}3)$$

The results of these calculations are shown in Fig. 5.11(a). The resulting values for a Xe gas density of 2 amagat are close to the zero density limit of the Xe ethanol interaction, as it was expected. For 33 amagat initial Xe gas density a strong decrease of the values of the Xe-ethanol interaction is observed with decreasing temperature which is in agreement with the observation that at low temperatures and high initial Xe gas densities the ethanol concentration in the mixture is dropping down significantly (see Fig. 5.8(c) and Fig. 5.9(b)) and therefore also the Xe-ethanol interactions decrease. With the known chemical shifts due to the Xe-ethanol interactions the chemical shift caused by Xe-Xe interactions can be calculated from the equation

$$\delta_{Xe}^{Xe-Xe} = \delta_{Xe}^{Eth} - \delta_{Xe}^{Xe-Eth} . \qquad (5.5\text{-}4)$$

It is plotted in Fig. 5.11(b). Of course the chemical shift dependence on temperature is now reversed compared to the Xe-ethanol interactions and the chemical shift contribution due to Xe-Xe interactions is highest for 33 amagat initial Xe gas density at low temperatures. From this graph the chemical shift due to the Xe-Xe interaction can be extracted as a function of Xe density at constant temperature (Fig. 5.12). It can be concluded that the Xe-Xe interactions in ethanol lead to a chemical shift which is proportional to the Xe density in ethanol and is nearly independent of temperature.
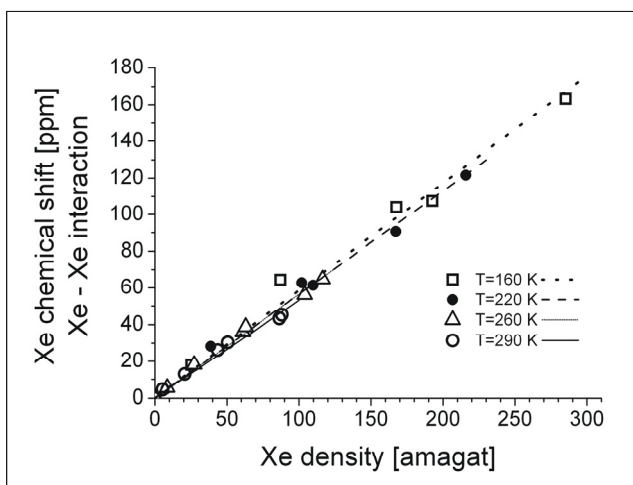

Fig. 5.12: Chemical shift of Xe due to Xe-Xe interaction versus Xe density with temperature as a parameter. The open squares correspond to 160 K, the closed circles to 220 K, the open triangles to 260 K, and the open circles to 290 K.

In Fig. 5.13(a) the plot of the chemical shift due to Xe-Xe interactions in ethanol is compared to measurements of the Xe-Xe interactions in different environments. The open circles represent again the Xe-Xe interaction of Xe dissolved in ethanol, and the solid line is a linear fit to these data. The slope of this linear fit which, in good approximation, corresponds to $-\sigma_1^{Xe-Xe}$ (the second virial coefficient in equation 5.4-1) is 0.546 ± 0.004 ppm/amagat. The dotted line in Fig. 5.13(a) is a linear extrapolation to high Xe densities of the Xe chemical shift in Xe gas at room temperature [Jam3, Jam6], the filled circles correspond to the chemical shift of liquid Xe, and the open squares are the chemical shifts of supercritical Xe gas [Bau].
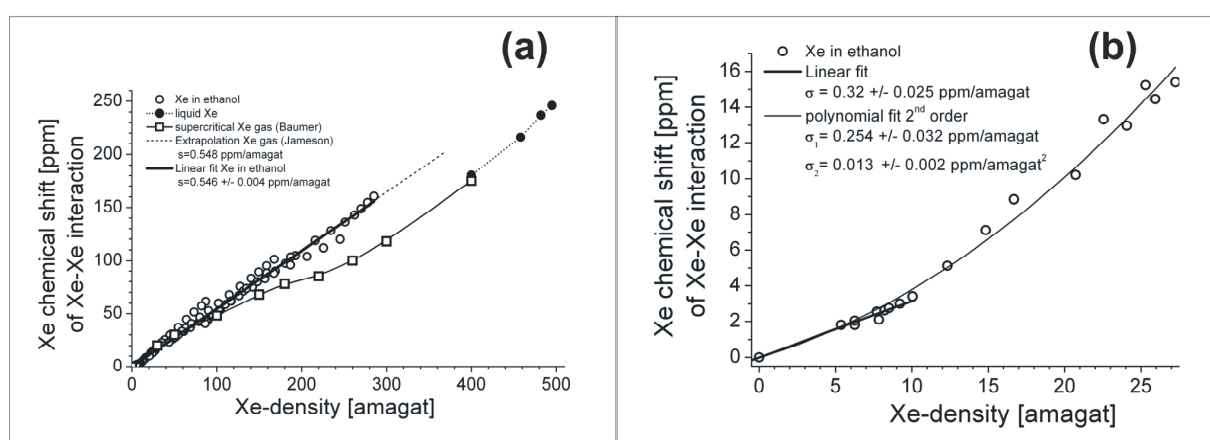

Fig. 5.13: (a) Chemical shift of Xe due to Xe-Xe interactions versus Xe density. Open circles correspond to Xe dissolved in ethanol, closed circles represent liquid Xe, and open squares are supercritical Xe gas. (b) Magnified view of the dependence of the Xe chemical shift on density caused by Xe–Xe interactions at low Xe densities.

The chemical shift due to Xe-Xe interactions in ethanol depends linearly on the Xe density and is independent of temperature. Quantitatively the shifts have the same values as the extrapolated values of Xe gas at room temperature. This means that the duration of the Xe-Xe collisions is independent of temperature. For the case of supercritical Xe the chemical shift depends nonlinearly on the Xe density and approach the chemical shifts in liquid Xe at high Xe densities. With increasing Xe density the number of collisions increases, where more than two Xe atoms are involved. In the case of liquid Xe, a single Xe atom is surrounded by more than one other Xe atom. The chemical shifts determined by collisions of several atoms are lower than in a binary collision, because the Xe atoms cannot approach each other as closely as in a binary collision.

Figure 5.13(b) shows a magnified view of the chemical shift caused by Xe-Xe-interactions in ethanol for low Xe (high ethanol) densities. For Xe densities lower than 4

amagat the Xe-Xe interaction coefficient is smaller than at higher Xe concentrations. This may be caused by a shielding effect of the surrounding ethanol molecules.

From these results the conclusion can be drawn that the approximation of equation 5.4-1 is valid, which means that the chemical shift behavior of Xe dissolved in ethanol is a sum of two contributions: the Xe-solvent interaction and the Xe-Xe interaction. Both interactions can be well described by the model developed in this work.

Xe dissolved in toluene

The chemical shift of Xe in toluene is independent of the Xe and toluene concentrations in the mixture as can be concluded from Fig. 5.7(b). Only the Xe-toluene interaction contributes to the chemical shift of Xe dissolved in toluene and therefore equation 5.5-1 simplifies to

$$\delta_{Xe}^{Tol}(T) = -\sigma_0^{Xe-Tol}(T) \cdot [Tol](T). \tag{5.5-5}$$

Therefore the chemical shift of Xe in toluene is normalized to the toluene density at room temperature. The fit of the model function to the data in Fig. 5.7(b) leads to the coefficients: $\alpha_1^{Xe-Tol} = 0$ ppm/amagat, $\alpha_2^{Xe-Tol} = 0.653 \pm 0.005$ ppm/amagat, and $E_{Xe}^{Tol} = -8.4 \pm 0.2$ meV. This means that no collective long range interactions between Xe atoms and toluene molecules exist and that the chemical shift of Xe in toluene is determined by short range interactions, which are the interactions of the Xe atoms with the π-electron system of the toluene aromatic ring preventing the Xe-atoms from other interactions.

To evaluate the possibility to use toluene as a storage medium for hyperpolarized Xe the solubility of Xe in toluene must be determined as a function of temperature. These results were obtained following the same procedure as for the Xe solubility in ethanol: the number of Xe-atoms dissolved in toluene was calculated from the chemical shift of the Xe gas line at each temperature and the volume of the total mixture at each temperature. The latter was determined by two dimensional proton MRI as can be seen from the examples in Fig. 5.8 (d)-(f). The application of equation 5.4-2 yields the Xe density $[Xe_{sol}]$ and the toluene density $[Tol]$ of the mixture as a function of temperature. The corresponding results are plotted in Fig. 5.14(a) for the measurement with an initial Xe gas pressure of 16 bar at room temperature. The open circles correspond to the Xe density of the mixture, the triangles to the toluene

density of the mixture and for comparison the density of pure toluene is depicted by the filled circles. The same behavior as for the ethanol-Xe mixture can be observed: at temperatures close to room temperature the toluene density of the mixture is highest and close to the density of pure toluene. With decreasing temperature more and more Xe atoms are dissolving into the toluene leading to an increasing Xe density and a decreasing toluene density of the mixture. At 170 K the Xe density is nearly twice of the toluene density. This experimental result makes it even more surprising that no Xe-Xe interactions in toluene were observed. The number of Xe atoms inside the mixture is higher than the number of toluene molecules for a high initial Xe gas pressure like 33 bar. Therefore not each Xe atom can be shielded from the Xe-Xe interaction by the aromatic ring of toluene. A possible explanation might be that one toluene molecule can shield two Xe atoms.
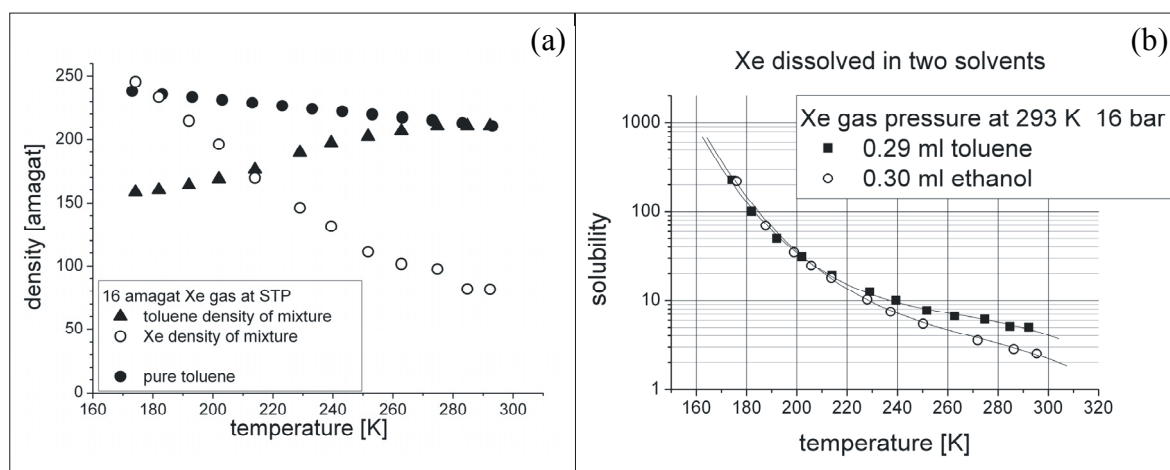

Fig. 5.14: (a) The Xe density of a Xe-toluene mixture (open circles), and toluene density of mixture (triangles) versus temperature for measurements with an initial Xe gas density of 16 amagat. The filled circles correspond to the density of pure toluene as a function of temperature. (b) Solubility of Xe in toluene (filled squares) and ethanol (open circles) for an initial Xe gas pressure of 16 amagat at room temperature as a function of temperature.

In Fig. 5.14(b) the temperature dependence of the solubility of Xe in toluene (filled squares) is compared to the solubility of Xe in ethanol (open circles) for the same initial gas pressure of 16 bar. At temperatures above the boiling point of Xe more Xe dissolves in toluene than in ethanol whereas at temperatures below the boiling point of Xe the solubility becomes the same. This observation can be explained by the fact that in the cold dense mixtures of both solvents with Xe the number of Xe atoms inside the mixtures becomes comparable to the number of solvent molecules. Therefore the dissolution of Xe at low temperature is also influenced by the dissolution of Xe in itself which is the same for both solvents.

5.6   Conclusions and outlook

The coefficients of Xe – atom (molecule) interaction for different environments normalized to the density of the interaction partners are summarized in Tab. 5.1. An overview of the chemical shifts normalized to the density as a function of temperature for different environments is given in Fig. 5.15, where the curves are calculated using the model function (equation 5.3-4) together with the parameters from Tab. 5.1. The chemical shift depends linearly on the density of the interaction partner in all cases.

Table 5.1: Coefficients of long (α_1) and short (α_2) range interactions for the Xe chemical shift in different environments

Interaction	α_1 [ppm/amagat]	α_2 [ppm/amagat]	E_A [meV]
Xe –Xe gas	0.415 ± 0.01	0.0097 ± 0.0025	-66 ± 4
Xe – Xe liquid	0.412 ± 0.04	0.026 ± 0.02	-17.2 ± 8
Xe – Xe in ethanol	0.543 ± 0.004	~ 0	-
Xe - ethanol	0.399 ± 0.006	0.0058 ± 0.0025	$- 32.2 \pm 5$
Xe – toluene chemical shift is independent from Xe and toluene density			
Xe – toluene	~ 0	$\alpha_2 = 0.653 \pm 0.005*)$	-8.35 ± 0.2

*) normalized to toluene density at room temperature

   A very strong dependence on temperature is observed for the Xe-Xe interactions in the Xe gas phase (solid line). This is due to the fact that the mean duration of the collisions between two atoms strongly depends on the kinetic energy of the atoms. A smaller kinetic energy leads to a longer duration of the collisions and therefore to a higher chemical shift. In the case of liquid Xe (dashed line) both the long range and the short range interactions are smaller than in the gas phase because the Xe atom is approached by more than one other Xe atom which inhibits the nearest possible approach of two atoms. Hence the interaction of two atoms given by the coefficients is weaker than in the gas phase. The smaller temperature dependence results from the fact that now the duration of collisions is nearly independent of temperature because it is dominated by the number of collisions per time interval which in

liquids should be nearly independent of temperature. The weak temperature dependence is caused by a decreasing mean distance between the Xe atoms with decreasing temperature.
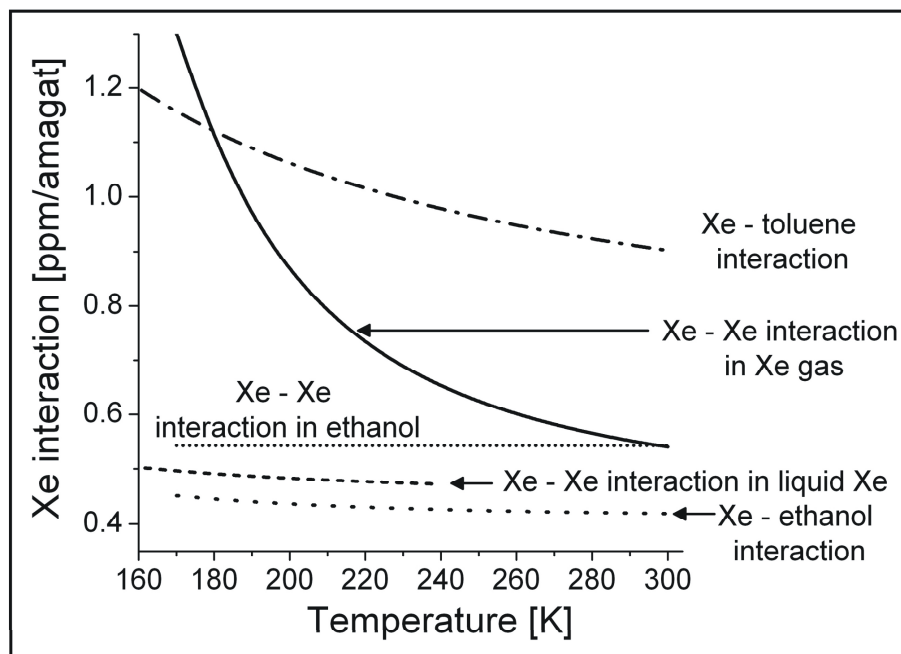

Fig. 5.15: Fitted Xe chemical shift normalized to density for different environments versus temperature. Solid line: Xe–Xe interaction in Xe gas; dashed line: Xe–Xe interaction in liquid Xe; short dotted line: Xe–Xe interaction in ethanol; dotted line: Xe–ethanol interaction in ethanol; and dashed dotted line: Xe–toluene interaction in toluene.

Xenon dissolved in ethanol (short dotted line) shows (see Fig. 5.13(a)) a behavior like a diluted gas without a temperature dependence of the Xe-Xe interaction coefficients up to high Xe densities (~ 250 amagat). At 293 K the Xe-Xe interaction coefficient in the liquid phase has the same value as for the Xe-Xe interaction in the gas phase. In ethanol the Xe atoms are diluted by the ethanol molecules, so that almost exclusively binary collisions of the Xe atoms can occur.

The Xe-ethanol interaction (dotted line) in ethanol shows a similar behavior to the Xe-Xe interaction in liquid Xe. The coefficient for the interaction of Xe with ethanol is about 10% smaller than the one for the Xe-Xe interaction in liquid Xe due to a smaller binding energy between Xe and ethanol compared to the binding energy between Xe atoms.

Finally, the coefficient for the Xe-toluene interaction (dotted dashed line) shows a strong dependence on temperature. This is because that in the case of Xe dissolved in toluene the total chemical shift is determined by the temperature dependent short range interactions since the Xe atoms are captured in the aromatic rings of the toluene molecules. The dependence on temperature is caused by decreasing distances between the Xe atoms and the toluene ring at decreasing temperature of the mixture.

Based on the work of Buckingham and Jameson [Buc, Jam7] a simplified model was developed, which quantitatively describes the dependence of the Xe chemical shift on temperature and density of the interacting atoms or molecules by only three fit parameters. With known gas temperature, the Xe density in the gas phase can be determined from the Xe gas chemical shift. In more complex situations (e. g. Xe dissolved in solvents) the chemical shift can be divided into a part which depends on the interaction between the solvent molecules and the Xe atoms and one part which describes the Xe-Xe interaction in the solvent. Both contributions can be described by the model. Based on the results of this work it should be possible to describe the dependence of the Xe chemical shift on temperature and density with a simple analytical equation for several solvents. If the chemical shift is independent of the Xe concentration (e. g. in toluene) the measurement of the chemical shift using hyperpolarized Xe may be used to determine non-invasively the local temperature for example in the human body.

6 On-line monitoring of polymerization reactions

In this chapter an example will be given that demonstrates the potential of [129]Xe NMR to serve as an ultra-sensitive and non-invasive probe to detect minimal physical, and chemical changes in a sample. The chemical shift sensitivity combined with the large non-equilibrium magnetization of hyperpolarized Xe which allows for time-resolved measurements will be used to follow polymerization reactions in real-time. For that purpose, a continuous flow of hyperpolarized Xe gas was applied to different reaction bulks dissolving fast into the lipophilic monomer solutions. The conversion of monomer into polymer results in a chemical shift change of the dissolved Xe resonance, and the progress of the reaction can be observed. This study deals with spectroscopically and temporarily resolved Xe NMR and it will be shown that from these spectroscopic data as a function of time the reaction rate of the investigated polymerizations can be calculated.

6.1   Introduction

A very important task in polymer engineering is the evaluation of the basic principles of polymerization reactions like the influence of temperature and pressure or other process parameters on the rate and yield of the reaction. The production of polymers with well defined physical and chemical properties is also required for most applications thereby demanding a narrow distribution of molecular weights. Therefore, it would be desirable to follow a polymerization in real-time instead of analyzing the composition of the polymer or the degree of polymerization afterwards, e. g. by gel permeation chromatography (GPC, a form of size exclusion chromatography), end group analysis by titration, or by ^{1}H and ^{13}C NMR.

In order to be used for the on-line monitoring of reactions analytical tools are required which circumvent the time consuming sample extraction, thereby eliminating the time lag between taking samples and calculating process parameters. Two examples of analytical methods which fulfill these requirements are calorimetry and IR (infrared) vibrational spectroscopy. Both have special advantages and disadvantages. The calorimetric measurements have the major advantage of being capable to investigate every kind of not thermoneutral reactions, including those that are difficult to analyze by other analytical tools (like for example suspension polymerizations or other reactions that take place in

heterogeneous phases) [Gio]. Calorimetry infers global reaction evolution by tracking the heat produced or consumed in a reactor due to reaction, but does not give any information about the composition of the products [McK, Zea, Vie]. On the other hand IR (infrared) vibrational spectroscopy can give information of the product composition but its application is limited to samples that can be penetrated by radiation with particular wave lengths which is the main drawback of most optical methods (exception: Attenuated Total Reflectance (ATR) IR spectroscopy). However the real-time plot of the IR spectroscopic measurements shows the qualitative and quantitative changes in the chemical structures based on the analyzed characteristic bands of e. g. disappearing monomers as well as of growing polymer chains [Sah] and is nowadays not only applied in research laboratories but also industries make use of it in order to control critical parameters of chemical reactions [Mor].

Other analytical tools like ^{1}H or ^{13}C-NMR spectroscopy are also able to provide a temporal resolution in the order of seconds (not true for natural abundance ^{13}C) but are usually limited to samples with well separated NMR lines which is not in most cases fulfilled for polymerization reactions because of the small differences in the chemical structure of monomers and polymers. Here it will be shown that [129]Xe NMR can overcome this problem by reporting quantitatively the composition of the monomer/polymer mixture by its chemical shift.

In recent years, [129]Xe NMR spectroscopy was proposed as a technique to investigate the amorphous phase of solid polymers, and it could be shown that its NMR parameters (like chemical shift, line width, T_1 and T_2) are sensitive to the composition of this phase [Man], which cannot be characterized by X-ray measurements. Stengle and Williamson demonstrated that in a closely related group of solvents, such as n-alkanes with different chain lengths, the chemical shift of the Xe resonance varies linearly with the solvent density and can be extrapolated to the chemical shift of Xe in LDPE (low-density polyethylene). However the chemical shift differences decrease with increasing chain length and two polymers with different chain length but the same chemical composition can hardly be discriminated [Ste]. Kentgens et al. measured the line width of the Xe signal of Xe absorbed in LDPE, LLDPE and HDPE (low-density polyethylene, linear low-density polyethylene, high-density polyethylene) as a function of the magnetic field strength and found out that the line width increases linearly with the field for all samples indicating that the line width of the Xe resonance in an amorphous polymer originates from a distribution of chemical shifts within the sample and that there is no exchange of Xe between the different regions on the time scale

of the inverse line width [Ken]. Kennedy showed that it is possible to detect structural changes in polymers, that are due to cross-linking, derivatization or degradation with ^{129}Xe NMR spectroscopy [Ken2]. ^{129}Xe NMR is also viable to monitor structural changes of polymers that originate from differences in temperature, because especially the line width of the absorbed Xe signal is sensitive to the changing mobility of Xenon atoms in polymers above or below the glass transition temperature [Ste, Che5, Mil2]. In systems with more than one phase, such as copolymers or polymer blends, the different domains can be distinguished by the chemical shift of absorbed Xe if the exchange of Xe between the domains is slow compared to the NMR experiment [Bro, Wal2]. Here the domain size and the Xe self diffusion coefficient in the investigated polymer is important, because domain sizes of 1 μm or below result in a fast exchange of the Xe atoms between different domains yielding only one Xe line (diffusion coefficients of Xe in polymers are in the range between $2*10^{-13}$ and $4*10^{-11}$ m^{2}s^{-1}) [Jun, Jun2, Sim].

In this work it will be shown that ^{129}Xe NMR is not only viable to investigate the amorphous phase of polymer products but also to monitor different polymerizations in real-time if a continuous flow of hyperpolarized Xe can be provided. For that purpose the living cationic polymerization of tetrahydrofuran (THF) and the free radical polymerization of styrene were selected and the different monomer/initiator mixtures were fumigated inside the NMR spectrometer with hyperpolarized Xe gas. The reactions were performed as mass polymerizations using the monomer also as a solvent, because the additional shift contribution of a solvent to the Xe chemical shift complicates the data analysis and was therefore avoided.

6.2   Experimental

For the living cationic polymerization a well defined amount (ranging from 0.6 to 2.4 ml) of absolute THF was mixed with a well defined amount (3.6 – 15.2 μl) of the initiator CF$_3$SO$_3$CH$_3$ (trifluormethanesulfonic acid methylester) in the sample tube for experiments with hyperpolarized Xe shown in Fig. 4.3. The sample preparation was done in a protective gas atmosphere (N$_2$) to prevent the reaction of the initiator with oxygen or water from the air. After adding the initiator the sample tube was delivered very fast into the magnet and a continuous flow of hyperpolarized Xe gas was applied, that was produced using the continuous flow mode of the Rb-Xe hyperpolarizer which is described in chapter 3.4. The hyperpolarized Xe gas was delivered through a 7 m long PFA (perfluoroalcoxy) pipe directly

into the sample tube positioned inside the spectrometer. The used spectrometer (4.7 Tesla, Xe resonance frequency: 55.3 MHz) is described in chapter 4 and is equipped with a standard temperature controlling system. The polymerizations were carried out at 40 to 60° C to make them reasonably fast. The resonator (20 mm birdcage coil) was already warmed up to this temperature when the sample tube was inserted. The acquisition of Xe NMR spectra was started immediately after the insertion of the sample tube and the thermal equilibration of the sample could be followed by the Xe chemical shift. This was proven before in a separate experiment where pure THF was heated up from room temperature to 40°C and the process was followed by the acquisition of hyperpolarized ^{129}Xe NMR spectra. The warming-up of the monomer leads to a decrease of the chemical shift (164.3 ppm at 293 K to 160.8 ppm at 313 K) whereas the progress of the polymerization reaction result in an increasing chemical shift of the absorbed Xe as will be shown later. For the analysis of the polymerization the first spectra were therefore neglected. For analysis those spectra were used, where the chemical shift started to increase to ensure that the sample was in thermal equilibrium.

The same procedure was followed for the free radical polymerization of styrene. Prior to polymerization, commercially added inhibitor was removed from the styrene by chromatography. The used initiator for the radical polymerization of styrene was AIBN ($C_8H_{12}N_4$, 2,2'-azobisisobutyronitrile), which was added just before insertion of the sample tube into the NMR magnet.

## 6.3   Results I: living cationic polymerization of THF

The living cationic polymerization of THF initiated by $CF_3SO_3CH_3$ is a chain-growth polymerization which consists of the three basic reaction steps: initiation, propagation, and termination. The reaction mechanism is presented below. The initiation reaction consists of two steps: first one monomer molecule reacts with one initiator molecule forming the active cationic species of this reaction, which is an oxonium ion. In the second step the next monomer reacts with the oxonium ion by insertion thereby keeping the cationic function. This reaction is slower compared to the first one and determines therefore the kinetics of the initiation reaction. During the propagation reaction the subsequent monomers are added to the active species leading to a growing polymer chain.

1. Initiation:
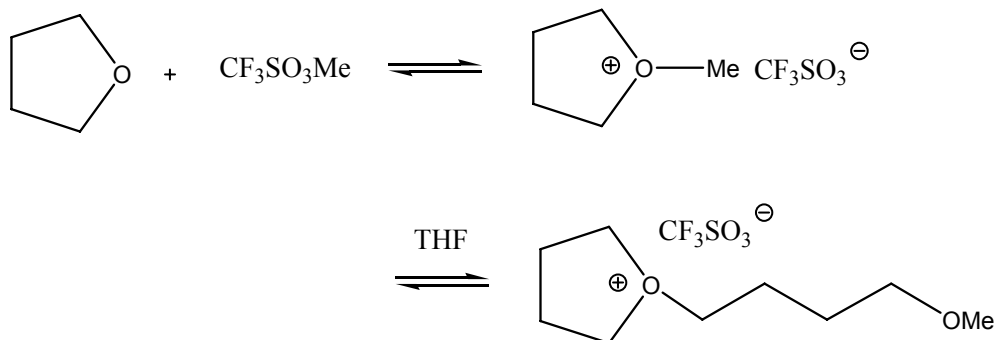
2. Propagation:
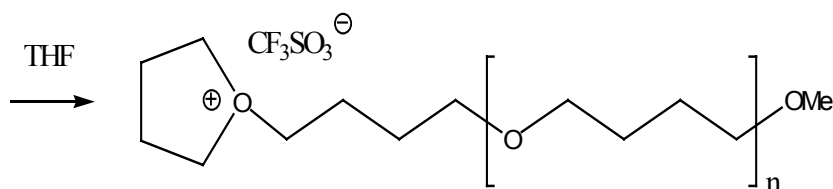
A special feature of living polymerizations is that no termination reaction takes place unless a molecule suitable for termination is added to the reaction bulk (for the cationic reaction presented here it could be for example water). If the initiation reaction is fast compared to the propagation reaction (in general true for living polymerizations), all polymer chains are initiated at the same time and grow until almost all monomer molecules are consumed resulting in a narrow distribution of molecular weights of the product. The kinetics of a living polymerization is mainly determined by the propagation reaction which in this case follows a first order rate law, because the concentration of the active species remains constant:

$$v_P = \frac{-d[M]}{dt} = k_P [P^*][M], \qquad (6.3\text{-}1)$$

where v_P is the velocity of the reaction, k_P the reaction constant, $[P^*]$ the concentration of the active species (oxonium ions), and $[M]$ the concentration of the monomer. The concentration of the active species $[P^*]$ is the same as the concentration of the initiator $[I]$ for living polymerizations and remains constant during the whole reaction process. Therefore the

degree of polymerization P_n is linearly dependent on the conversion U of the reaction and can be calculated using a simple formula [Cow]:

$$P_n = \frac{[M]}{[I]} \cdot U \,.$$

(6.3-2)

Some selected ^{129}Xe NMR spectra acquired during the living polymerization of 1 ml THF (12.3 mmol) initiated by 3.8 µl CF$_3$SO$_3$CH$_3$ (0.033 mmol) at 40 °C are shown in Fig. 6.1. The plot only depicts the spectral region of the hyperpolarized Xe dissolved in the reaction bulk omitting the signal of Xe gas, which has the same chemical shift during the whole polymerization process due to the continuous flow of hyperpolarized Xe gas. The gas line was used as a reference for the spectra and due to the low density of the hyperpolarized gas (0.07 bar) was set to zero ppm. Figure 6.1 depicts only a few selected NMR spectra of the whole series that was acquired during the polymerization process in order to recognize the increasing chemical shift and the broadening of the line of dissolved Xe accompanied by different line shapes occurring during the polymerization process.
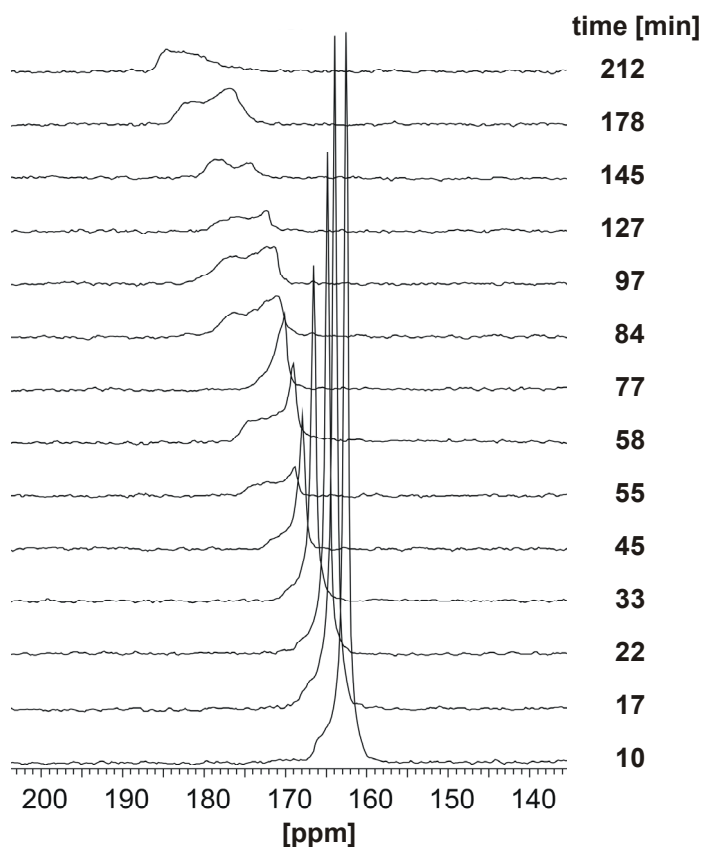
Fig. 6.1: ^{129}Xe NMR spectra of the polymerization of 1 ml THF with 3.8 µl CF$_3$SO$_3$CH$_3$ as a function of time. The plot shows the line of hyperpolarized Xe dissolved in the reaction bulk of some selected spectra to have a better view to the different line shapes occurring during the polymerization process.

Fig. 6.2: Dependence of chemical shift (center of gravity) on time for the polymerization of 1 ml THF with 3.8 µl CF$_3$SO$_3$CH$_3$.

The huge broadening of the Xe line representing Xe dissolved in the reaction bulk cannot be explained by the increasing viscosity of the reaction bulk, wh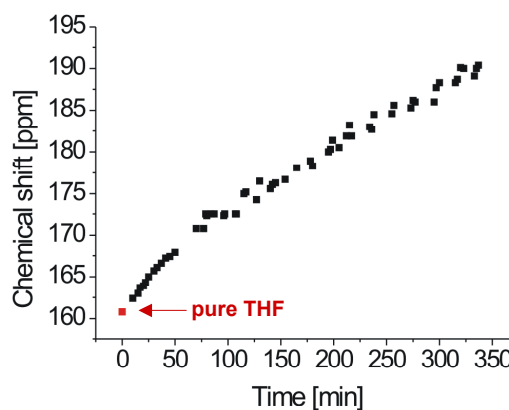ich takes place during the mass polymerization due to the consumption of the monomer. Kentgens et al. found for Xe absorbed in solid polymers a line width of the Xe resonance of 100 Hz in different polyethylene samples, that were measured above the glass transition temperature. For polymers below the glass transition temperature (e. g. polycarbonate at room temperature) the measured line width was 500 Hz [Ken]. These measurements indicate that the line width of the absorbed Xe signal is sensitive to the chain mobility. However, they cannot explain the observed line broadening (up to 700 Hz) accompanied by different asymmetric line shapes during the polymerization process, because the melting point of polytetrahydrofuran (PTHF) is between 20-40°C depending on the chain length and its glass transition temperature is –86 °C, respectively [Mat]. The PTHF chains are therefore very mobile during the polymerization carried out at 40 °C and additional monomer molecules increase the mobility of the chains significantly compared to the solid polymer. Kentgens suggested, based on measurements of the line width as a function of the magnetic field strength, that the line broadening of Xe absorbed in polymer samples is due to a distribution of chemical shifts or a small residual shielding anisotropy [Ken]. This could also be true for Xe dissolved in the reaction bulk during the polymerization, but cannot be verified from the data presented here although the line widths and asymmetric shapes were reproduced during other real-time measurements of this polymerization. For this reason the center of gravity of the Xe line was chosen for further evaluation of the chemical shift data.

Figure 6.2 represents the plot of the center of gravity of the Xe line dissolved in the reaction mixture versus time for the whole polymerization process. From this plot it becomes obvious that the chemical shift of Xe dissolved in the reaction bulk increases continuously during the reaction. The change of the chemical shift can be explained by the changing composition of the reaction bulk during the polymerization: in the beginning of the reaction, the bulk consists mainly of the monomer THF and therefore the chemical shift of the dissolved Xe is dominated by this component. During the reaction the amount of monomer decreases while the polymer chains are growing. Now the chemical shift of the dissolved Xe is influenced by a sum of two contributions which are changing while the reaction is proceeding: one contribution due to the decreasing amount of monomer and the other contribution due to growing polymer chains. From Fig. 6.2 it can be determined that the chemical shift depends non-linearly on time. This can be explained by the fact that the

velocity of the reaction (see equation 6.3-1) depends on the monomer concentration, which is decreasing during the reaction leading to a deceleration of the reaction at high conversion.

Now the chemical shift behavior of Xe during the polymerization will be discussed in more detail. According to chapter 1 (see equation 5.4-1) the chemical shift of Xe dissolved in a monomer/polymer mixture can be written as:

$$\delta_{Xe}^{diss} = -\sigma_0^{Xe-mon}(T) \cdot [mon](T) - \sigma_0^{Xe-pol}(T) \cdot [pol](T) - \sigma_1^{Xe-Xe}(T) \cdot [Xe](T), \qquad (6.3-3)$$

where δ_{Xe}^{diss} is the chemical shift of Xe dissolved in the reaction bulk, $\sigma_0^{Xe-mon}(T)$ and $\sigma_0^{Xe-pol}(T)$ determine the shielding contribution due to Xe-monomer and Xe-polymer interaction depending on temperature T, $[mon](T)$ and $[pol](T)$ depict the monomer and polymer density in the reaction mixture and σ_1^{Xe-Xe} is the shielding due to Xe-Xe interactions, which is proportional to the Xe density $[Xe](T)$. Equation 6.3-3 can be reduced to $\delta_{Xe}^{diss} = -\sigma_0^{Xe-mon} \cdot [mon] - \sigma_0^{Xe-pol} \cdot [pol]$ due to the experimental conditions used here: first, all experiments were performed at constant temperature, therefore the temperature dependence of all parameters can be neglected. Second, the chemical shift contribution due to Xe-Xe interactions can be omitted due to the very low Xe density in experiments with hyperpolarized Xe performed in the continuous flow mode of the hyperpolarizer (0.07 bar Xe in the gas phase). The two remaining parameters ($-\sigma_0^{Xe-mon} \cdot [mon]$ and $-\sigma_0^{Xe-pol} \cdot [pol]$) are changing differently during the progression of the polymerization; for the first term σ_0^{Xe-mon} remains constant because the shielding depends only on the chemical nature of the monomer molecule, but $[mon]$ is decreasing due to the consumption of the monomer whereas the second term $[pol]$ is increasing by the same amount, because it is considered as the number of monomer molecules that are incorporated in the polymer chains. Moreover, σ_0^{Xe-pol} might change because the chemical nature of the polymer chains changes during the polymerization because of increasing chain length.

In order to analyze the chemical shift data of a polymerization reaction in a quantitative way both contributions to the chemical shift must be determined independently. For this reason THF-polymers with different chain lengths were produced in the chemical lab following the same procedure as described in the experimental part and termination by

addition of water. After precipitation, washing, and drying of the polymers they were analyzed by GPC and ^{129}Xe NMR and their specifications are given in Tab. 6.1. The molecular weights which are determined by GPC are not very accurate because the used GPC chromatograph is not calibrated for THF polymers. Nevertheless, the obtained numbers show the right trend (increasing molecular weight for increasing reaction time or higher temperature). The values given for the polydispersity are more reliable because for their determination no calibration is needed.

Table 6.1: Specifications of different THF polymers

Polymer	Monomer/ initiator ratio	Reaction temperature [°C]	Reaction time [min]	Reaction yield in %	Molecular weight (GPC) [kg/mol]	Polydisper- sity (GPC)	Xe chemical shift [ppm]
1	212.6	40	30	40	6.1	1.8	200.8
2	212.6	40	64	53	8.0	1.96	201.7
3	224.2	40	114	77	29	2.07	201.7
4	145.5	50	36	67	14	1.91	201.3

It can be seen that all polymer products have high polydispersities which is unusual for living polymerizations. This can be explained by the fact that the reactions were performed as mass polymerization (without solvent) leading to a high polydispersity for conversions exceeding 20% because of the increased viscosity of the system [Mue, Eli]. The data presented here show the same behavior, because the polymer with the lowest conversion (polymer 1) possesses the smallest distribution of molecular weights.

For the acquisition of the ^{129}Xe NMR spectra each solid polymer was filled in the NMR pressure tube and fumigated with 4 bar thermally polarized Xenon. 0.2 bar of oxygen were added in order to shorten the T_1 relaxation time. After an equilibration time (at least 2 hours) the ^{129}Xe NMR spectra of the polymer samples were measured at room temperature. The result of the measurements is shown in Fig. 6.3(a).

It becomes obvious that the Xe chemical shift only very slightly depends on the polymer chain length which is in agreement with the measurements of Stengle et al. [Ste] for Xe absorbed in polyethylene with different molecular weights. The mean value for the

chemical shift of Xe in solid PTHF (poly-tetrahydrofurane) is 201.4 ppm. A possible explanation for this behavior might be that the Xe atom can probe only a part of the polymer chain. Once the polymer chain is exceeding a certain length the chemical shift of absorbed Xe remains constant.
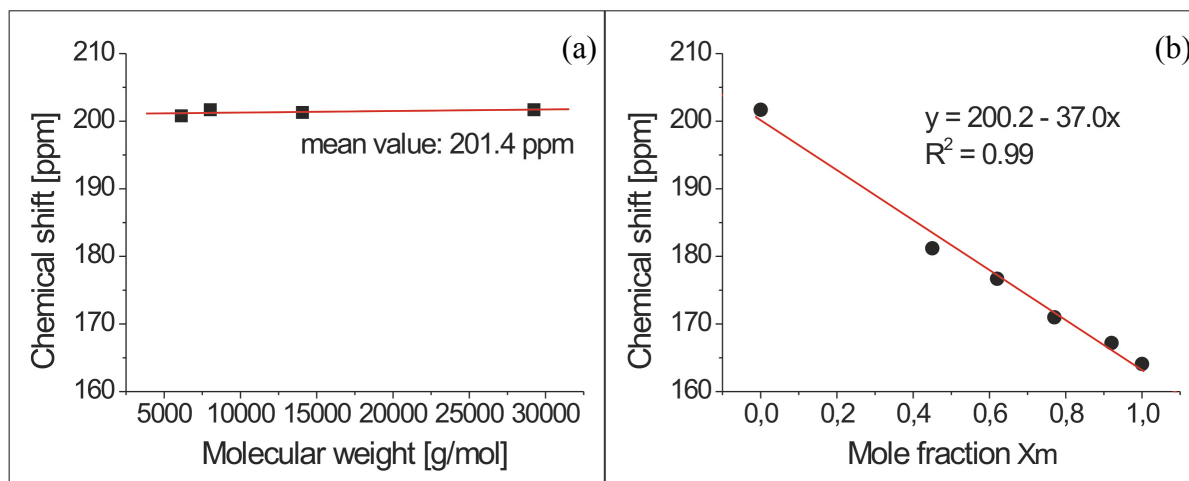

Fig. 6.3: Calibration measurements with thermally polarized Xe to evaluate the influence of (a) chain length and (b) monomer concentration on Xe chemical shift.

Another important result of the measurements with thermally polarized Xe is that the line width of Xe dissolved in solid PTHF was narrow for all investigated polymers (100-150 Hz in agreement with [Ken]) compared to the very broad lines shown in Fig. 6.1 for the on-line measurement (up to 700 Hz) proving that the line broadening cannot arise from a decreasing mobility of the Xe atoms during the polymerization.

From Fig. 6.3(a) it can be concluded that the Xe chemical shift change during the polymerization reaction must arise only from the decreasing monomer concentration in the reaction bulk. This was proven and quantified by measurements of solid PTHF (polymer 3) dissolved in different amounts of monomer. The mixtures were also fumigated with 4 bar thermally polarized Xe and 0.2 bar oxygen and the measured Xe chemical shift values are plotted in Fig. 6.3(b) versus the mole fraction X_m of the monomer (Mole fraction: ratio of the moles of one component and the total moles of the mixture. In a binary mixture the mole fractions of both components have the following relationship: $1 = X_m + X_p$). Also for these measurements a small Xe line width (50 Hz) for Xe dissolved in the mixture was observed. A linear dependence of the Xe chemical shift on the mole fraction of the mixture can be determined. This is a very important result, because now the Xe chemical shift can be used to determine quantitatively the composition of the reaction bulk during a polymerization

reaction. From the time-resolved chemical shift data it is therefore possible to calculate the monomer concentration of the mixture at each time of the reaction, from which the conversion and finally the degree of polymerization of the polymer can be computed.

In Fig. 6.4(a) the results of the time-resolved measurements with hyperpolarized Xe are shown for different polymerization reactions. The black squares correspond to the data of the polymerization already shown in Fig. 6.2, the blue symbols represent a polymerization using 2.4 ml THF (29.6 mmol) and 15.2 µl initiator (0.132 mmol) at 40 °C and the green squares show the data of the polymerization of 0.77 ml THF (9.6 mmol) initiated by 7.6 µl $CF_3SO_3CH_3$ (0.066 mmol) at 50 °C. Because the Xe chemical shift depends on temperature (see chapter 5) the chemical shift data of the polymerization performed at 50 °C were corrected to fit into the plot of the polymerizations carried out at 40 °C. The correction was done according to preliminary measurements of hyperpolarized Xe dissolved in pure THF heated up from room temperature to 40 °C. The chemical shift of Xe dissolved in pure THF at 40°C is indicated by the red square and was used as the zero time reference point for the polymerization reactions.
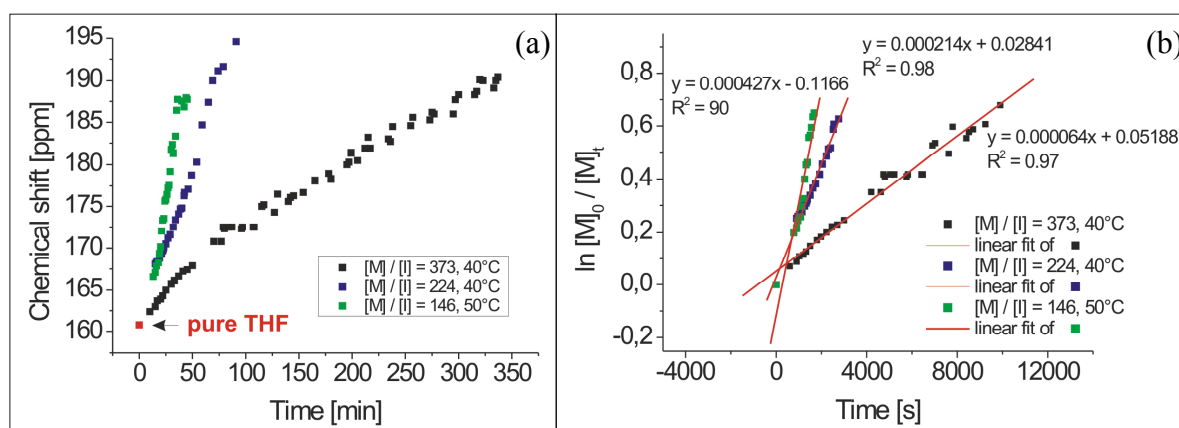

Fig. 6.4: (a) chemical shift data (center of gravity) of dissolved Xe for two polymerizations performed at 40° C (black and blue squares) and for a polymerization at 50° C (green squares). (b) ln $[M]_0/[M]_t$ calculated from the chemical shift data to determine the reaction constants for the polymerizations. Only values up to a conversion of 50% were taken into account, see text for details.

Because the increasing chemical shift can be directly correlated with a decreasing monomer concentration (Fig. 6.3 (b)) different velocities of the reactions can be recognized according to the different starting conditions. The influence of the concentrations of the reactants on the reaction speed can be considered by comparing the two polymerizations

carried out at 40 °C. For the polymerization represented by the black squares the concentration of monomer and of initiator was smaller compared to the reaction symbolized by the blue points, which results in a smaller velocity of the reaction (see equation 6.3-1) as can been seen by the smaller slope of the chemical shift data.

The influence of temperature on the velocity of the reaction becomes obvious from Fig. 6.4(a) as well. The polymerizations symbolized by the black and green squares have comparable reactant concentrations but were performed at different temperatures (black squares: 40 °C, green squares: 50 °C). The chemical shift data of the polymerization at 50 °C show a much steeper slope indicating a much higher velocity of the reaction which is in agreement with basic chemical theory.

For the calculation of the reaction constant equation 6.3-1 must be integrated leading to the following result:

$$\ln\left(\frac{[M]_0}{[M]_t}\right) = k_p \cdot [P^*] \cdot t, \tag{6.3-4}$$

where $[M]_0$ and $[M]_t$ are the monomer concentrations at the beginning of the reaction and at a certain time t. If the polymerization follows first order kinetics and shows a living behavior - which means that $[P^*]$ is constant since no termination reactions take place - the plot of $\ln([M]_0/[M]_t)$ versus time shows a linear dependence. The slope of this line is given by $k_p \cdot [P^*]$ and from this k_p can be calculated since the concentration of the active species is identical to the initial initiator concentration.

In order to compute the reaction constant from the on-line ^{129}Xe NMR measurements, $[M]_t$ must be calculated from the chemical shift data. This can be done by first converting the chemical shift data into the mole fraction of the monomer Xm using the known relationship between the Xe chemical shift and the mole fraction as depicted in Fig. 6.3(b). The data of the calibration measurement must first be corrected for the temperature difference (the calibration measurement was performed at room temperature), which can be done by using the known temperature dependence of the Xe chemical shift, which was evaluated in a preliminary experiment of hyperpolarized Xe dissolved in pure THF. Afterwards $[M]_t$ can be simply calculated by multiplying the time-resolved mole fraction data by the initial monomer concentration for each polymerization reaction. Now $\ln([M]_0/[M]_t)$ can be calculated and the

result is plotted for each polymerization reaction versus time in Fig. 6.4(b). Only the data points up to a conversion of 50% are used for each polymerization, because at high conversions the reactions do not follow a first order law anymore due to the increasing viscosity of the system. The data show a nice linear dependence on time, and the results of the fits are shown Fig. 6.4(b). The value of the reference point was taken into account for the fits to mark the beginning of the reaction because of the delay due to the waiting for thermal equilibrium after putting the sample inside the spectrometer. From the slope of the fits the reaction constant can be computed by division by the initiator concentration. The results are summarized in Tab. 6.2.

Table 6.2: Reaction constants of the polymerizations monitored by real-time ^{129}Xe NMR

Polymerization	Monomer/initiator ratio	Reaction temperature [°C]	Reaction constant [s mol]
1 (■)	373	40	0.0019
2 (■)	224	40	0.0016
3 (■)	146	50	0.0065

It becomes obvious that the reaction constants of the polymerizations performed at 40° C are fairly similar as is expected by the theory, because the reaction constants depend on temperature and on the experimental conditions, which were the same for both polymerizations. The reaction constant for the polymerization carried out at 50° C is nearly four times higher than the ones for the 40° C reactions with is in nice agreement with the empiric rule of van't Hoff, which predicts for a temperature increase of 10° C a two to four times higher reaction constant [Roe]. These results prove the capability of hyperpolarized ^{129}Xe NMR as an analytical tool for the on-line monitoring of reactions.
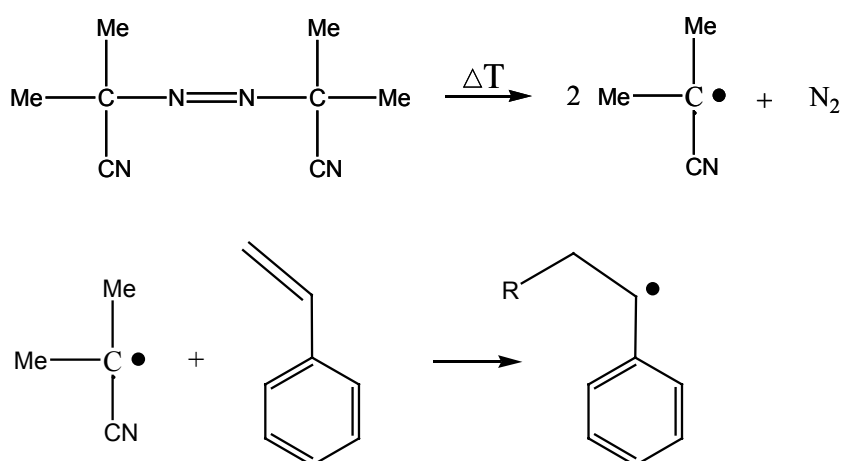
6.4   Results II: free radical polymerization of styrene

Free radical polymerizations have the most industrial applications of all polymerization methods and are therefore of high technological interest. Hence, this study also tries to follow a free radical polymerization with hyperpolarized ^{129}Xe NMR. This is also very interesting for further applications of hyperpolarized Xe because radicals could react as relaxation agents

thereby destroying the Xenon polarization. Therefore, this part of the work is also meant to find out if hyperpolarized ^{129}Xe NMR can be successfully applied to radical systems.

The free radical polymerization of styrene follows a chain-growth mechanism consisting of the same basic reaction steps as the living cationic polymerization of THF discussed before. In opposition to the living polymerization termination reactions take place and therefore must be considered for the kinetic evaluation. The initiator for this polymerization is AIBN ($C_8H_{12}N_4$, 2,2'-azobisisobutyronitrile) which at a temperature of 40° C splits in two radicals as is indicated in the first step of the reaction mechanism denoted below. In the second step of the initiation reaction the radicals react with one monomer thereby keeping the radical function. This step is fast compared to the decomposition of AIBN and has therefore nearly no influence on the velocity of the initiation reaction. During the propagation reaction, which follows a first order rate law, monomer molecules are reacting with the active species forming growing polymer chains. In the termination reaction the radical ends of two macromolecules can react with each other or with radicals formed during the initiation reaction under recombination or disproportionation thereby eliminating the radical function. Because the growing polymer chains are randomly terminated and the two termination reactions lead to very different chain length, the products of free radical polymerizations possess a large polydispersity.
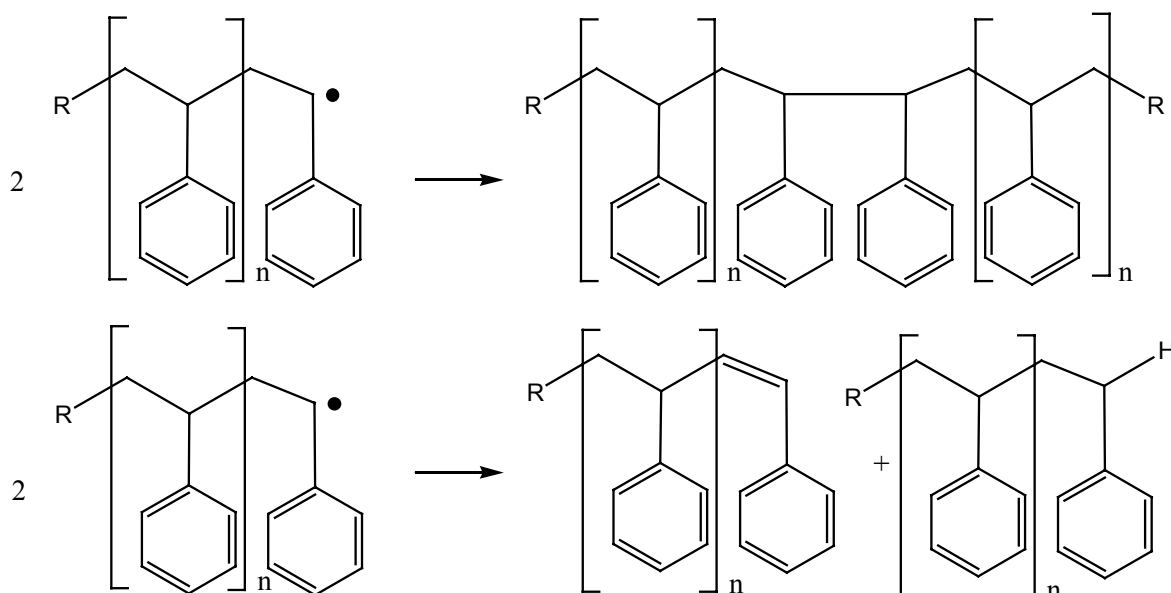
1. Initiation

2. Propagation
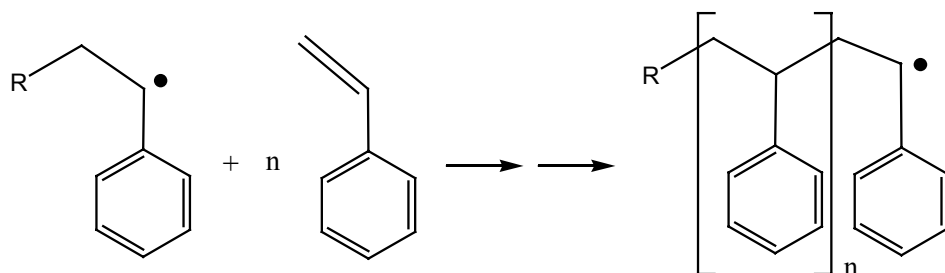
3. Termination

The real-time monitoring of the free radical polymerization of styrene was performed following the same procedure as described for the polymerization of THF. To 0.6 ml of styrene (5.2 mmol) 66 mg of AIBN (0.4 mmol) were added just prior to the insertion of the sample inside the NMR magnet. A continuous flow of hyperpolarized Xe gas was applied to the reaction bulk and the acquisition of the ^{129}Xe NMR spectra was started after reaching thermal equilibrium. The spectra show a good signal to noise ratio of the dissolved Xe comparable to the one of the cationic polymerization of THF indicating that the free radicals do not destroy the Xe polarization on a short time scale. The chemical shift of Xe dissolved in the reaction bulk is shown in Fig. 6.5 as a function of time.

Three drastic changes in chemical shift can be distinguished in the plot, the first arising from an increase of temperature and the second due to the starting of the reaction. The temperature chosen initially for this reaction was 40° C which is indicated in the figure by the yellow color. It becomes obvious that at 40° C the reaction was very slow which is represented by a constant chemical shift of Xe dissolved in the reaction bulk. Only after 40 minutes a small increase in the chemical shift can be observed. The small velocity of the reaction could be due to a small amount of active species inside the reaction mixture, because at 40° C the decomposition of AIBN is slow.
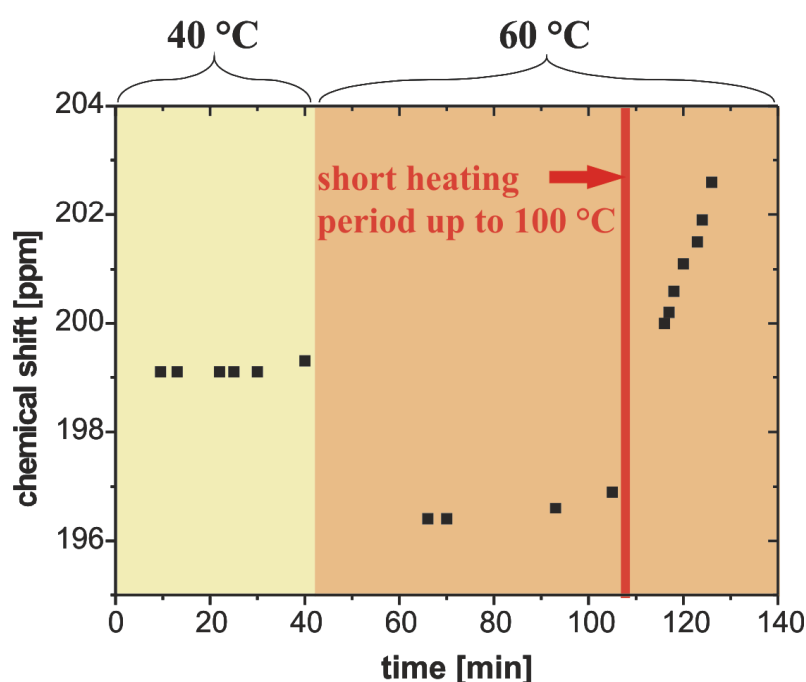

Fig. 6.5: Chemical shift of Xe dissolved in the reaction bulk versus time for the free radical polymerization of styrene initiated by AIBN. The colors in the plot indicate different temperatures.

To speed up the reaction the temperature was increased to 60° C (indicated in the figure by the orange color) and after a waiting period to ensure thermal equilibrium the acquisition of ^{129}Xe NMR spectra was continued. A significant decrease of the Xe chemical shift can be observed which arises from the temperature change. It can be determined that the reaction progresses only slightly faster at 60° C compared to 40° C. To accelerate the decomposition of the AIBN and therefore the formation of free radicals the reaction mixture was taken out of the spectrometer and heated with a heat gun for a short time period up to approximately 100° C (represented by the red line in Fig. 6.5). After re-insertion into the spectrometer and a delay for thermal equilibrium (the temperature inside the spectrometer was kept at 60° C) the measured ^{129}Xe NMR spectra show a fast increasing chemical shift of the

Xe dissolved in the reaction bulk representing a high speed of the polymerization reaction. The line width for the dissolved Xe was narrow (30 Hz) for all spectra that were acquired before the heating period but started to increase continuously to a value of over 200 Hz (at 130 minutes) after the heating. The line shape was symmetric for all observed spectra, but the degree of conversion was still low when the experiment was stopped. Therefore it cannot be excluded that during this polymerization also asymmetric line shapes occur.

This experiment presents the proof of principle that ^{129}Xe NMR is also viable to monitor reactions even including free radicals. Three different velocities of the polymerization could be distinguished by the slope of the chemical shift data. This study does not yet give quantitative results, because the necessary calibration of the Xe chemical shift to the mole fraction of styrene in the monomer/polymer mixture is missing. However, after calibration measurements the calculation of the reaction constant should be possible for the quasi-stationary period of the reactions (for conversions between 1 and 10% the radical concentration in the reaction bulk can be considered constant due to equal velocities of the initiation and termination reactions [Cow]).

6.5   Conclusions and outlook

This study reports the first application of hyperpolarized ^{129}Xe NMR spectroscopy to analyze polymerization processes in real-time which is a challenge in polymer engineering. It has been successfully demonstrated that the chemical shift of Xe dissolved in the reaction bulk monitors quantitatively the mole fraction of the monomer allowing the calculation of the conversion at each time of the reaction and the reaction constant. The line broadening and asymmetric line shapes of the dissolved Xe occurring during the polymerization may contain additional information of the physical environment of the Xe atoms in the reaction bulk like e.g. chain entanglements that restrict the mobility of the Xe atoms. This aspect of the experiments needs to be explored carefully in the future perhaps leading to additional information of the behavior of macromolecules in solution. The capability of the application of hyperpolarized ^{129}Xe NMR not only to the living cationic polymerization of THF but also to the free radical polymerization of styrene suggests an exciting potential for the monitoring of various kinds of reactions.

7 Time resolved chemical shift imaging

In this chapter a dynamic process is investigated which is not isotropic, therefore also spatial resolution is required in combination with temporal and spectroscopic resolution. This is realized by using chemical shift imaging (CSI) with one dimensional spatial resolution in the direction of the anisotropy of the observed process. One dimensional CSI is about as fast as two-dimensional imaging without spectroscopic information because in both cases only one dimension is encoded using the time consuming phase encoding method. Both methods (2D FLASH imaging and 1D CSI) have been used to visualize the melting and dissolution process of Xe ice into pure ethanol and a 80/20 vol% ethanol-water mixture [Han]. This study was performed in order to evaluate the feasibility to dissolve high quantities of hyperpolarized Xe in a liquid which has the potential to be used for biological applications. Therefore the hyperpolarized Xe was produced in the batch mode of the hyperpolarizer and accumulated on top of the frozen liquids in order to achieve higher Xe quantities than can be obtained in the continuous flow mode of the hyperpolarizer.

7.1 Introduction

Hyperpolarized ^{129}Xe MRI has great potential to reveal dynamic processes because there is no need for signal averaging due to the large non-equilibrium magnetization that can be obtained by optical pumping. Applied as a gas it has been used to demonstrate void space imaging in materials [Son4, Gre], imaging of the respiratory system of living animals [Moe, Joh2, Che3, Via, Cre], and even human beings [Den, Che4, Mac, Ebe, Bac, Mug, Saa, Lan].

It has been proposed that the difference in chemical shift of Xe in different types of tissue [Sak, Wol] or in oxygenated and deoxygenated blood [Wol2, Bif, Alb2] can provide contrast enhancement for several physiological applications like functional MRI [Alb3]. This has lead to the first applications of *in vivo* Xe chemical shift imaging following the respiration of hyperpolarized Xe by laboratory rats [Swa, Swa2], where the brain and the thorax of the rats has been imaged.

As mentioned in chapter 1 it is an important issue to find a suitable storage medium for large quantities of hyperpolarized Xe. Another major task for hyperpolarized ^{129}Xe NMR is the quick and efficient delivery of ^{129}Xe to the sample during the polarization lifetime of

[129]Xe. This is especially difficult for one of the most promising applications of hyperpolarized Xe which is the investigation of biological materials like cells and proteins exploiting the extremly sensitive chemical shift range of [129]Xe. In recent applications Xenon was proven to be a useful probe for protein structure, surface, and morphology, and protein ligand binding events [Til, Rub2]. Furthermore there are other promising methods for investigating proteins like the use of SPINOE for highlighting hydrophobic cavities in proteins [Son5, Lan] or to utilize functionalized Xe as a biosensor [Spe, Han2].

The natural solvent for cells and proteins is water in which Xe dissolves only in small quantities (Ostwald coefficient for Xe in water is 0,1 [Pie]) due to its hydrophobic character. For the efficient delivery of hyperpolarized Xe to aqueous solutions the use of the amphoteric solvent ethanol is promising because it can be mixed with water in arbitrary proportions and it is a very good solvent for Xe as has been shown in chapter 5. Therefore the dynamics of melting, migration and dissolution of hyperpolarized Xe ice into ethanol and ethanol/water mixtures was investigated with the method of time resolved two dimensional MRI and one dimensional CSI starting from the initial condition of a Xe ice layer on top of the frozen solvent.

7.2   Experimental

The hyperpolarized Xe was produced using the batch mode of the Rb-Xe hyperpolarizer which is described in chapter 3.3. Under the experimental conditions used here the polarizer produces about 1.5 cm^3/min (@1 bar, 20°C) Xe gas with a polarization fraction of 20%. The hyperpolarized Xe gas flows through the sample cell with an inner diameter of 7 mm, which was introduced in chapter 4, containing about 0.2 cm^3 of either ethanol or an ethanol/water (80 vol% ethanol) mixture. The different solvents were first deoxygenated in three pump and thaw cycles and then frozen at 77 K in liquid nitrogen. A layer of hyperpolarized Xe ice with a thickness of about 1 mm was accumulated over a time period of 6 min onto the surface of the frozen solvent. In order to maintain the Xe polarization in the sample tube, a field of 1000 G was applied using a permanent Halbach magnet. After the preparation period the sample tube was closed with two valves, separated from the hyperpolarizer and finally inserted into a 4.7 T vertical bore Bruker imaging system operating at a Xe resonance frequency of 55.3 MHz. The same birdcage resonator with an inner diameter of 20 mm (BRUKER) was used for all NMR experiments.

A series of two-dimensional FLASH images and one-dimensional chemical shift images were acquired during the heating-up and melting processes of the hyperpolarized Xe ice layer to observe the occurring phase transitions and the dissolution process. The corresponding pulse sequences for FLASH and CSI images are shown in Fig. 7.1(a) and (b).
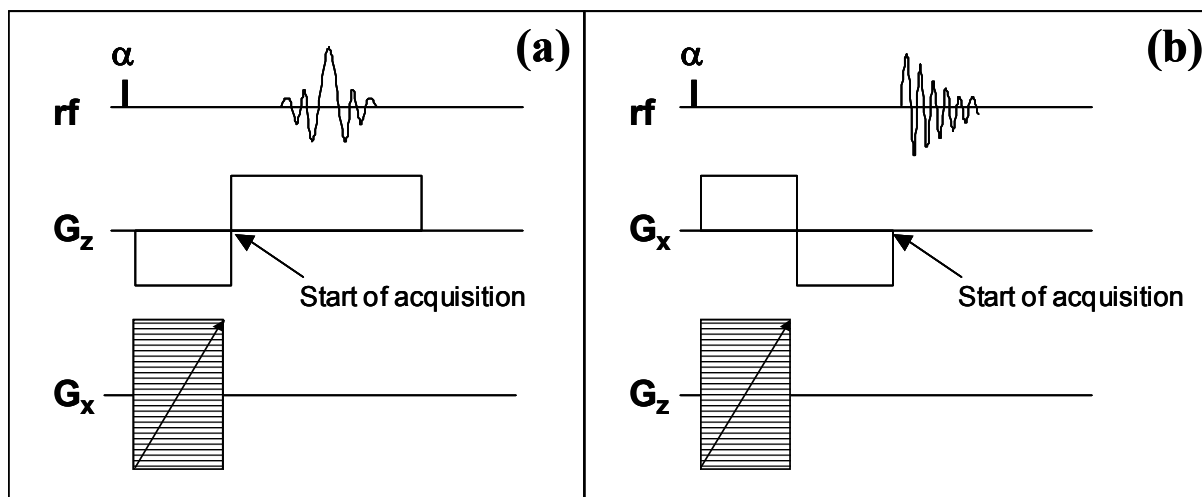

Fig. 7.1: a) Pulse sequence of two-dimensional FLASH imaging and b) one-dimensional spatially resolved Xe CSI imaging.

The 2D FLASH images were obtained using 64 phase encoding G_x gradient steps along the indirect dimension and by acquiring the gradient echo signal along the direct dimension caused by bipolar G_z gradients. The field of view (FOV) for each 2D FLASH image is 20 mm for both directions and the images represent a projection along the direction of the *y*-axis within the sensitive coil volume since no slice selection was applied. The spatial resolution is about 80 μm in the *x* direction and 310 μm in the *z* direction and the experimental time for the acquisition of one image was about 1.5 s.

The sequence to obtain one dimensional CSI images consists also of an rf-excitation pulse with a small flip angle α followed by a gradient pulse in z direction of 150 μs duration for phase encoding. The bipolar gradient pulse G_x in the *x*-direction serves to generate a gradient echo. After switching off the G_x gradient and a minimum delay time to ensure that the actual gradient strength has decreased to zero, the second half of the echo was acquired (acquisition time: 20 ms). For spatial encoding the gradient G_z was increased stepwise from – 1 T/m to +1 T/m in 64 steps. This results, for the chosen field of view of 30 mm, in a spatial resolution of 470 μm. The total time required for a complete 1D image was 2 s.

The observed melting and dissolution process of Xe ice takes place on a time scale of several minutes. Therefore it was possible to acquire several FLASH and CSI images during its progress. In order to compensate for the losses of Xe magnetization due to consumption by rf-pulses and T_1-relaxation, and to obtain a comparable signal-to-noise ratio for all images, the flip angle α was adequately increased from $\alpha = 0.25°$ for the first image to $\alpha = 12°$ for the last image of both sequences.

To obtain a temperature reference for the heating-up process the temperature was measured in separate experiments with a calibrated PT 100 temperature sensor for both solvents. In these measurements the solvent was frozen in liquid nitrogen without Xe ice on top and the temperature was measured at three different positions in the sample: at the meniscus, in the middle of the solvent cylinder and at the bottom of the sample tube. Figure 7.2 depicts the initial condition of the Xe MRI experiments (frozen solvent with hyperpolarized Xe ice on the top) and the geometry of the sample tube (sample tube and inner glass tube where also Xe ice is formed during the accumulation process), also indicated are the different positions of the temperature sensor for the separate temperature measurements.
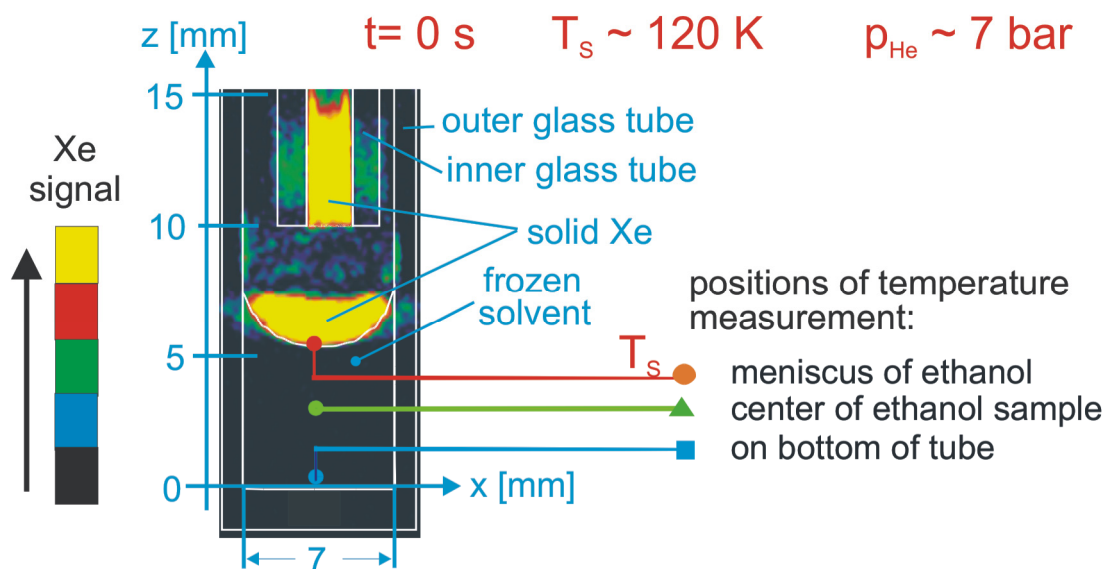

Fig. 7.2: Two dimensional x-z FLASH image of hyperpolarized Xe ice frozen on the surface of an ethanol/water ice block depicting the initial conditions of the experiments. The image was taken 60 s after the removal from the liquid nitrogen bath and the temperature was determined by the line width of the Xe ice signal in the corresponding CSI image [Yen]. The positions of the PT 100 temperature sensor for the separate temperature measurements in the solvents are indicated.

The temperature evolution inside the liquids is independent of the composition of the solvents (pure ethanol and 80/20 vol% ethanol/water mixture) and is mainly determined by the heat capacity of the glass tube due to the small amount of solvent sample. The results of the temperature measurements at the different positions are given in Fig. 7.3, where also the time schedule for the imaging experiments is denoted. The first images were taken 60 s after the removal from the liquid nitrogen bath and will be referred to as 0 s in the following, because they represent the beginning of the imaging series.
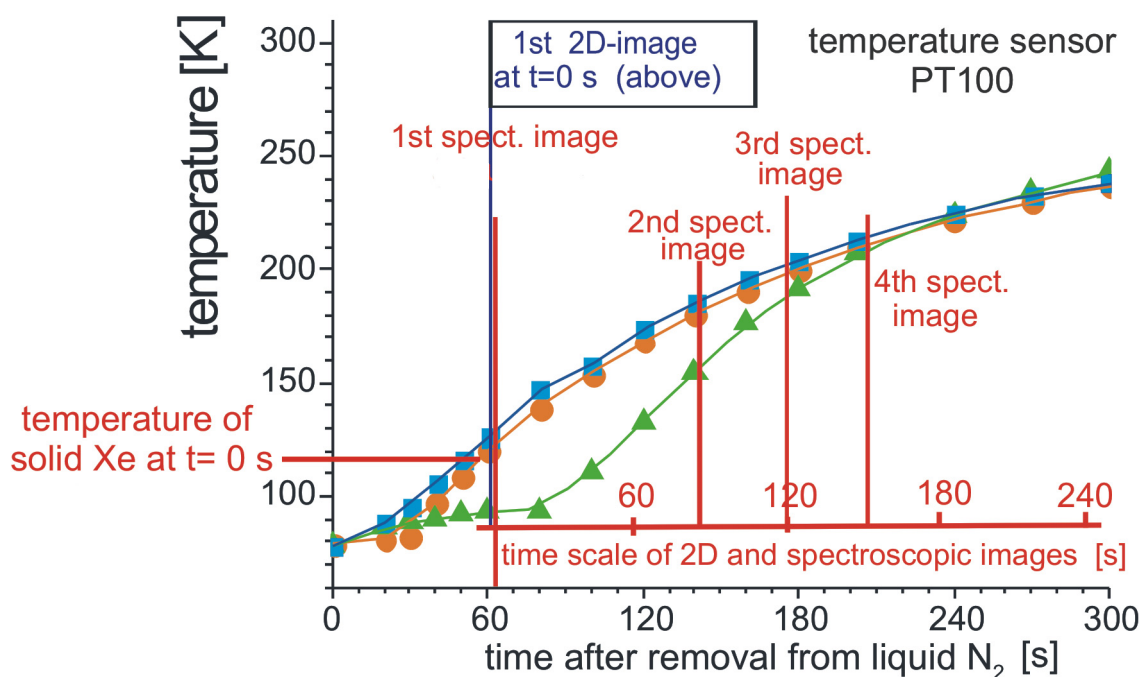

Fig. 7.3: Results of temperature measurements versus time. The symbols correspond to the different positions in the solvent which are indicated in Fig. 7.2 (red circles: meniscus, green triangle: center of the solvent cylinder, blue squares: bottom of sample tube). The time schedule for the imaging experiments is denoted as well.

A maximum temperature gradient in the sample of 45 K between the center and the bottom of the solvent cylinder can be observed 80 s after the removal from liquid nitrogen. After 200 s the temperature deviations in the whole sample are smaller than 5 K. These measurements serve as an estimation of the temperature during the heating-up process and will be used for the interpretation in the result part.

7.3 Results I: two dimensional FLASH images

The incorporation process of solid hyperpolarized Xe ice into ethanol and an 80/20 vol% ethanol/water mixture is studied in order to evaluate if high amounts of hyperpolarized Xe can efficiently be delivered to the solvent in this way. Therefore a series of two dimensional FLASH images were acquired for each solvent which are shown in Fig. 7.4. The top part of Fig. 7.4 corresponds to the measurements of pure ethanol whereas the bottom part depicts the images of the 80/20 vol% ethanol/water mixture.
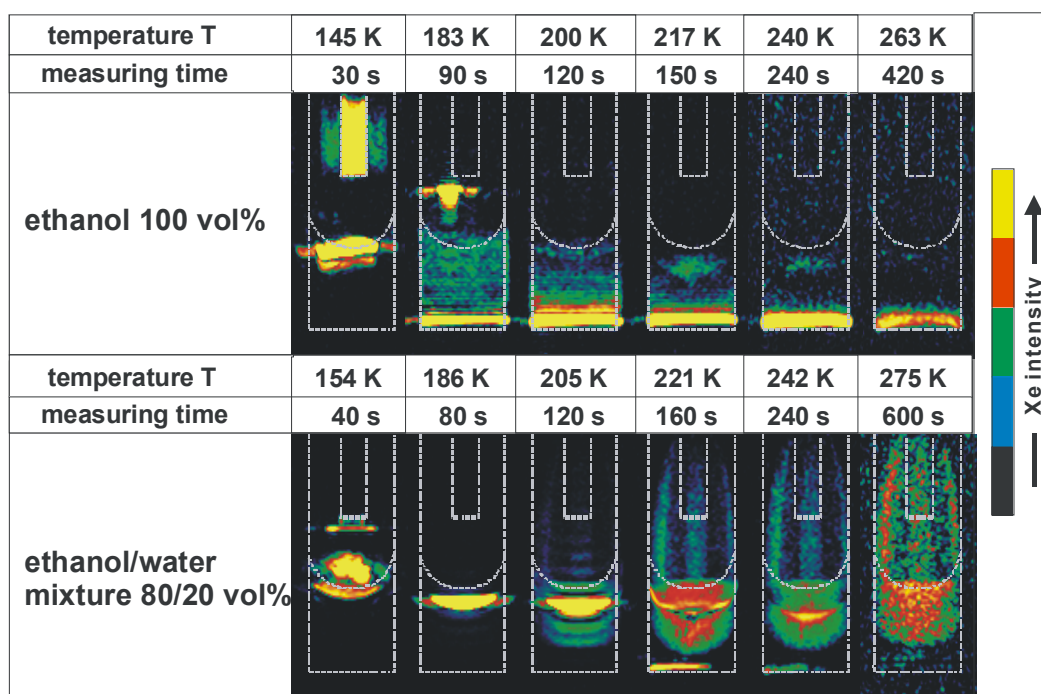

temperature T	145 K	183 K	200 K	217 K	240 K	263 K	
measuring time	30 s	90 s	120 s	150 s	240 s	420 s	
ethanol 100 vol%							
temperature T	154 K	186 K	205 K	221 K	242 K	275 K	
measuring time	40 s	80 s	120 s	160 s	240 s	600 s	
ethanol/water mixture 80/20 vol%							

Fig. 7.4: Series of two dimensional FLASH images of hyperpolarized Xe ice, which is melting, migrating and dissolving into the supercooled ethanol (top) or the solid ethanol/water mixture (bottom). The dotted lines indicate the position of the inner glass tube for hyperpolarized Xe delivery, the sample tube, and the shape of the meniscus of the investigated solvents. For pure ethanol all the Xe polarization is concentrated on the bottom of the sample tube after 120 s and remains there until the end of the measurements whereas for the case of the ethanol/water (80/20 vol%) mixture nearly all Xe polarization is in the gas phase after 600 s.

The temperature T_s which was determined at the meniscus of the frozen solvent in the separate temperature measurements is denoted for each image. The first picture of the series of images of hyperpolarized Xe ice incorporating into pure ethanol (top part of Fig. 7.4) was taken after 30 s at a temperature of 145 K and shows that the solid Xe (melting point 161.3 K, compare Fig. 2.2) starts to sink slowly as a whole block through the ethanol although the

melting point of pure ethanol, T_m^{eth} = 159 K, is much higher. This can be explained by the phase diagram of ethanol, which shows a supercooled liquid state at temperatures between 97 K < T < 159 K [Egu] in the case of fast cooling like it was preformed in these experiments. At t = 90 s (T_s ~ 183 K) the solid Xe of the inner tube has melted and forms a liquid droplet at the end of the inner tube. This is consistent with the fact that solid Xe melts at T_m = 161.3 K and liquid Xe starts to boil at T_b = 208 K at 7 bar and is a confirmation for the validity of the temperature measurements. In this image also a thin layer of hyperpolarized Xe with a thickness of about 1mm on the bottom of the tube can be observed, which has sunk down through the supercooled solvent due to its higher density compared to ethanol. However, the FLASH images do not provide any information about the physical state and the composition of this thin layer, which can consist of pure liquid Xe or a dense Xe/ethanol mixture. This is a good example for the requirement of spectroscopic information and gives the motivation for the CSI measurements which will be discussed in the next section. In the next image at t = 120 s and T_s = 200 K the liquid Xe droplet of the inner glass tube has fallen through the liquid ethanol and is joining the Xe layer on the bottom. This layer with a high density of Xe atoms still exists at times t > 420 s (see following images of this series) and hardly any polarized Xe gas is observable above the solvent although the actual temperature inside the ethanol (217 K, 240 K, 263 K) is much higher than the boiling point of Xe (208 K).

The huge chemical shift differences of the Xe phases (solid Xe ~ 300 ppm, liquid ~ 250 ppm and gas = 0 ppm) result in a distortion of the images in the direction of frequency encoding. The dotted lines which indicate the meniscus and inner and outer glass tubes were determined by the images of solid Xe (image in Fig. 7.2 and Fig. 7.4 top at t = 30 s and bottom at 40 s). Because the direction of the read encoding was chosen to be the *z* direction, the images of liquid Xe are displaced by about 0.8 mm and the ones of the Xe gas phase by about 5 mm along the negative *z*-direction relative to the image of the solid induced due to their chemical shift differences. An example for this behavior can be recognized in the top part of Fig. 7.4 for the image acquired at t = 90 s. Here the droplet of liquid Xe is positioned about 1 mm below the end of the inner tube and the image of the gas phase is shifted almost entirely into the liquid ethanol phase. The sideways displacement of the liquid droplet to the left side of the outer surface of the inner glass tube is a real effect due to a small tilting of the inlet, and the surface tension of the liquid Xe. The overlap of coexisting Xe phases complicates a qualitative and quantitative evaluation of the dissolution process of

hyperpolarized Xe by means of FLASH imaging and shows again the need of spectroscopic information which can be provided by CSI.

The images on the bottom in Fig. 7.4 correspond to the incorporation process of hyperpolarized Xe ice into a solid ethanol/water matrix. In the first image of this series at t = 40 s and T_s = 154 K a layer of Xe ice can be seen on top of the frozen solvent. The next two images taken at 80 and 120 s and temperatures of 186 and 205 K, respectively, show a layer of liquid Xe on top of the frozen solvent as is indicated by the small displacement of this layer of about 1 mm below the meniscus of the solvent resulting from the chemical shift difference of liquid and solid Xe. The liquid Xe cannot pass through the solvent at these temperatures as was observed for pure ethanol because due to the addition of water the ethanol is not in a supercooled state (which means viscous but liquid) but forms a solid matrix with the water molecules which the liquid Xe is not able to penetrate. The addition of water to ethanol leads to an increase of the melting point of the solid ethanol/water to 210 K which is close to the boiling point of liquid Xe at 7 bar. The next image at t = 160 s (T_s = 221 K) shows consequently that a large fraction of liquid Xe has evaporated into the gas phase before it could be dissolved into the ethanol/water mixture. The gas image clearly shows the meniscus and the inner tube (indicated by two dark vertical stripes) shifted by Δz = -5 mm. In addition to the Xe gas two thin layers of liquid or dissolved Xe are visible on the surface and close to the bottom of the ethanol/water volume. This observation can be explained by the fact that some liquid Xe migrates through pores and/or cracks, which have formed in the solid ethanol/water block which will be proven by the CSI images. At t = 600 s nearly all the remaining Xe polarization is in the gas phase, which already indicates that pure ethanol is a better storage medium for hyperpolarized Xe than an ethanol/water mixture.

7.4 Results II: one dimensional CSI

Figure 7.5 (a)-(f) represents a selection of six one dimensional spectroscopic images of the incorporation process of hyperpolarized Xe in pure ethanol showing all different coexisting Xe phases resolved in the spectral, spatial, and time dimensions. The horizontal axis in the plots of Fig. 7.5 represents the spectroscopic dimension of the Xe chemical shift ranging from 0 to 350 ppm. The vertical axis corresponds to the amplitude of the spectra and the third axis gives the z position, where z = 0 mm is the bottom of the sample tube and z = 6.5 mm depicts the lowest point of the ethanol meniscus. Figure 7.5 (a) is the CSI image which corresponds to

the 2D image at t = 0 s presented in Fig. 7.2 and shows the pure Xe ice with a chemical shift of 300 ppm positioned at z = 6.5-9 mm on top of the frozen ethanol and attached to the inner glass tube at z = 10-17 mm. The amplitudes of the spectra in Fig. 7.5(a) indicate that most of the solid Xe is located on top of the meniscus (6 – 9 mm) which is reasonable because the one dimensional CSI images represent projections in x and y directions and the diameter of the inner tube is much smaller compared to that of the sample tube. The line width of the Xe ice varies from 14 ppm (~ 800 Hz full width at half maximum (FWHM)) at z ~ 6.5 mm to less than 1 ppm (~50 Hz FWHM) at z = 15 mm. This can be explained by differences in the temperature of the solid Xe at different positions in the sample tube. The Xe ice which is in direct contact with the frozen solvent remains cold for a longer time than the one attached to the inner tube, because the frozen solvent acts as a thermal reservoir. The smaller line width of Xe ice in the inner tube at higher temperatures arises from an increased mobility of the Xe atoms that averages out the broadening from the dipole-dipole interaction.

Following Yen and Norberg [Yen], who measured the line width of Xe ice as a function of temperature, the temperature of solid Xe in Fig. 7.5(a) is estimated from its line width to be T ~ 135 K at z = 15 mm and T ~ 117 K at z = 6 mm. This agrees well with the temperature T_s of 120 K measured with a temperature sensor near the meniscus at this time. The next image in Fig. 7.5(b) (t = 90 s, T_s = 183 K) shows that the Xe ice at the inner glass tube has melted and is now liquid (indicated by the narrow peak at 255 ppm at a z position of about 10 mm) which has been already observed in the FLASH images in Fig. 7.4. It can also be seen that a thin layer of hyperpolarized Xe has been formed on the bottom of the sample tube. The spectra in the vicinity of z = 1 mm show two peaks at 300 ppm and 250 ppm demonstrating that at t = 90 s the thin layer at the bottom of the sample tube is composed of solid Xe particles in coexistence with liquid Xe. The next image acquired at 120 s with a temperature of 200 K (Fig. 7.5(c)) shows that the Xe ice at the bottom of the sample tube has converted into liquid Xe, because the Xe ice peak has vanished from the spectra. The decreased chemical shift of 235 ppm of this thin layer indicates that ethanol molecules start to diffuse into the liquid Xe layer. In the next CSI images (Fig. 7.5(d)-(f)) the chemical shift of this layer drifts from 235 ppm at t = 120 s to 195 ppm at t = 690 s. According to the results of chapter 5 it can be concluded that the temperature increases and the averaged Xe density within this layer decreases with time which can be easily explained by the diffusion of ethanol molecules into this layer driven by the concentration gradient.
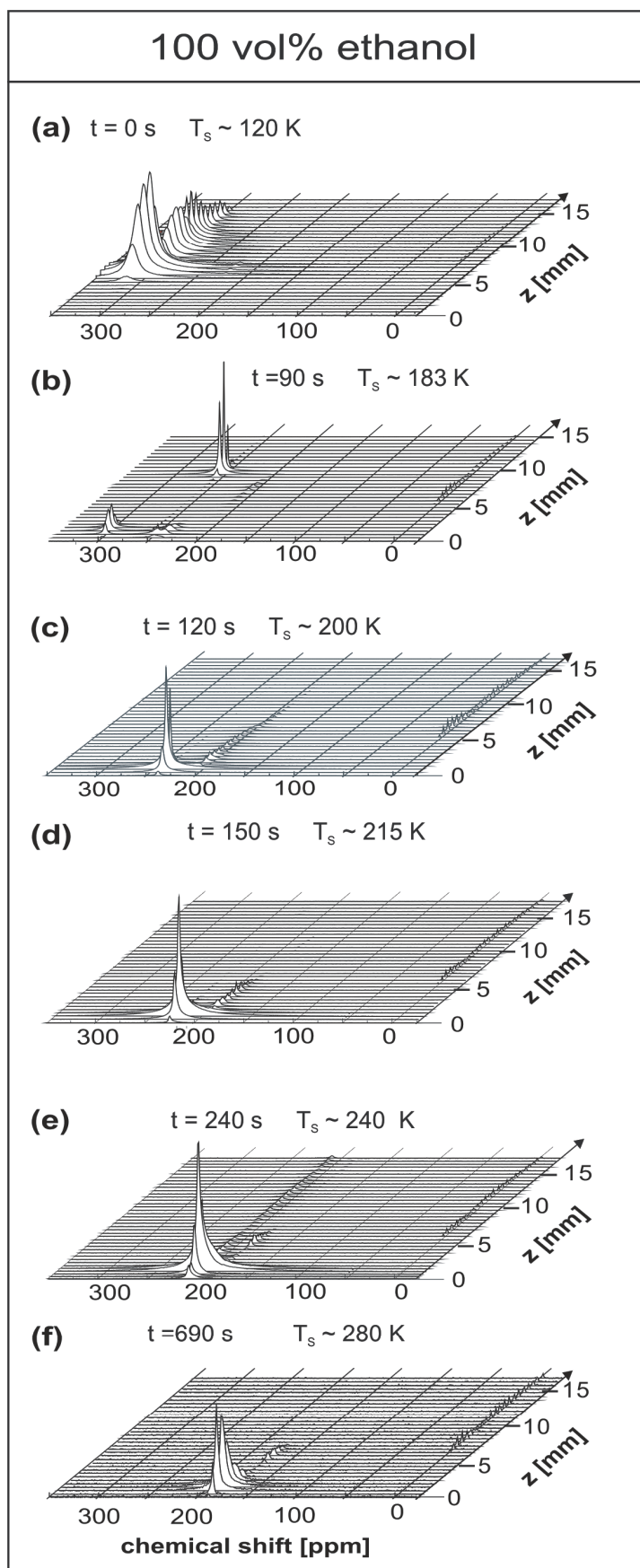
100 vol% ethanol

(a) t = 0 s T_s ~ 120 K

(b)   t = 90 s T_s ~ 183 K

(c)   t = 120 s T_s ~ 200 K

(d)   t = 150 s T_s ~ 215 K

(e)   t = 240 s T_s ~ 240 K

(f)   t = 690 s T_s ~ 280 K

chemical shift [ppm]

Fig. 7.5(a)-(f): One-dimensional CSI images of hyperpolarized Xe frozen on ethanol as a function of time. The horizontal axis in the plots represents the spectroscopic dimension of the Xe chemical shift ranging from 0 to 350 ppm. The vertical axis corresponds to the amplitude of the spectrum and the third axis gives the z position, where z = 0 mm is the bottom of the sample tube and z = 6.5 mm depicts the lowest point of the ethanol meniscus. The corresponding time and temperature of the images is denoted at the top of each image. The localized spectra give information about all the phase transitions of Xe occurring during the melting and dissolution processes.

The images of Fig. 7.5(c)-(f) show also a peak at 205 ppm in the trace of Xe spectra between 2 mm $< z <$ 6 mm, which is most likely Xe dissolved in liquid ethanol at smaller Xe density on the warmer walls of the glass tube (see chapter 1). In all the images, only small amounts of Xe gas (indicated by a chemical shift of 0 ppm) exist above the meniscus and nearly all the Xe polarization is trapped in the thin layer at the bottom of the sample tube for more than 11 min and up to temperatures of 280 K (Fig. 7.5(f)). This is far beyond the boiling point of liquid Xe of 208 K at 7 bar. The boiling point of the Xe-ethanol layer increases during time because of the dilution of the mixture from the viewpoint of pure liquid Xe due to the diffusion of ethanol molecules into the layer, which leads to a higher boiling point of the mixture and hinders therefore the evaporation of Xe gas. The region of the ethanol phase, which is above the thin layer with a high Xe concentration and in contact with the gas phase, is represented in the image at 690 s (Fig. 7.5(f)) by a group of small lines at 175 ppm between 6 and 8 mm. This chemical shift is the smallest observed in the ethanol phase during the whole incorporation experiment indicating a low Xe density in this region which also proves that only a small amount of Xe is leaving the dense Xe/ethanol layer at the bottom of the tube. This experimental result suggests that ethanol is a good storage medium for hyperpolarized Xe.

Looking at all spectra of the Xe layer at the bottom of the tube it is striking that they have very broad line widths (up to 33 ppm) and very different and asymmetric line shapes. The high Xe density inside this layer should not result in broad lines as becomes obvious from Fig. 5.5 in chapter 1 where also the spectra with very high Xe densities show thin lines. An enhanced view of the bottom region of the CSI images is shown for t = 210 s in Fig. 7.6.

The broad and asymmetric line shapes arise from huge Xe density gradients in the radial and z-directions as is indicated by the drawing on the left-hand side of Fig. 7.6 leading to a superposition of narrow lines with different chemical shifts and amplitudes. Temperature gradients within the ethanol phase cannot explain the observed line broadening, because the separate temperature measurements (Fig. 7.3) result in temperature differences over the whole ethanol sample of less than 5 K, which lead to line shifts of about 1.8 ppm. From equation 5.4-1 and the corresponding coefficients of the Xe-ethanol and Xe-Xe interaction determined in chapter 1 it can therefore be calculated that the observed maximum line width of 33 ppm corresponds to Xe density variations of about 70 amagat in the radial and z-directions within the measured sample slice (Δz = 0.5 mm; Δy = 3.5 mm).
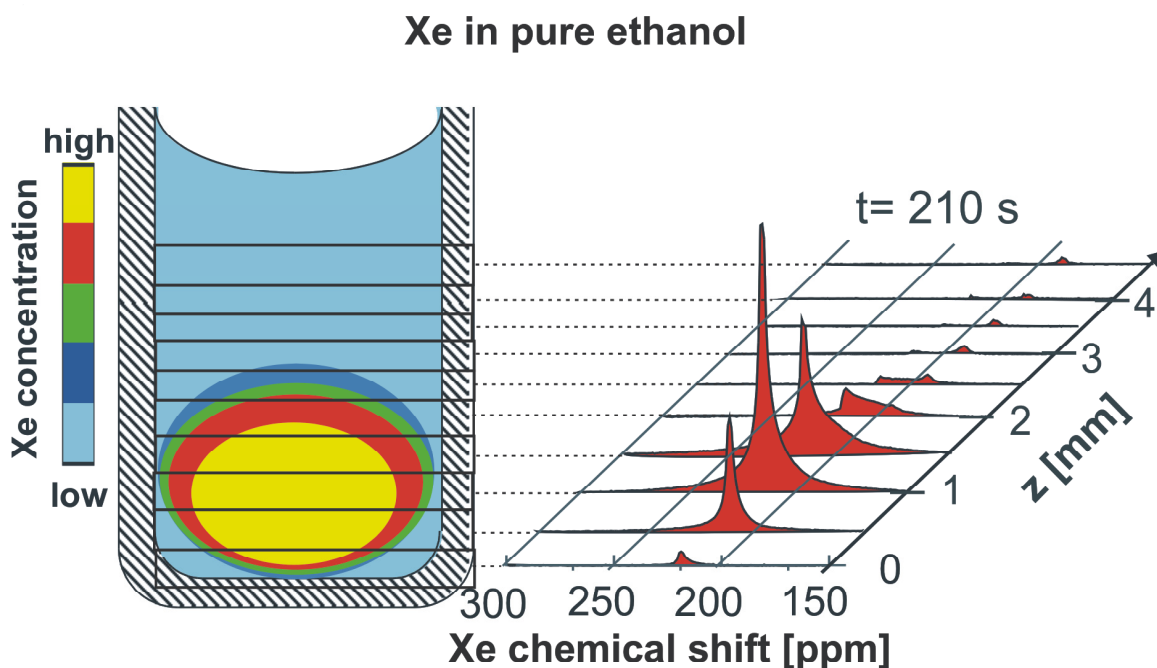
Fig. 7.6: Zoom to the bottom part of the CSI image acquired at t = 210 s. In the spectroscopic dimension only the lines are shown which correspond to Xe in the dissolved or liquid phase. The big changes of the shape and the width of the lines at different positions z can be explained by large variations in the Xe concentration on the bottom of the tube which is indicated by the schematic drawing on the left-hand side of the figure.

Now the corresponding incorporation process of hyperpolarized Xe is discussed for the 80/20 vol% ethanol/water mixture. Therefore the CSI images in Fig. 7.7(a)-(f) show the process of the melting, dissolution and evaporation of hyperpolarized Xe ice accumulated on top of a frozen 80/20 vol% ethanol/water mixture. The notation of the images is the same as for the CSI images for the case of pure ethanol in Fig. 7.5. The first image of this series acquired at 0 s and a temperature T_s of 122 K shows only Xe ice lying on top of the meniscus of the frozen solvent and attached to the inner glass tube which is the same situation as for pure ethanol depicted in Fig. 7.5 (a). The denoted temperature was also determined by the line width of the Xe ice signal [Yen]. In the next image (Fig. 7.7(b)) measured at t = 40 s and T_s = 154 K solid Xe (300 ppm) coexists with the liquid (255 ppm) and the gas phase (0 ppm) and a small amount of liquid Xe has penetrated through the whole ethanol/water ice block as can be seen from the group of small lines at 255 ppm positioned at z = 0-4 mm. At t = 80 s (186 K) most of the Xe has converted into the liquid phase and is concentrated on the surface of the ethanol/water ice block in analogy to the FLASH image in Fig. 7.4 at t = 80 s.
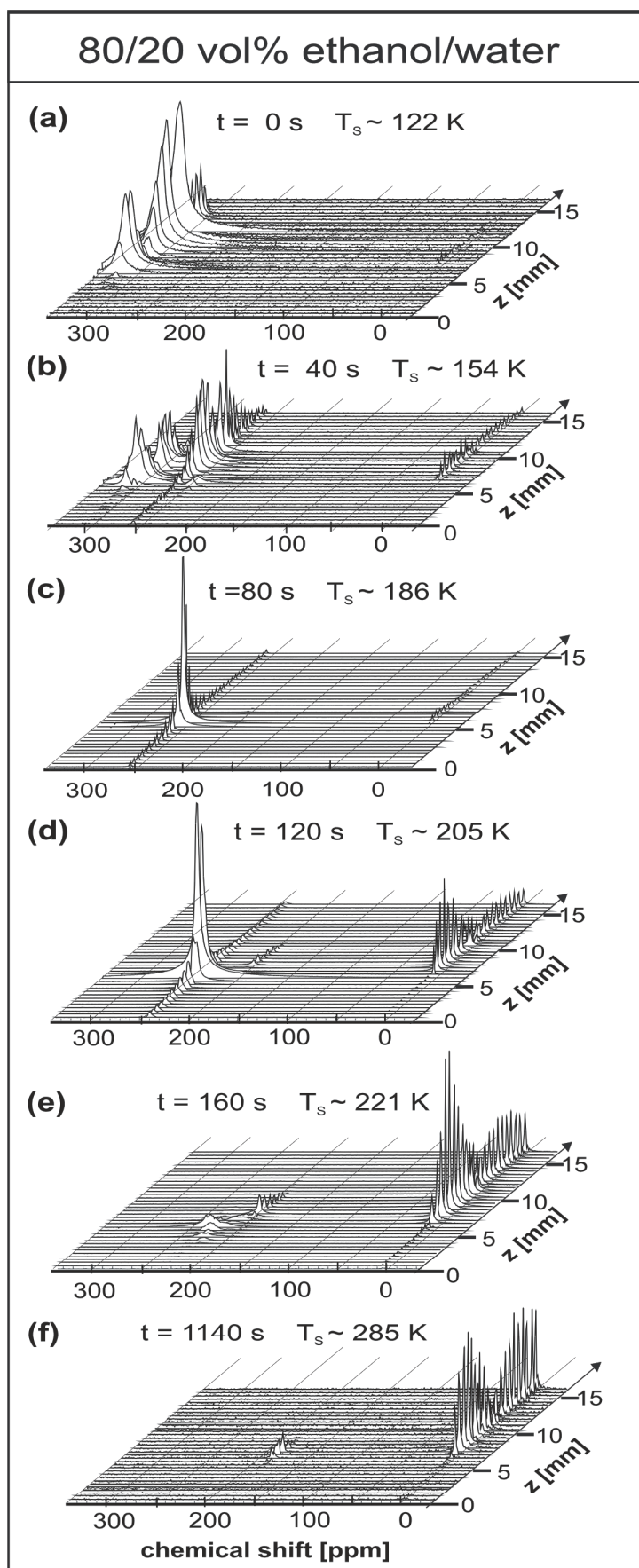
Fig. 7.7: Time series of one-dimensional CSI images of hyperpolarized Xe frozen on 80/20 vol% ethanol/water ice. The horizontal axis in the plots represents the spectroscopic dimension of the Xe chemical shift ranging from 0 to 350 ppm. The vertical axis corresponds to the amplitude of the spectrum and the third axis gives the z position, where $z = 0$ mm is the bottom of the sample tube and $z = 6.5$ mm depicts the lowest point of the ethanol/water meniscus. The corresponding times and temperatures of the CSI images are denoted at the top of each image. These images show that the different Xe phases (Xe gas, liquid, solid or dissolved phase) can be well discriminated by this method compared to the FLASH-images in Fig. 7.4. The CSI images show that after 1140 s most of the hyperpolarized Xe has evaporated into the gas phase and that only a small amount has dissolved into the ethanol/water mixture.

In the next CSI image (Fig. 7.7(d)) obtained at t = 120 s the measured temperature on the surface of the solvent T_s ~ 205 K is close to the boiling point of liquid Xe (~ 208 K at 7 bar). Therefore the liquid Xe has begun to evaporate into the gas phase, as is indicated by the increased amplitude of the Xe gas lines in the spectra above the meniscus of the solvent. The group of small lines at 200 ppm located at the range of the meniscus represents the dissolution of Xe into a liquid ethanol/water layer, which exists at the warmer surface of the sample tube. The following CSI image at t = 160 s and T_s = 221 K (Fig. 7.7(e)) shows that most of the hyperpolarized Xe has evaporated into the gas phase and only a small amount of liquid and dissolved Xe is left at the meniscus of the ethanol/water mixture. The ethanol/water ice block (T_m = 210 K) still exists several hundred seconds after all the liquid Xe has evaporated hindering the dissolution of the hyperpolarized Xe. The spectrum below the meniscus (z < 6.5 mm) in Fig. 7.7(e) shows a row of Xe gas lines with very small amplitudes and chemical shifts that differs slightly from the chemical shift of free Xe gas, which originated from the migration of liquid Xe through the pores of the solvent ice matrix and subsequent evaporation of the liquid Xe to the gas phase. Xe gas which is enclosed in pores with different diameters has a different chemical shifts compared to the free Xe gas because of Xe interactions with the walls of the pores. This phenomenon can be used for the pore size determination with [129]Xe NMR as has been shown in many applications [Ito, Raf2, Chm, Raf3, Rat, Ter, Nos, Jam, Sea, Stu, Mou]. These gas lines of enclosed Xe inside the melting ethanol/water ice block remain until t = 600 s.

A magnified view of the time series of Xe spectra at the meniscus (z = 6 mm) is given in Fig. 7.8 which shows the development of a group of gas lines with different chemical shifts for t >120 s and temperatures above the boiling point of liquid Xe. These lines can be associated with the presence of open and closed pores of different sizes existing inside the ethanol/water ice block which are filled with Xe gas of different pressures. The broad lines between 200 and 250 ppm in Fig. 7.8 and at 220 ppm in Fig. 7.7(e) between 3 mm < z < 6 mm indicate that a fraction of the Xe has dissolved into the liquid ethanol/water phase coexisting with the solvent ice matrix. Again large Xe density gradients cause the broad lines with very different line shapes as was already discussed for the measurements of pure ethanol.
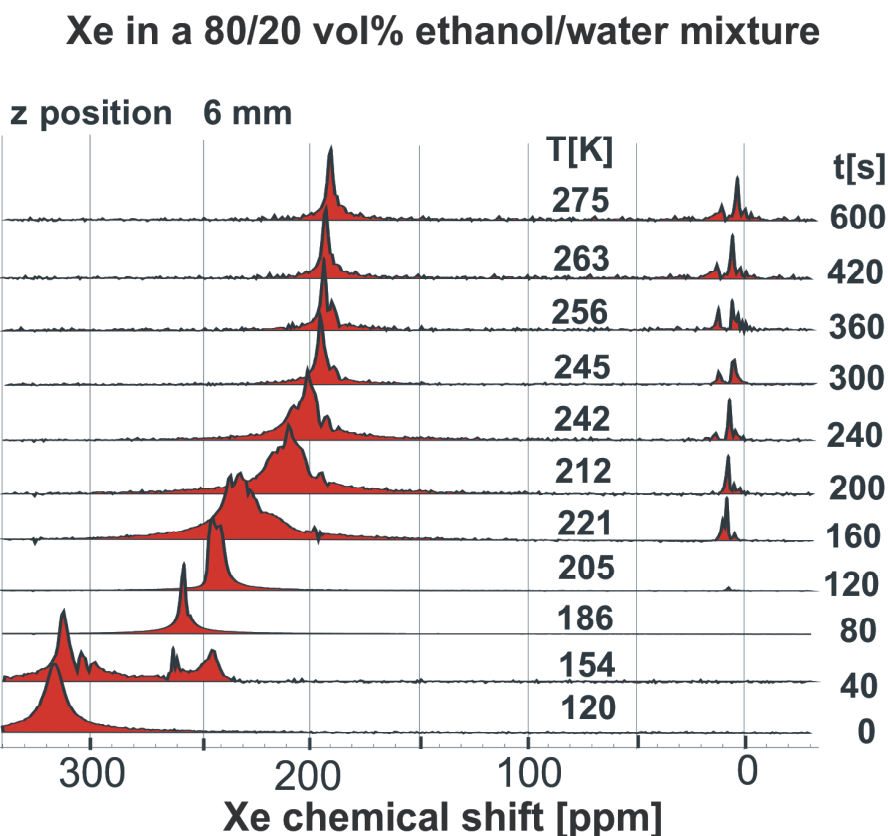
Fig. 7.8: Time dependence of the Xe spectrum for an 80/20 vol% ethanol/water mixture measured at the meniscus of the ice block at $z = 6$ mm. The Xe gas peaks with a chemical shift of a few ppm appearing after t = 120 s are associated with closed and open pores filled with Xe gas at different pressures.

After 1140 s and at a temperature T_s of 285 K (Fig. 7.7(f)) the whole ethanol/water ice block has melted and the corresponding CSI image shows that only two lines remain, a single Xe gas line with high amplitude at $z > 6.5$ mm and a line corresponding to Xe dissolved in the liquid meniscus (180 ppm) between 6 mm $< z <$ 9 mm. The fact that no Xe signal can be observed inside the ethanol/water mixture (z < 6 mm) except in the vicinity of the meniscus means that all the magnetization of the dissolved Xe has decayed to zero and that the liquid surface is in continuous exchange with the Xe gas reservoir. These experiments clearly demonstrate that this method is not useful for the delivery of high amounts of hyperpolarized Xe to the ethanol/water mixture. The high melting point of the mixture far above the boiling point of liquid Xe hinders the dissolution of the hyperpolarized Xe in the solvent which might be the case for all solvents with melting points above the Xe boiling point. The large polarization of the frozen Xe ice may be preserved in the liquid alcohol/water mixture by rapidly heating up the sample, which leads to strong convective mixing of Xe into the solvent.

7.5   Conclusions and outlook

Using the method of time resolved laser-polarized Xe CSI and FLASH imaging it has been demonstrated how Xe atoms incorporate and dissolve into different frozen solvents. A wealth of different physical phenomena, such as the observation of phase transitions, the position dependent line narrowing of Xe ice, the creation of pores and the existence of a dense liquid Xe layer in ethanol have been observed. However, the chemical shift of the signals in the Xe spectra depends on temperature and on the Xe density and the line widths depend on density and temperature gradients, so that the spectra under the condition of very high Xe densities in solution have to be carefully interpreted. It has been shown that the dilution of ethanol with water and the subsequent increasing of the melting point lead to a very inefficient incorporation of hyperpolarized Xe.

However, the dense liquid Xe/ethanol mixture is promising for the injection into biochemical or biological systems in vitro, where the highest possible density of polarized Xe atoms should be delivered to the target molecules in the aqueous environment. The good time resolution of the Xe CSI imaging (2 s) presented here promises the feasibility of other applications as well, like the mapping of temperature and gas density versus space in various dynamic processes and the *in situ* measurement of chemical reactions in micro-fluidic reactors.

8 Multi-dimensional MRI with a continuous flow of hyperpolarized Xenon

The topic of this chapter is time-resolved multidimensional imaging using the continuous flow mode of the Rb-Xe hyperpolarizer for the investigation of two different systems. In the first part of the chapter the dissolution process of hyperpolarized Xe gas in organic solvents at room temperature will be studied using two dimensional imaging of Xe in the dissolved phase. These results complete the study of Xe dissolved in ethanol and toluene and their capability to serve as a storage medium for hyperpolarized Xe. The second part of the chapter presents gas phase imaging in porous media and addresses the question if hyperpolarized Xe gas can be used for the nondestructive characterization of porous samples. For this purpose the penetration of Xe into a filter matrix was monitored by taking profiles and two dimensional images as a function of time, and additionally a three dimensional image of Xe gas dispersed in a macro-porous silica ceramic sample was acquired.

8.1   Introduction

 The high non-equilibrium nuclear polarization achievable by optical pumping makes multi-dimensional imaging viable even for the low spin density of hyperpolarized Xe gas in the continuous flow mode of the hyperpolarizer (0.07 bar Xe in the gas phase). This permits, for example, the imaging of macroscopic void spaces in porous materials [Bru2] and the visualization of gas flow and diffusion in porous samples [Cal2, Kai].

The steady state nuclear spin polarization of a continuous flow of hyperpolarized Xe overcomes the time limitations that arise if hyperpolarized Xe is accumulated e. g. as ice. The advantage of the accumulation of hyperpolarized Xe is that a larger amount of spins is present leading to a good signal-to-noise ratio. However, the batch-mode application of hyperpolarized samples is limited by their T_1 relaxation time, which determines the lifetime of the hyperpolarization. Additionally the non-equilibrium magnetization is consumed by the rf pulses applied during the NMR experiment. The signal-to-noise ratio of the continuous flow application of hyperpolarized Xe is smaller compared to the one of accumulated samples due to the much smaller amount of spins, whereas on the other hand the permanent refreshment of the magnetization allows for the use of larger flip angles and signal averaging. This approach

is limited by the time scale on which the exchange between the fresh hyperpolarized gas and the depolarized gas inside the sample takes place. For Xe dissolved in a liquid this exchange can be in the order of minutes depending on the volume of the solvent that the Xe atoms have to penetrate and the size of the gas/liquid interface. One example for the time scale of the dissolution process of hyperpolarized Xe gas in liquids will be shown in the first result part of this chapter by time-resolved two dimensional imaging of the dissolution process of hyperpolarized Xe gas into ethanol and toluene.

The imaging of hyperpolarized Xe gas in a porous sample will not be seriously limited by the exchange time, because in this case the exchange is considerably fast depending on the size and the interconnectivity of the pores as will be demonstrated in the second result part of this chapter. However, another problem can arise in gas phase imaging with hyperpolarized Xe which is due to the rapid diffusion of the atoms in the gas phase. In the condensed phase the one dimensional resolution of MRI images can reach a few micrometers under ideal conditions and is mainly limited by the low signal-to-noise ratio due to the small number of spins in such minute portions. The limits to resolution of hyperpolarized gas imaging mainly arise from the rapid diffusion of the spins, which is typically several orders of magnitude higher than in liquids. Song et al. demonstrated that a resolution of approximately 100 μm in two dimensional images of hyperpolarized Xe gas using gradient strengths typical for micro-imaging hardware, and the image resolution was primarily limited by the rapid gas diffusion and not by the available signal intensity [Son4].

In addition to limiting the MRI resolution, diffusion effects can also distort images of samples containing boundaries or diffusion barriers within the space being imaged. The detailed characterization of this effect is difficult using ^{1}H NMR because due to the slow diffusion of liquids an image resolution below 10 μm is required, which is difficult to achieve because of the weak signal. The use of hyperpolarized Xe gas for studying the effects of boundary restricted diffusion provides two advantages: a strong NMR signal and a large diffusion length which has been exploited by both theoretical approaches [Hys, Put] and experimental evaluation in this field [Son6].

8.2   Experimental

All samples were deoxygenated prior to the NMR measurements. In general, the deoxygenation is not essentially required for measurements with a continuous flow of

hyperpolarized Xe, because minor losses of magnetization due to fast relaxation can be compensated by the permanent delivery of new hyperpolarized spins. But if the dissolution or penetration process of Xe in a special matrix is intended to be studied, the relaxation of the hyperpolarized spins in parts of the sample will lead to an incorrect result. The hyperpolarized Xe gas was produced in the continuous flow mode of the Rb-Xe hyperpolarizer (see chapter 4) and delivered through a 7 m plastic tube directly into the sample tube inside the spectrometer (Xe resonance frequency 55.3 MHz, 20 mm birdcage coil). The flow rate of the gas mixture containing 1% hyperpolarized Xe was for all experiments about 300 cm^3/min.

The pulse sequence for the acquisition of two dimensional FLASH images which was used to monitor the dissolution process of Xe gas in liquids was already shown and discussed in chapter 7.2. A difference to the imaging series in chapter 7.2 was that the flip angle was slightly larger (3° for ethanol and 7° for toluene) and not incremented during the imaging series. The FOV for the experiments with 2 ml ethanol (filling height: 1 cm in a tube with 16 mm inner diameter) was 30 mm in both directions and no slice selection was applied (resolution in z: 117 μm, resolution in x: 469 μm). For the experiments with toluene (1 ml, filling height: 0.5 cm, same tube as for ethanol) the FOV in the x direction was 70 mm (resolution: 273 μm) and in z direction 10 mm (resolution: 156 μm). The experimental time to acquire one image was the same for both solvents and about 1 s.

The penetration of hyperpolarized Xe gas in a polyester filter material (provided by Prof. Kraushaar, university of Karlsruhe) was studied by measuring one-dimensional images in z direction (inner diameter of the sample tube: 7mm, FOV: 20 mm, resolution: 156 μm, flip angle: 70°, experimental time = 10 ms). The used imaging sequence is based on a gradient echo and shown in Fig. 8.1 (a). In addition, two-dimensional FLASH images were acquired during the penetration process with a flip angle of 14° and a field of view of 50 * 30 mm (resolution in x: 1870 μm, resolution in z: 390 μm) within an experimental time of 200 ms.

The three-dimensional image of a porous silica ceramic (provided also by Prof. Kraushaar) was obtained by using the pulse sequence shown in Fig. 8.1(b). The pulse sequence is based on a conventional three-dimensional FLASH image with an additional delay in the loop of the second phase gradient. This delay (25 s) was incorporated into the pulse sequence to allow for the refreshment of magnetization after the acquisition of each two-dimensional slice. The imaging parameters used were: flip angle: 8°, field of view in x, y and z: 42 mm, 46mm, 30 mm, and the corresponding resolution: in x: 328 μm, in y: 718 μm and in z: 937 μm. The total acquisition time was 14 minutes.
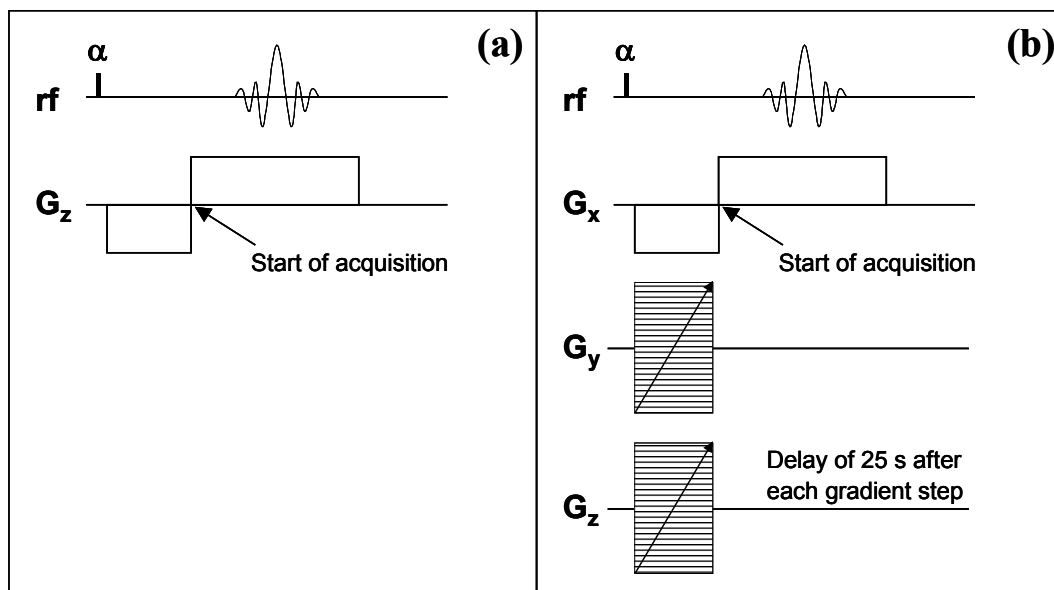
Fig. 8.1: Pulse sequences for the acquisition of (a) profiles and (b) three-dimensonal FLASH images.

8.3 Results I: MRI of the dissolution process of hyperpolarized Xe gas in a continuous flow in organic solvents

In this part of the work the dissolution process of hyperpolarized Xe gas in 2 ml ethanol and 1 ml toluene was studied at room temperature. Because the Ostwald coefficient of Xe in toluene is twice as large as the one of Xe in ethanol, approximately the same amounts of Xe should dissolve in the two liquids. The study of the dissolution process of Xe in a solvent is an important feature because a lot of applications of hyperpolarized Xe NMR take place in a liquid environment like, for example, the on-line monitoring of polymerizations as presented in chapter 6, or biological applications such as the investigation of protein folding mechanisms [Til, Spe, Han2]. For these applications it is crucial that a sufficient amount of hyperpolarized Xe dissolves in the liquid on the time scale of the NMR measurements. This problem is not that significant for the acquisition of NMR spectra, because only one rf pulse per experiment is applied and most of the magnetization will be maintained in the sample. For MRI measurements the time scale of exchange is more important, because a lot of magnetization is consumed due to the large number of excitation pulses. This is especially true for measurements in the continuous flow mode because the smaller number of spins requires the use of larger flip angles to achieve a sufficient signal-to-noise ratio.

Another reason why it is interesting to study the dissolution behavior of hyperpolarized Xe in organic solvents is the possibility to store hyperpolarized Xe in the specific solvent. For this application it must be known how much hyperpolarized Xe dissolves in a certain time in the solvent and if its distribution in the solvent is homogeneous.

Figure 8.2 shows the dissolution process of hyperpolarized Xe gas at room temperature flowing with a flow rate of 300 cm^3/min over 2 ml ethanol (top part) and 1 ml toluene (bottom part). The times denoted below the images correspond to the times after the continuous flow was turned on. The filling heights in the sample tube were about 1 cm for ethanol and 0.5 cm for toluene. The images of both solvents were not acquired with the same field of view and the same resolution making a quantitative analysis of the dissolution process difficult. However, the images in Fig. 8.2 depict a zoom to the same region of interest of the samples allowing a qualitative evaluation of the dissolution process of Xe in ethanol and toluene.
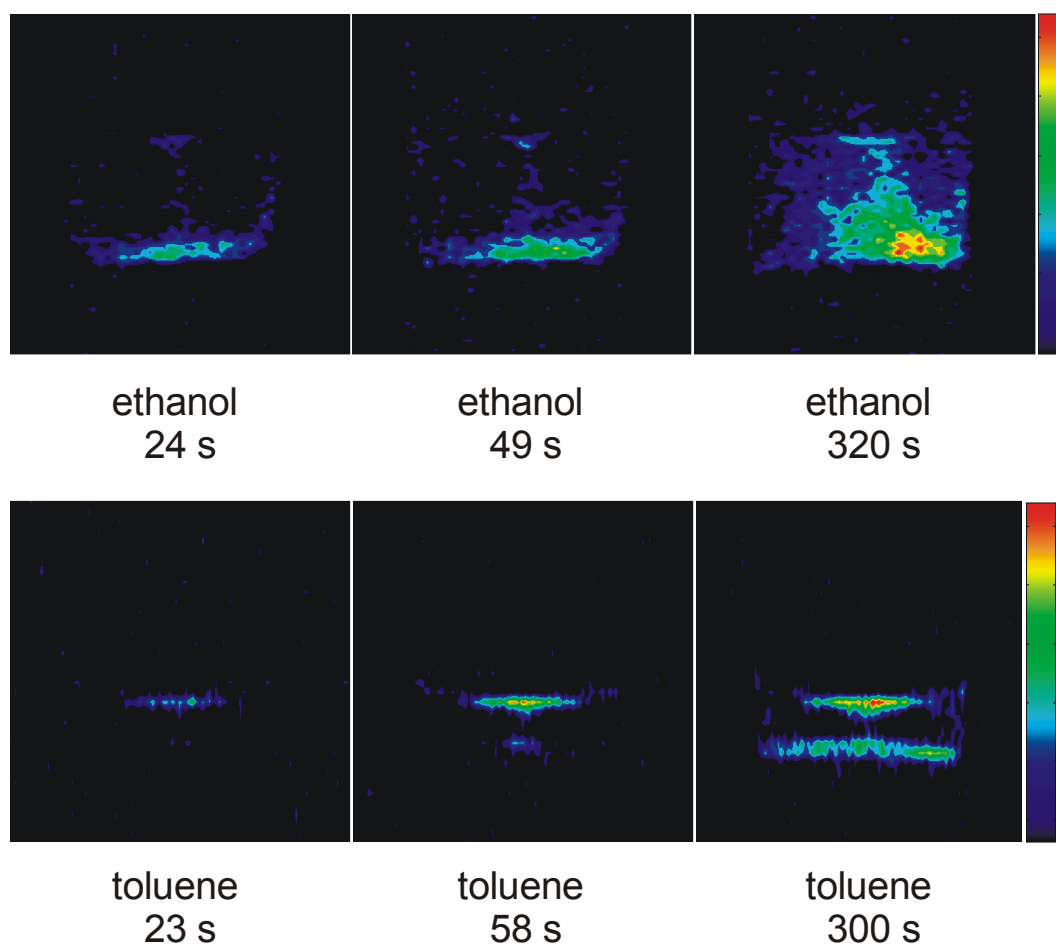

Fig. 8.2: Series of FLASH images monitoring the dissolution process of hyperpolarized Xe in 2 ml ethanol (top part) and 1 ml toluene (bottom part). The same region of interest is displayed for all images. The time denoted under the images represents the time after the continuous flow of hyperpolarized Xe was turned on.

It is observed that the Xe dissolving in ethanol sinks down in a stream from the center of the meniscus directly through the solvent to the bottom of the sample tube where it forms a thin layer. This is in agreement with the imaging experiments of accumulated Xe in cold ethanol of chapter 7 and was also observed by Navon et al. for the dissolution of hyperpolarized Xe gas (not in continuous flow) in partially deuterated benzene [Nav]. After 320 s a considerable amount of Xe has dissolved in ethanol, but its distribution is very inhomogeneous. The distribution of Xe in the solvent is driven by two forces: by diffusion and by convection. The latter seems to occur in the solvent due to the gas stream that hits the center of the meniscus. This convection pattern is indicated by the Xe signal occurring at the edges of the sample tube as can be seen from the images taken at 24 s and 49 s after the start of the continuous flow. The observation of the inhomogeneous Xe distribution in the solvent is a real effect and cannot arise from a distortion of the images due to convection. This can be concluded from the gas phase images of the measurements, which are not depicted in Fig. 8.2. The images of the gas phase show a homogeneous Xe distribution and no influence of the fast movement of the Xe atoms in the gas phase due to the low resolution of the images.

For the dissolution process of Xe gas in toluene, the Xe also incorporates first in the meniscus of the solvent, but it does not sink to the bottom of the sample tube immediately (see image acquired at 23 s). From the next image it can be seen that a huge amount of Xe has accumulated at the meniscus of the toluene and a smaller amount of hyperpolarized Xe has moved through the solvent to the bottom of the sample tube, again forming a layer at this position. After 300 s a high amount of Xe has dissolved in the toluene that had accumulated at the meniscus of the toluene and at the bottom of the sample tube. An even more inhomogeneous distribution as in ethanol is visible which can be due to two effects: The Xe diffusion in toluene might be slower than in ethanol and the convection inside the solvent may be less efficient due to the lower filling height.

Some conclusions can be drawn from these time-resolved imaging experiments. The distribution of Xe inside the solvents is still highly inhomogeneous after five minutes. It can be properly dispersed by vigorous shaking, which was proven in additional experiments the results of which are not shown here. The hyperpolarized Xe accumulates at different positions in the solvents, in ethanol mainly at the bottom of the sample tube and in toluene at the meniscus of the solvent and also at the bottom of the sample tube. This effect can arise from the different densities of the solvents (ethanol: 0,79 g/ml, toluene: 0,87 g/ml [Roe]). The knowledge of the inhomogeneous Xe distribution is important, because these solvents are

intended to be used as storage media for hyperpolarized Xe, and the extraction of the Xe from the storage medium should take place at the position of the highest Xe concentration.

Another very interesting observation was the formation of a convection pattern inside the solvents due to the gas stream that collides with the surface of the solvents. The investigation of this convection by velocity measurements at different flow rates would be useful, because the convection might have a positive effect for some applications of hyperpolarized Xe NMR such as the investigation of reactions in the liquid phase. The convection due to gas flow can lead to a more homogeneous distribution of reactants and products in the reaction bulk yielding well defined kinetics of the reaction and a higher degree of conversion.

8.4   Results II: MRI of hyperpolarized Xe in porous media

The non-invasive characterization of porous materials continues to be an experimental challenge. For example, the properties of many porous materials can depend not only on the overall porosity but also on the size, distribution, and connectivity of the pores within a given material. These properties of porous media can be difficult to study particularly in opaque media without destroying the material of investigation. In principle such materials can be studied by infusing them with water or other liquids, but there are various samples whose chemical and physical sensitivity precludes such approaches like e. g. polymers, catalysts, ceramics, aerogels, food products or living samples [Goo].

^{129}Xe NMR has proven to be a good tool for this kind of investigations due to its chemical inertness and the enhanced contrast it can provide if hyperpolarized. Hyperpolarized Xe is also suitable for dynamic measurements in porous samples. It can be used, for example, as a model system for studying the flow of a gas through a porous medium. These investigations can be also useful for industrial applications and environmental protection, because many gaseous emissions have to be purified by passing a filter medium. Another possible application is the investigation of heterogeneous reactions where a reactant gas flows through a solid porous medium (e. g. a catalyst).

Figure 8.3 presents an example of this kind of study, showing the penetration of hyperpolarized Xe gas into a polyester filter material. The top part of the figure shows a sketch of the experimental conditions whereas the bottom part depicts the results of the time-resolved one-dimensional imaging of this process.
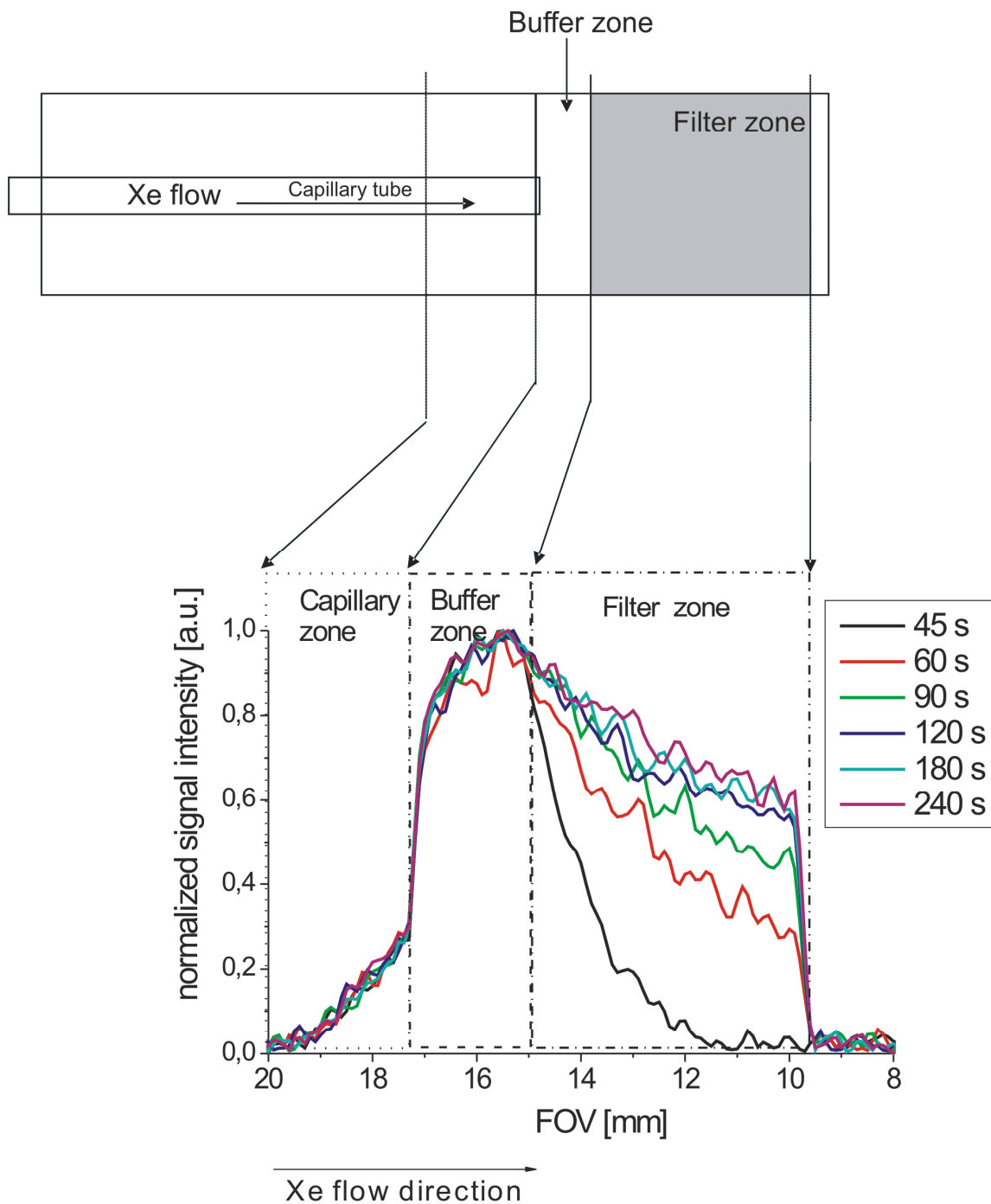
Fig. 8.3: Penetration of hyperpolarized Xe gas into a filter sample. The top part of the figure shows a sketch of the sample tube and the bottom part comprises 1D images as a function of time.

It becomes obvious that the intensities of the profiles reflect very well the slow penetration of hyperpolarized Xe gas into the filter medium and also the different regions of the sample tube (like capillary and buffer zone) can be discriminated reproduciby. The signal amplitude was normalized to the maximum signal amplitude of the buffer region, because the

sample tube is only filled with gas in this region. The decrease of signal intensity in the capillary zone is due to its position within the resonator because it was placed at the edge of the sensitive volume of the birdcage coil. The sudden drop of signal intensity at the other end of the profiles indicates the bottom of the sample tube. The sharp edge representing the end of the sample tube indicates that no distortions due to the fast diffusion of the Xe gas occur in the images at this resolution (156 μm). If the resolution is increased, an edge-enhancement effect due to the restrictive diffusion at the boundaries of the sample would result in a higher signal intensity at the margins of the sample [Saa2, Son6, Tay].

In the region of the filter material the intensity of the profiles increases as a function of the penetration process. This increase of the amount of hyperpolarized Xe within the filter material can also be represented by the integral of the signal intensity at the position of the filter as a function of time, which is shown in Fig. 8.4.
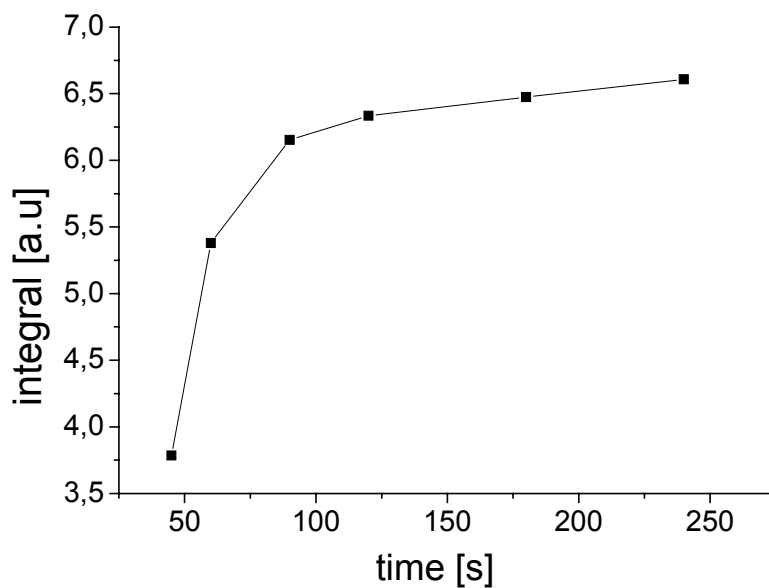

Fig. 8.4: Integral of signal intensity of 1D profiles over the filter region as a function of time.

It can be seen that the integral increases rapidly at the beginning of the penetration process and approaches a maximum value after 240 s when the filter material is completely filled with Xe gas. To ensure that the penetration process was isotropic over the sample volume two-dimensional images were acquired as well as a function of time. Representative, three images are shown in Fig. 8.5. The yellow lines in the figure depict the dimensions of the sample tube and the volume filled by the filter material. The three images show that the penetration of Xe through the filter material proceeds uniformly over the axial dimension of the sample tube indicating an even distributions of the fibers of the filter over the whole material.
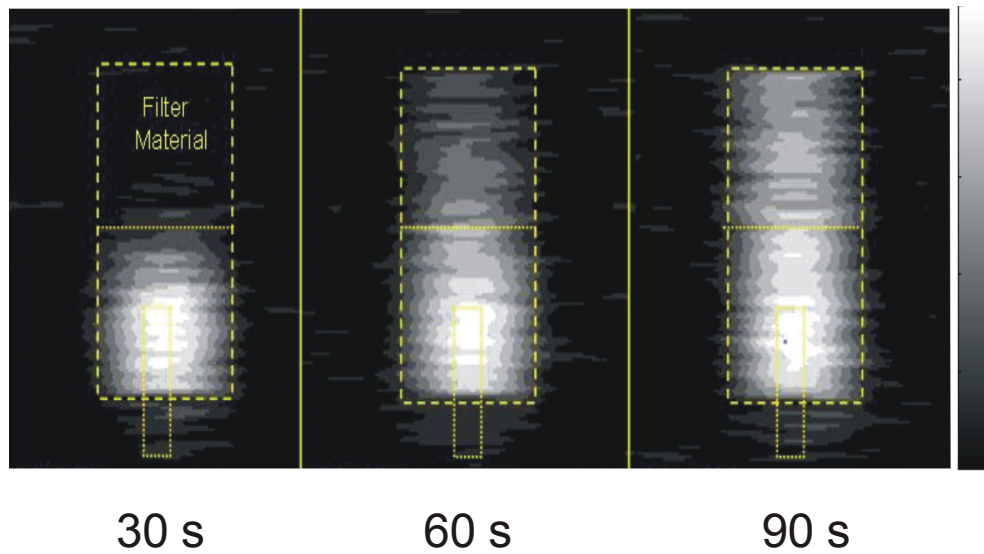
Fig. 8.5: Two-dimensional FLASH images acquired during the penetration process of hyperpolarized Xe into a filter material.

This part of the work has demonstrated that it is possible to successfully monitor the incorporation process of Xe in a porous material by time-resolved one and two-dimensional imaging. The time required for the acquisition of a one-dimensional image (10 ms) and a two-dimensional image (200 ms) would allow to follow much faster processes as well.

If not a dynamic process is the matter of interest but the real structure of a porous material the projection over one or two dimensions of the sample must be avoided and therefore slice selection with two-dimensional imaging or three-dimensional imaging have to be applied. Figure 8.6 shows as an example the three-dimensional image of hyperpolarized Xe gas dispersed in a macro-porous silica ceramic.
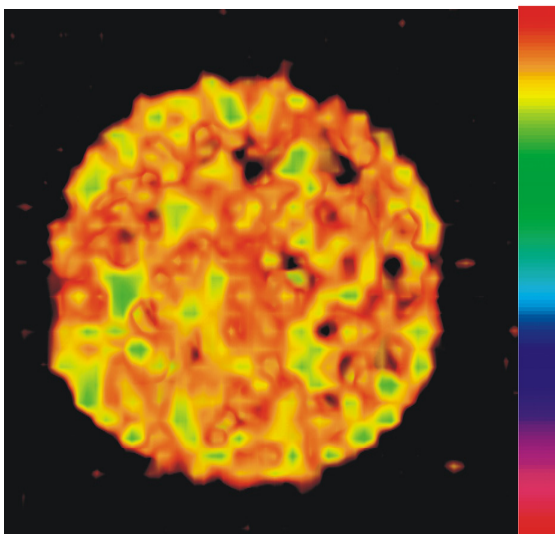

Fig. 8.6: Three-dimensional FLASH image of a porous silica ceramic filled with hyperpolarized Xe. The presented picture shows a zoom to the region of interest of the sample and no free gas is depicted.

Figure 8.6 represents a zoom in the three-dimensional image to the region of the porous medium and displays no free gas in order to have a clear view of the porous sample. The poor resolution of the image (about 1mm in y and z direction and 330 μm in x direction) allows only to distinguish very large pores in the two-dimensional representation of the image. The image was acquired in such a way that after each fast sampling of a plane in k-space (due to read encoding and phase encoding in one direction, the repetition time was about 12 ms) a waiting period of 25 s was abided. This was done to allow the refreshment of the magnetization due to the continuous flow of hyperpolarized Xe in the macro-porous sample in order to get a similar signal-to-noise ratio for each slice of the three dimensional image. The total acquisition time was at 14 minutes still considerably short for a three-dimensional experiment.

8.5   Conclusions and outlook

This chapter revealed the potential of multi-dimensional imaging in the continuous flow mode of the hyperpolarizer. It was demonstrated that the monitoring of dynamic processes like the dissolution of Xe in an organic solvent or the penetration of Xe through a filter medium is viable even with a very small number of hyperpolarized spins (0.07 bar in the gas phase).

The investigation of the dissolution process of hyperpolarized Xe in solvents has shown that the hyperpolarized Xe accumulates at the bottom of the sample tube. This knowledge is important if ethanol or toluene are to be used for the storage of hyperpolarized Xenon. Another interesting point of this study was the formation of a convective motion inside the liquid samples during the measurements with a continuous flow of hyperpolarized Xe. This phenomenon could be exploited in the application of hyperpolarized Xe for the on-line monitoring of chemical reactions.

It has also been demonstrated that hyperpolarized Xe can be used to investigate the properties of porous materials. The penetration of hyperpolarized Xe into a filter material was followed by time-resolved imaging indicating the possibility to model the dynamics of important gas/solid reactions or the efficiency of filtration processes with hyperpolarized Xe. It has also been shown that hyperpolarized ^{129}Xe NMR can be used to determine non-invasively the pore size distribution and pore connectivity of porous materials by three-dimensional imaging within reasonable experimental time.

9 Conclusions and outlook

This work has revealed a part of the great potential of [129]Xe NMR using its extreme sensitivity to its physical and chemical environment and its capability for time-resolved measurements. A variety of different experiments was performed combining NMR measurements with spectroscopic, spatial, and temporal resolution thereby exploiting the large non-equilibrium magnetization of hyperpolarized Xe to monitor dynamic processes.

This work was especially focused on investigations concerning the behavior of Xe in solutions, because many important applications of [129]Xe NMR are expected to take place in the liquid phase such as studies of proteins or cells or a very recent application for the on-line monitoring of chemical reactions developed during this work. Therefore, it was inevitable to earn a solid understanding of the different contributions that determine the Xe chemical shift.

In the first part of this work a new analytical model was introduced which allows the quantitative evaluation of the Xenon chemical shift in the gas and liquid phases and of Xe dissolved in organic solvents. Extensive measurements of the chemical shifts of thermally polarized Xenon were performed as a function of temperature (150-295 K) and Xe density (1-400 amagat). Based on these measurements and on the work of Buckingham and Jameson [Buc, Jam7] a simplified phenomenological model was developed, which describes the dependence of the Xe chemical shift on temperature and density of the interacting atoms or molecules quantitatively using only three fit parameters. With knowledge of the gas temperature, the Xe density in the gas phase can be determined from the chemical shift of the Xe gas. In more complex environments (e. g. Xe dissolved in solvents) the chemical shift can be divided into a part which depends on the interaction of the solvent molecules and the Xe atoms and one part which describes the Xe-Xe interaction in the solvent. Both contributions are described by the model and the activation energies for the atom-atom or atom-molecule interactions were determined. Based on these results it will be possible to describe the dependence of the Xe chemical shift on temperature and density with a simple analytical equation for several solvents. If the chemical shift is independent of the Xe concentration (e.g. as in the case of toluene) the measurement of the chemical shift of hyperpolarized Xe enclosed in biocompatible aromatic system may be used to determine non-invasively the local temperature, for example in the human body.

The second part of this work reports for the first time an application of hyperpolarized [129]Xe NMR spectroscopy to analyze polymerization processes in real-time which is a challenge in polymer engineering. It has been successfully demonstrated that the chemical shift of Xe dissolved in the reaction bulk monitors quantitatively the mole fraction of the monomer allowing the calculation of the conversion at each time of the reaction and the reaction constant. The line broadening and asymmetric line shapes of the dissolved Xe occurring during the polymerization may contain additional information of the physical environment of the Xe atoms in the reaction bulk for example, about chain entanglements that restrict the mobility of the Xe atoms. This aspect of the experiments needs to be explored carefully in the future, possibly leading to additional information of the behavior of macromolecules in solution. The capability to follow not only the living cationic polymerization of THF but also the free radical polymerization of styrene with hyperpolarized [129]Xe NMR suggests an exciting potential for the monitoring of various kinds of reactions.

Two major tasks of hyperpolarized [129]Xe NMR are to find a suitable storage medium for large quantities of hyperpolarized Xe in the liquid phase and to develop a method which ensures the quick and efficient delivery of [129]Xe to the research sample during the polarization lifetime. This is especially difficult for the promising applications of hyperpolarized Xe in biology because the typical solvent for proteins and cells is water in which only small quantities of Xe can be dissolved due to its hydrophobic character. For the efficient delivery of hyperpolarized Xe to aqueous solutions the amphoteric solvent ethanol is promising because it can be mixed with water in arbitrary proportions and is a very good solvent for Xe as has been shown in this work. Therefore, the dynamics of melting, migration, and dissolution of hyperpolarized Xe ice into ethanol and ethanol/water mixtures were investigated with the method of time resolved two-dimensional MRI and one-dimensional CSI starting from the initial condition of a Xe ice layer on top of the frozen solvent. A wealth of different physical phenomena, such as the observation of phase transitions, the position dependent line narrowing of Xe ice, the creation of pores, and the existence of a dense liquid Xe layer in ethanol have been observed. It has been shown that the dilution of ethanol with water and the subsequent increase of the melting point lead to a very ineffective incorporation of hyperpolarized Xe. However, the dense liquid Xe/ethanol mixture is promising for the injection into biochemical or biological systems *in vitro*, where the highest possible density of polarized Xe atoms should be delivered to the target molecules in the aqueous environment. The good time resolution of the Xe CSI imaging (2 s) presented here promises for the

feasibility of other applications as well, like the mapping of temperature and gas density versus space in various dynamic processes and the *in situ* measurement of chemical reactions in micro-fluidic reactors.

The last chapter of this work was devoted to the multi-dimensional imaging of hyperpolarized Xe produced in the continuous flow mode of the hyperpolarizer. It has been successfully demonstrated that the monitoring of dynamic processes like the dissolution of Xe in an organic solvent or the penetration of Xe through a filter medium is viable even with a very small number of hyperpolarized spins (0.07 bar in the gas phase). The investigation of the dissolution process of hyperpolarized Xe in solvents has shown that the hyperpolarized Xe accumulates at the bottom of the sample tube. This knowledge is important if ethanol or toluene are to be used for the storage of hyperpolarized Xenon. Another interesting point of this study was the formation of a convective motion inside the liquid samples during the measurements with a continuous flow of hyperpolarized Xe. This phenomenon could be exploited in the application of hyperpolarized Xe for the on-line monitoring of chemical reactions. Also the potential of ^{129}Xe NMR to be used for the investigation of porous materials has been demonstrated. The penetration of hyperpolarized Xe in a filter material was followed by time-resolved imaging indicating the possibility to model the dynamics of important gas/solid reactions or the efficiency of filtration processes with hyperpolarized Xe. It has been also shown that hyperpolarized ^{129}Xe NMR can be used to determine non-invasively the pore size distribution and pore connectivity of porous materials by three-dimensional imaging within reasonable experimental time.

In this work fundamental aspects as well as exciting new applications of hyperpolarized ^{129}Xe NMR have been revealed that give access to a wide range of further uses in several fields of natural and engineering sciences. Its big advantages, like sensitivity to its environment and the possibility of time-resolved measurements fulfill especially the requirements of investigations in chemical reaction kinetics and dynamics of biomolecules.

10 References

[Abr]   A. Abragam, "Principles of Nuclear Magnetism", *Oxford University Press*, Oxford 1961.

[Alb]   M. S. Albert, G. D. Cates, B. Driehuys, W. Happer, B. Saam, C. S. Springer, A. Wishnia, *Nature 370*, 370, 199–201 (1994).

[Alb2]   M. S. Albert, V. D. Schepkin, T. F. Budinger, *J. Comput. Assited Tomogr.* **19**, 975 (1995).

[Alb3]   M. S. Albert, D. Balamore, *Nucl. Instrum. Methods. Phys. Res. A* **402**, 441-453 (1998).

[App]   S. Appelt, G. Wäckerle, M. Mehring, *Phys. Rev. Lett.* **72**, 3921 (1994).

[App2]   S. Appelt, G. Wäckerle, M. Mehring, *Phys. Lett. A* **204**, 210 (1995).

[App3]   S. Appelt, A. Baranga, B. Erickson, C. J. Romalis, A. R. Young, W. Happer; *Phys. Rev.* **A 58,**1412 (1998).

[App4]   S. Appelt, "From Photon Spin to Magnetic Resonance Imaging", Habilitation, RWTH Aachen 2004.

[App5]   S. Appelt, F. W. Häsing, H. Kühn, J. Perlo, B.Blümich, *Phys. Rev. Lett.* **94**, 197602 (2005).

[App6]   S. Appelt, T. Ünlü, K. Zilles, N. J. Shah, S. Baer-Lang, H. Halling, *Appl. Phys. Letters* **75**, 427 (1999).

[App7]   S. Appelt, „Paramagnetische Verschiebung, Light-Shift-Effekte und die Geometrische Phase im Rb-Xe-System", *Dissertation*, Universität Stuttgart 1993.

[App8]   S. Appelt. F. W. Häsing, S. Bär-Lang, N. J. Shah, B. Blümich, *Chemical Physics Letters*, **348** (2001) 263-269.

[Bac]   P. Bachert, L. R. Schad, M. Bock, M. V. Knopp, M. Ebert, T. Großmann, W. Heil, D. Hofmann, R. Surkau, E. W. Otten, *Magn. Reson. Med.* **36**, 192-196 (1996).

[Bae]   S. U. Baer-Lang, „NMR mit hyperpolarisiertem Xenon in hohen un niedrigen Magnetfeldern", Dissertation RWTH Aachen, 2001.

[Bag]   D. M. S. Bagguely, "Pulsed Magnetic Resonance: NMR, ESR and Optics- a Recognition of E. L. Hahn", *Clarendon Press*, Oxford 1992.

[Bau]   D. Baumer, A. Fink, and E. Brunner, *Z. Phys. Chem.* **217**, 289 (2003).

[Bif]   A. Bifone, Y. Q. Song, R. Seydoux, R. E. Taylor, B. M. Goodson, T. Pietrass, T. F. Budinger, G. Navon, A. Pines, *Proc Natl Acad Sci USA* **93**,12932–6 (1996).

[Blo]   F. Bloch, W. W. Hansen, M. Packard, *Phys. Rev.* **69**, 127 (1946).

[Blü]   B. Blümich, "Imaging of Materials", *Clarendon Press*, Oxford 2000.

[Blü2]   B. Blümich, „Essential NMR", *Spinger-Verlag*, Berlin Heidelberg 2005.

[Bou]   M. A. Bouchiat, R. R. Carver, C. M. Varnum, *Phys. Rev. Lett.* **5**, 373 (1960).

[Bri]   D. Brinkmann, H. Y. Carr, *Phys. Rev.* **150**, 174 (1966).

[Bro]   S. K. Brownstein, J. E. L. Roovers, D. J. Worsfold, *Magn. Reson. Chem.* **130**, 392 (1988).

[Bru]   E. Brunner, Concepts in Magnetic Resonance Vol.11, 313 (1999**)**.

[Bru2]   E. Brunner, M. Haake, A. Pines, J. A. Reimer, *J. Magn. Reson.* **138**, 155-159 (1999).

[Buc]   A. D. Buckingham, J. A. Pople, *Discuss. Faraday Soc.* **22**, 17 (1956).

[Cal]   P. T. Callaghan, "Principles of Nuclear Resonance Microscopy", *Clarendon Press*, Oxford 1991.

[Cal2]   P. T. Callaghan, C. D. Eccles, Y. Xia, *J. Phys. E* **21**, 820-822 (1988).

[Can]   D. Canet, "Nuclear Magnetic Resonance, Concepts and Methods", *Wiley*, Chichester 1996.

[Car]   T. R. Carver and C. P. Slichter, *Phys. Rev* **92**, 212 (1953), ibid. **102**, 975 (1956).

[Cat]   G. D. Cates, D. R. Benton, M. Gatzke, W. Happer, K. C. Hasson, N. R. Newbury, *Phys. Rev. Lett.* **65**, 2591 (1990).

[Cav]   J. Cavanagh, W. J. Fairbrother, A. G. Palmer, N. J. Skelton, "Protein NMR spectroscopy: Principles and Practice", Academic Press, San Diego 1996.

[Che]   A. Cherubini, A. Bifone, "Hyperpolarised xenon in biology", *Progress in Nuclear Magnetic Resonance Spectroscopy* **42**, 1-30 (2003).

[Che2] T. T. P. Cheung, C. M. Fu, S. Wharry, *J. Phys. Chem.* **92**, 5170 (1988).

[Che3] X. L. Chen, M. S. Chawla, G. P. Cofer, L. W. Hedlund, H. E. Möller, G. A. Johnson, *Magn. Reson. Med.* **40**, 61-65 (1998).

[Che4] X. L. Chen, H. E. Möller, M. S. Chawla, G. P. Cofer, B. Driehuys, L. W. Hedlund, J. R. MacFall, G. A. Johnson, *Magn. Reson. Med.* **42**, 645-648 (1999).

[Che5] T. T. P. Cheung, P. J. Chu, *J. Phys. Chem.* **96**, 9551 (1992).

[Chm] B. F. Chmelka, D. Raftery, A. V. McCormick, L. C. de Menorval, R. D. Levine, A. Pines, *Phys. Rev. Lett.* **66**, 580–583 (1991).

[Chu] T. E. Chupp, R. J. Hoare, *Phys. Rev. Lett.* **64**, 2261 (1990).

[Chu2] T. E. Chupp, R. J. Hoare, R. A. Loveman, E. R. Oteiza, J. M. Richardson, M. E. Wagshul, *Phys. Rev. Lett.* **63**, 1541 (1989).

[Coo] G. E. Cook, "Argon, Helium and the Rare Gases", Interscience Publishers, New York (1961).

[Cow] J. M. G. Cowie, "Polymers: Chemistry and Physics of Modern Materials", Blackie Academic & Professional, 2nd edition (1997).

[Cre] Y. Cremillieux, Y. Berthezene, H. Humblot, M. Viallon, E. Canet, M. Bourgeois, T. Albert, W. Heil, A. Briguet, *Magn. Reson. Med.* **41**, 645-648 (1999).

[deLa] E. E. de Lange, J. P.Mugler III., J. R. Brookeman, J. Knight-Scott, J. D. Truwit, C. D. Teates, T. M. Daniel, P. L. Bogorad, G. D. Cates, *Radiology* **210**, 851-857 (1999).

[Dem] J. Demarquay, J. Fraissard, *Chem. Phys. Lett.* **136**, 314 (1987).

[Den] A. J. Deninger, B. Eberle, M. Ebert, T. Großmann, W. Heil, H. U. Kauczor, L. Lauer, K. Markstaller, E. Otten, J. Schmiedeskamp, W. Schreiber, R. Surkau, M. Thelen, N. Weiler, *J. Magn. Reson.* **141**, 207-216 (1999).

[Der] E. G. Derouane, J. M. Andre, A. A. Lucas, *Chem. Phys. Lett.* **137**, 336 (1987).

[Dri] B. Driehuys, G. D. Cates, E. Miron, K. Sauer, D. K. Walther, W. Happer, *Appl. Phys. Lett.* **69**, 1668 (1996).

[Dri2] B. Driehuys, G. D. Cates, W. Happer, H. Mabuchi, B. Saam, *Phys. Lett. A* **184**, 88 (1993).

[Ebe]   M. Ebert, T. Großmann, W. Heil, W. E. Otten, R. Surkau, M. Leduc, P. Bachert, M. V. Knopp, L. R. Schad, M. Thelen, *Lancet* **347**, 1297-1299 (1996).

[Egu]   T. Eguchi, G. Soda and H. Chiara, *Mol. Phys.* **40**, 681 (1980).

[Eli]   H.-G. Elias, "Makromoleküle", *Hüthig & Wepf Verlag*, Basel, Heidelberg, New York 1990.

[Ern]   R. R. Ernst, G. Bodenhausen, A. Wokaun, "Principles of Nuclear Magnetic Resonance in One and Two Dimensions", *Clarendon Press*, Oxford 1991.

[Fre]   G. H. Fredrickson, E. Helfland, *Macromolecules* **18**, 2201 (1985).

[Fuk]   E. Fukushima, S. B. W. Roeder, "Experimental Pulse NMR", Addison-Wesley Publishing Company, Inc., Reading, Massachusetts 1981.

[Gae]   H. C. Gaede, "NMR investigations of Surfaces and Interfaces Using Spin-Porarized Xenon", *Dissertation, Berkeley* 1995.

[Gat]   M. Gatzke, G. D. Cates, B. Driehuys, D. Fox, W. Happer, B. Saam, *Phys. Rev. Lett.* **70**, 690 (1993).

[Goo]   B. Goodson, *J. Magn. Reson.* **155**, 157-216 (2002).

[Gre]   D. M. Gregory, R. E. Gerald II, R. E. Botto, *J. Magn. Reson.* **131**, 327-335 (1998).

[Haa]   M. Haake, B. M. Goodson, D.D. Laws, E. Brunner, M. C. Cyrier, R. H. Havlin, A. Pines, *Chem. Phys. Lett.* **292**, 686 (1998).

[Haa2]   M. Haake, A. Pines, J. A. Reimer, R. Seydoux, *J. Am. Chem. Soc.* **119**, 11711 (1997).

[Han]   S. Han, H. Kühn, F. W. Häsing, K. Münnemann., B. Blümich, S. Appelt, *J. Magn. Reson.* **167**, 298-305 (2004).

[Han2]   S. Han, S. Garcia, T. J. Lowery, E. J. Ruiz, J. A. Seeley, L. Chavez, D. S. King, D. E. Wemmer, A. Pines, "Improved NMR Based Bio-Sensing with Optimized Delivery of Polarized ^{129}Xe to Solutions", *Anal. Chem.*, in press.

[Hap]   W. Happer; *Rev. Mod. Phys.*, **44** (1972) 169.

[Hap2]   W. Happer, E. Miron, S. Schaefer, D. Schreiber, W. A. van Wijngaarden, X. Zeng, *Physical Review A* **29**, 3092 (1984).

[Har]   R. K. Harris, B. E. Mann, "NMR and the Periodic Table", *Academic Press* 1978.

[Hir]   G. J. Hirasaki, "NMR applications in petroleum reservoir studies" in S. Stapf, S. Han, (Eds.), "Nuclear Magnetic Resonance Imaging in Chemical Engineering", Wiley-VCH, in press.

[Hol]   A. F. Hollemann, E. Wiberg, „Lehrbuch der Anorganischen Chemie", *de Gruyter* 1985.

[Hun]   E. R. Hunt, H. Y. Carr, *Phys. Rev.* **130**, 2302 (1963).

[Hys]   W. B. Hyslop, P. C. Lauterbur, J. Magn. Reson. **94**, 501-510 (1991).

[Ish]   K. Ishigawa, H. Imai, Y. Takagi, *Phys. Rev. A* **70**, 042712 (2004).

[Ito]   T. Ito, J. Fraissard, *J. Chem. Phys* **76**, 5225 (1982).

[Jae]   H. J. Jaensch, J. Hof, U. Ruth, J. Schmidt, D. Stahl and D. Fick, *Chem. Phys. Lett.* **296**, 146 (1998).

[Jam]   C. J. Jameson, A. C. de Dios, *J. Chem. Phys.* **116**, 3805 (2002).

[Jam2]   C. J. Jameson, A. K. Jameson, J. K. Hwang, *J. Chem. Phys.* **89**, 4074 (1988).

[Jam3]   A. K. Jameson, C. J. Jameson, H. S. Gutowsky, *J. Chem. Phys.* **53**, 2310 (1970).

[Jam4]   C. J. Jameson, A. K. Jameson, S. M. Cohen, *J. Chem. Phys.* **62**, 4224 (1975).

[Jam5]   C. J. Jameson, A. K. Jameson, *Mol. Phys.* **20**, 957 (1971).

[Jam6]   C. J. Jameson, A. K. Jameson, S. M. Cohen, J. Chem. Phys. 59, 4540 (1973).

[Jam7]   C. J. Jameson, A. C. deDios, *J. Chem. Phys.* **97**, 417 (1992).

[Jau]   Y. Y. Jau, N. N. Kuzma, W. Happer, *Phys. Rev. A* **69**, Art. No. 061401 (2004).

[Joh]   E. Johansson, J. Svensson, S.Mansson, J. S. Petersson, L. E. Olsson, K. Golman, F. Stahlberg, *J. Magn. Reson.* **159**, 68 (2002).

[Joh2]   G. A. Johnson, G. Cates, X. J. Chen, C. P. Cofer, B. Driehuys, W. Happer, L. W. Hedlund, B. Saam, M. D. Shattuck, J. Swartz, *Magn. Reson. Med.* **38**, 66-71 (1997).

[Jok]   J. Jokisaari, Progress in NMR Spectroscopy **26**, 1 (1994).

[Jun]   F. Junker, W. S. Veeman, *Macromolecules* **31**, 7010-7013 (1998).

[Jun2] F. Junker, "Materialforschung an porösen Festkörpern mittels Xenon-Diffusionsmessungen: Eine ^{129}Xe-PFG-NMR-Studie", Dissertation, Gerhard-Mercator-Univerität Duisburg 2000.

[Kai] L. G. Kaiser, T. Meersmann, J. W. Logan, A. Pines, *Proc. Natl. Acad. Sci. U.S.A.* **97**, 2414-2418 (2000).

[Kas] A. Kastler, *J. Phys. Radium* **11**, 255 (1950).

[Ken] A. P. M. Kentgens, H. A. van Boxtel, R.-J. Verweel, W. S. Veeman, *Macromolecules* **24**, 3712-3714 (1991).

[Ken2] G. J. Kennedy, *Polym. Bull.* **23**, 605 (1990).

[Kim] R. Kimmich, "NMR Tomography, Diffusometry, Relaxometry", *Springer-Verlag*, Berlin 1997.

[Kna] K. Knagge, L. J. Smith, D. Raftery, *J. Phys. Chem. B.* **109(10)**, 4533-4538 (2005).

[Kna2] K. Knagge, J. Prange, D. Raftery, *Chem. Phys. Lett.* **397**, 11 (2004).

[Kuz] N. N. Kuzma, B. Patton, K. Raman, W. Happer, *Phys. Rev. Lett.* **88**, 147602 (2002).

[Lan] C. Landon, P. Berthault, F. Vocelle, H. Desvaux, *Protein Sci.* **10**, 762 (2001).

[Lea] J. C. Leawoods, B. T. Saam, M. S. Conradi, *Chem. Phys. Lett* **327**, 359 (2000).

[Loc] E. Locci, Y. Dehouck, M. Casu, G. Saba, A. Lai, M. Luhmer, J. Reisse, K. Bertik, *J Magn Reson* **150**, 167–4 (2001).

[Mac] J. R. Macfall, H. C. Charles, R. D. Black, H. Middleton, J. C. Swartz, B. Saam, B. Driehuys, C. Erickson, W. Happer, G. D. Cates, G. A. Johnson, C. E. Ravin, *Radiology* **200**, 553-558 (1996).

[Mai] R. W. Mair, R. Wang, M. S. Rosen, D. Candela, D. G. Cory, R. L. Walsworth, Magn. Reson. Imag. 21, 287 (2003).

[Mai2] G. C. Maitland, M. Rigby, E. B. Smith, W. A. Wakeham, "Intermolecular forces, their Origin and determination", *Clarendon Press*, Oxford 1981.

[Man] M. Mansfeld, W. S. Veeman, *Chem. Phys. Lett.* **222**, 422 (1994).

[Mat] K. Matyjaszewski (ed.), "Cationic Polymerizations: Mechanisms, Synthesis, and Applications", *Marcel Dekker, inc.* (1996).

[Maz] R. K. Mazitov, A. N. Panov, K. M. Enikeev, A. V. Il'yasov, *Docklady Biophys* **28**, 364366 (1999).

[Mil] J. B. Miller, J. H. Walton, C. M. Roland, *Macromolecules* **26**, 5602 (1993).

[Mil2] J. B. Miller, J. H. Walton, C. M. Roland, *Macromolecules* **25**, 5602 (1996).

[Moe] H. E. Möller, X. J. Chen, M. S. Chawla, B. Driehuys, L. W. Hedlund, G. A. Johnson, *J. Magn. Reson.* **135**, 133-143 (1998).

[Mor] S. Morel, *16th European Symposium on Polymer Spectroscopy (ESOPS),* may 29-June 1, 2005, Kerkrade, Netherlands.

[Mou] I. L. Moudrakovski, L. Q. Wang, T. Baumann, J. H. Satcher, G. H. Exarhos, C. I. Ratcliffe, J. A. Ripmeester, *J. Amer. Chem. Soc.* **126**, 5052 (2004).

[Mou2] I. L. Moudrakovski, S. Lang, C. I. Ratcliffe, S. Benoit, G. Santyr, J. A. Ripmeester, *J. Magn. Reson.* **144**, 372 (2000).

[Mou3] I. L. Moudrakovski, C. I. Ratcliffe, J. A. Ripmeester, *J. Am. Chem. Soc.* **123**, 2066 (2001).

[Mue] A. Müller, *Dissertation*, RWTH Aachen, Aachen 1994.

[Mug] J. P. Mugler, B. Driehuys, J. R. Brookeman, G. D. Cates, S. S. Berr, R. G. Bryant, T. M. Daniel, E. E. de Lange, J. H. Downs, C. J. Erickson, W. Happer, D. P. Hinton, N. F. Kassel, T. Maier, C. D. Philipps, B. T. Saam, K. L. Sauer, M. E. Wagshul, *Magn Reson Med* **37**, 809–815 (1997).

[Nav] G. Navon, Y.-Q. Song, T. Room, S. Appelt, R. E. Taylor, A. Pines, *Science* **271**, 1848 (1996).

[Nos] A. Nossov, E. Haddad, F. Guenneau, A. Gedeon, *Phys. Chem. Chem. Phy* **5**, 4473 (2003).

[Pat] B. Patton, N.N. Kuzma, W. Happer, *Phys. Rev. B* **65**, 020404 (2001).

[Pie] T. Pietraß, *Magnetic Resonance Review* **17**, 263 (2000**)**.

[Pie2] T. Pietrass, A. Bifone, A. Pines, *Surface Science*, **334**, L730 (1995).

[Pur] E. M. Purcell, H. C. Torrey, R. V. Pound, Phys. Rev. 69, 37 (1946).

[Put] B. Putz, D. Barsky, K. Schulten, *J. Magn. Reson.* **97**, 27-53 (1992).

[Raf]   D. Raferty., H. Long,, L. Reven,, P. Tang, A. Pines; *Chem. Phys. Letter* **191** (1992) 385.

[Raf2]   D. Raftery, H. Long, T. Meersmann, P. Grandinetti, L. Reven, A. Pines, *Phys. Rev. Lett.* **66**, 584 (1991).

[Raf3]   D. Raftery, B. F. Chmelka, "Xenon NMR Spectroscopy", *NMR - Basic Principles and Progress*, **30**, 111 (1994).

[Rat]   C. I. Ratcliffe, "Xenon NMR" *Ann. Rep. NMR Spec.* **36**, 123 (1998).

[Rip]   J. A. Ripmeester, C. I. Ratcliffe, *J. Chem. Phys*. **94**, 7652 (1990).

[Roe]   Roempp Chemielexikon, Ausgabe 1991.

[Roo]   T. Room, S. Appelt, R. Seydoux, E. L. Hahn, A. Pines, Phys. Rev. B 55, 11604 (1997).

[Rom]   M. V. Romalis, E. Miron, G. D. Cates, *Phys. Rev. A* **56**, 4569 (1997).

[Rub]   S. M. Rubin, M. M. Spence, B. M. Goodson, D. E. Wemmer, A. Pines, *Proc Natl Acad Sci USA* **97,** 9472–5 (2000).

[Rub2]   S. M. Rubin, M. M. Spence, I. E. Dimitrov, E. J. Ruiz, A. Pines, D. E. Wemmer, *J Am Chem Soc* **123**, 8616–7 (2000).

[Saa]   B. Saam, D. A. Yablonskiy, D. S. Gierada, M. S. Conradi, *Magn. Reson. Med.* **42**, 507-514 (1999).

[Saa2]   B. Saam, N. Drukker, W. Happer, *Chem. Phys. Lett.* **263**, 481-487 (1996).

[Sah]   K. Sahre, T. Hoffmann, D. Pospiech, D. Fischer, K.-J. Eichhorn, B. Voit, *16th European Symposium on Polymer Spectroscopy (ESOPS),* may 29- June 1, 2005, Kerkrade, Netherlands.

[Sak]   K. Sakai, A. M. Bilek, E. Oteiza, R. L. Walsworth, D. Balamore, F. Jolesz, M. S. Albert, *J. Magn. Reson. B* **111**, 300-304 (1996).

[Sea]   D. N. Sears, C. J. Jameson, *J. Chem. Phys.* **119**, 12231 (2003).

[Sim]   J. H. Simpson, W. Y. Wen, A. A. Jones, *Macromolecules* **29**, 2138 (1996).

[Sli]   C. P. Slichter, „Principles of Magnetic Resonance", *Springer-Verlag,* Berlin 1978.

[Smi]   J. Smith, L. J. Smith, K. Knagge, E. MacNamara, D. Raftery, J. Am. Chem. Soc. 123(12), 2927-2928 (2001).

[Smi2] B. D. Smith, R. Srivastava eds., "Thermodynamic data for pure compounds, Part B, halogenated hydrocarbons and alcohols", *Elsevier*, Amsterdam-Oxford-NewYork, Tokyo 1986.

[Son]   Y.-Q. Song, S. Ryu, P. N. Sen, *Nature* **406**, 178 (2000).

[Son2] Y.Q. Song, B. M. Goodson et al., *Angew. Chem.* **109,** 2464-2466 (1997).

[Son3] Y.Q. Song, *Concepts Magn. Reson.* **12**, 6-20 (2000).

[Son4] Y.Q. Song, H. C. Gaede, T. Pietraß, G. A. Barrall, G.C. Chingas, M. R. Ayers, A. Pines, *J. Magn. Reson. A* **115**, 127-130 (1995).

[Son5] Y.Q. Song, B. M. Goodson, R. E. Taylor, D. D. Laws, G. Navon, A. Pines, *Angew. Chem. Int. Ed.,* **36**, 359 (1997).

[Son6] Y.-Q. Song, B. M. Goodson, B. Sheridan, T. M. de Swiet, A. Pines*, J. Chem. Phys.* **108**, 6233-6239 (1998).

[Spe]   M. M. Spence, S. M. Rubin, I. E. Dimitrov, E. J. Ruiz, D. E. Wemmer, A. Pines, S. Q. Yao, F. Tian, P. G. Schultz, *Proc Natl Acad Sci USA* **98**, 10654–7 (2001).

[Sta]   S. Stapf, S. Han (Eds.), "Nuclear Magnetic Resonance Imaging in Chemical Engineering", Wiley-VCH, in press.

[Ste]   T. R. Stengle, K. L. Williamson, *Macromolecules*, **20**, 1428-1430 (1987).

[Str]   R. L. Streever, H. Y. Carr, *Phys. Rev.* **121**, 20 (1961).

[Str2] W. B. Streett, L. S. Sagan, L. A. K. Staveley, *J. Chem. Thermodyn.* **5**, 633 (1973).

[Stu]   D. Stueber, C. J. Jameson, "The chemical shifts of Xe in the cages of clathrate hydrate structures I and II", *J. Chem. Phys.* **120**, 1560 (2004).

[Su]   T. Su, G. L. Samuelson, S. W. Morgan, G. Laicher, B. T. Saam, *Appl. Phys. Lett.* **85**, 2429 (2004).

[Swa]   S. D. Swanson, M. S. Rosen, B. W. Agranoff, K. P. Coulter, R. C. Welsh, T. E. Chupp, *Magn Reson Med* **38**, 685–8 (1997).

[Swa2] S. D. Swanson, M. S. Rosen, K. P. Coulter, R. C. Welsh, T. E. Chupp, *Magn Reson Med* **42**, 1137-1145 (1999).

[Tay] R. E. Taylor, Y.Q. Song, T. Room, S. Appelt, R. Seydoux, A. Bifone, D. de Graw, B. Goodson, D. Laws, A. Pines, in "37th Experimental Nuclear Magnetic Resonance, Pacific Grove, CA, USA (1996).

[Ter] V. V. Terskikh, I. L. Moudrakovski, S. R. Breeze, S. Lang, C. I. Ratcliffe, J. A. Ripmeester, A. Sayari, *Langmuir* **18**, 5653 (2002).

[Til] R. F. Tilton, I. D. Kuntz, *Biochemistry* **21**, 6850–7 (1982).

[Tor] H. C. Torrey, *Phys. Rev*. **130,** 2306 (1963).

[Tse] C. H. Tseng, R. W. Mair, G. P. Wong, D. Williamson, D. G. Cory, R. L. Walsworth, *Phys. Rev. E* **59**, 1785 (1999).

[Tyc] R. Tycko, J. A. Reimer, *J.Phys. Chem.* **100**, 13240 (1996).

[Ver] A. S. Verhulst, O. Liivak, M. H. Sherwood, I. L. Chuang, *J. Magn Reson*. **155**, 145 (2002).

[Via] M. Viallon, G. P. Cofer, S. A. Suddarth, H. E. Möller, X. J. Chen, M. S. Chawla, L. W. Hedlund, Y. Cremillieux, G. A. Johnson, *Magn. Reson. Med.* **41**, 787-792 (1999).

[Vol] C. H. Volk, J. G. Mark, B. C. Grover, *Phys. Rev. A* **20**, 2381 (1979).

[Wal] T. G. Walker, W. Happer, "Spin-exchange optical pumping of noble-gas nuclei" ,*Rev. Mod. Phys*. **69**, 629 (1997).

[Wal2] J. H. Walton, J. B. Miller, C. M. Roland, *J. Polym. Sci., Part B, Polym. Phys*. **30**, 527 (1992).

[Wan] R. Wang, R. W. Mair, M. S. Rosen, D. G. Cory, R. L. Walsworth, *Phys. Rev. E* **70**, Art. No. 026312 (2004).

[Wol] J. Wolber, D.J.O. McIntyre, L. M. Rodrigues, P. Carnochan, J. R. Griffiths, M. O. Leach, A. Bifone, *Magn Reson Med* **46**, 586–91 (2001).

[Wol2] J. Wolber, A. Cherubini, M. O. Leach, A. Bifone, *Magn. Res. Med.* **43**, 491 (2000).

[Wu] Z. Wu, W. Happer, J. M. Daniels, *Phys. Rev. Lett.* **59**, 1480 (1987).

[Wu2] Z. Wu, W. Happer, M. Kitano, J. M. Daniels, *Phys. Rev. A* **42**, 2774 (1990).

[Yen]   W. M. Yen, R. E. Norberg, *Phys. Rev.* **131**, 269-275 (1963).

[Zoo]   A. L. Zook, B. B. Adhyaru, C. R. Bowers, *J. Magn. Reson.* **159**, 175 (2002).

Many thanks to… / Mein Dank gilt…

Curriculum vitae

Personal data

Name:	Kerstin Münnemann (geb. Kletzke)
Date and place of birth:	13th may 1974, Krefeld
Marital status:	married
Nationality:	German

School Education

1980 – 1984	Geschwister Scholl – primary school in Krefeld
1984 – 1993	Maria Sybilla Merian – secondary school in Krefeld
	Degree (05/1993): general qualification for university entrance („Abitur").

Academic Education

10.1993 – 05.1998	Basic studies of chemistry at the Heinrich-Heine-university in Düsseldorf, Degree: intermediate diploma
05.1998 – 09.1998	Student trainee at Henkel KgaA, Düsseldorf
10.1998 – 03.2002	Advanced study period at RWTH Aachen university Diploma thesis: „NMR-Untersuchung zur anäthetischen Wirkung von Xenon " Degree (03/2002)**:** Diplom-Chemikerin
04.2002 – 09.2005	Promotion and employment at the Institute of Technical und Macromolecular Chemistry of RWTH Aachen university Doctoral examination: 29.09.2005